

Interaction Among Magmas from Various Sources and Crustal Melting Processes During Continental Collision: Insights from the Huayang Intrusive Complex of the South Qinling Belt, China

Fangyang Hu^{1,2}, Shuwen Liu^{1*}, Mihai N. Ducea^{2,3}, Wanyi Zhang⁴, James B. Chapman², Jinghao Fu¹ and Maojiang Wang¹

¹Key Laboratory of Orogenic Belts and Crustal Evolution, Ministry of Education, School of Earth and Space Sciences, Peking University, Beijing 100871, PR China; ²Department of Geosciences, University of Arizona, Tucson, AZ 85721, USA; ³Faculty of Geology and Geophysics, University of Bucharest, Bucharest, Romania; ⁴Development Research Center, China Geological Survey, Beijing 100037, PR China

*Corresponding author. Present address: School of Earth and Space Sciences, Peking University, Beijing 100871, China. Telephone: +86-010-62754163. Fax: +86-010-62754163. E-mail: swliu@pku.edu.cn

Received July 19, 2017; Accepted April 19, 2018

ABSTRACT

The Qinling Orogenic Belt in central China, which resulted from continent–continent collision, is an excellent area for the study of collision-related magmatism. An integrated study including detailed field investigations, petrography, mineral and whole-rock geochemistry, zircon U–Pb–Hf–O isotopes, and geochemical modeling was carried out on the Huayang intrusive complex—a key magmatic intrusion in the South Qinling Belt—in order to understand the nature and melt source regions of magmatism associated with continental collisional orogenesis. The Huayang intrusive complex is composed of ~207–202 Ma medium to fine-grained granite, coarse to medium-grained granite of the same age, ~214–207 Ma tonalite and granodiorite, and rare ~218–213 Ma mafic xenoliths. The mafic xenoliths are characterized by enriched large ion lithophile elements, with zircon $\epsilon\text{Hf}(t)$ values of -6.8 to +4.1 and average zircon $\delta^{18}\text{O}$ of 6.1‰, which suggests that the xenoliths may represent melts derived from phlogopite-bearing lithospheric mantle. The tonalites and granodiorites exhibit high Sr/Y and La/Yb, but low Rb/Sr, with variable zircon $\epsilon\text{Hf}(t)$ values of -6.7 to +1.9 and zircon $\delta^{18}\text{O}$ values of 5.3‰ to 9.0‰. We suggest that they were derived from partial melting of Neoproterozoic, low $\delta^{18}\text{O}$ basaltic rocks with a minor input of mafic magma. These melts underwent fractional crystallization and assimilated high $\delta^{18}\text{O}$ crustal materials during magma ascent and emplacement. The coarse to medium-grained granitic rocks have zircon $\epsilon\text{Hf}(t)$ values of -7.3 to +1.5, with low zircon $\delta^{18}\text{O}$ values (average 5.7‰). The medium to fine-grained granitic rocks have zircon $\epsilon\text{Hf}(t)$ values of -14.7 to +1.1, with high zircon $\delta^{18}\text{O}$ values (average 8.4‰). Both of these granitic rock types show similar whole-rock geochemistry, with metaluminous to strongly peraluminous compositions, and are characterized by intermediate to low Sr/Y values. We propose that the coarse to medium-grained granites originated from partial melting of low $\delta^{18}\text{O}$ Neoproterozoic metabasaltic to metatonalitic rocks, and that the medium to fine-grained granites were derived from high $\delta^{18}\text{O}$ Neoproterozoic metagreywackes. Both granitic magma types experienced plagioclase-dominated fractional crystallization during magma ascent and emplacement. The data suggest that three different source materials were involved in magmatism in the South Qinling Belt: 1) the lithospheric mantle; 2) low $\delta^{18}\text{O}$ Neoproterozoic metabasaltic to tonalitic rocks, and 3) high $\delta^{18}\text{O}$ Neoproterozoic metagreywackes. Slab break-off and/or dehydration of the subducted slab may have induced the melting of

the sub-continental lithospheric mantle and caused subsequent crustal melting by heating the base of the crust. The results of this study suggest that magmatism in continental collisional orogens is not only generated by heating from radioactive element decay during crustal thickening.

Key words: crustal melting; granite; Huayang complex; mafic xenolith; Qinling orogenic belt; zircon

INTRODUCTION

Intermediate magmatism at subduction margins is relatively well understood, (Stern, 2002; Grove *et al.*, 2012; Ducea *et al.*, 2015b), although numerous uncertainties remain. There is growing consensus that the suites of magmatic rocks at arcs, ranging from basalt to rhyolite, with average andesite/dacite compositions, formed above oceanic subduction systems; the primary magmas originate in the mantle wedge due to water- and other volatiles-induced flux melting of the asthenosphere (Grove *et al.*, 2012). Those primitive melts are subsequently modified along their ascent path via a variety of differentiation mechanisms (Annen *et al.*, 2006; Bouilhol *et al.*, 2013; Ducea *et al.*, 2015b; Jagoutz & Kelemen, 2015), resulting in the classic suites of predominantly calc-alkaline magmatic rocks that form both in intra-oceanic and Andean settings.

What happens magmatically when an oceanic realm is fully consumed and collision between two continents initiates? In part, this is a limitation stemming from the scarcity of magmatically active major collisional settings on the planet today. For example, the Indo-Asian collision system is, by and large, not currently magmatically active, although it has been in its recent past (Chung *et al.*, 2005; Zhu *et al.*, 2015). There are other magmatically active margins along parts of the Tethyan collision zone (e.g. Carpathians, Caucasus Mountains) (Seghedi & Downes, 2011; Hu *et al.*, 2017a; Chapman *et al.*, 2018) which demonstrably did not involve any oceanic subduction over the past 10 Ma (Hosseinpour *et al.*, 2017) and thus are technically collisional margins. Importantly, the compositions of these collisional arcs are not very different, except in detail, from those of subduction margins (Seghedi *et al.*, 2004; Babarin, 2005; Dilek & Altunkaynak, 2007; Wang *et al.*, 2016). This observation presents a major unresolved question: are continental plates descending (subducting) just like oceanic ones and generating a similar thermo-mechanical setting for melting in a convective mantle wedge or are the similarities in arc compositions not at all related? In other words, what are the primary melt sources in continental collisional orogens and how is melting accomplished?

It appears that some of the collisional margins that generate magmatic arcs are not as simple as they were once portrayed to be, dominated or exclusively made of S-type leucogranites (and their surface equivalents) formed due to radioactive heating of previously thickened crust (Harris *et al.*, 1986; Sylvester, 1998; Bonin, 2004). Collisional arcs may be shorter lived than

subduction zones and melting may be associated with unique triggers such as slab break-off (Davies & von Blanckenburg, 1995), convective removal of the lower lithosphere of the upper plate (Gîrbacea & Frisch, 1998; Gao *et al.*, 2004; Lee *et al.*, 2006; Ducea *et al.*, 2015a, 2015b), or extensional collapse (Blasband *et al.*, 2000; Liu & Yang, 2003).

Some geologists, interested in unraveling the mechanisms of collisional magmatism, have turned their attention to extinct collisional margins of great scale. Plenty of such systems exist e.g. the Paleozoic Variscan belt of Europe (Matte, 2001; Couzinié *et al.*, 2016) and the Triassic Dabie–Qinling Orogen of China (this study) (Wu & Zheng 2013; Dong & Santosh, 2016). The problem in any one of these ancient orogens is that there are major uncertainties over when collision started, how long it lasted, and when it ended or transitioned into a distinctly different tectonic regime (such as clear-cut extensional collapse). In other words, while major magmatic products, including large batholiths, exist in these older collisional archives, the timeline of the collisional processes is inherently ambiguous. Of interest here are magmatic products that are similar to those that form in subduction zones. If an orogen transitions to bimodal magmatism, this can easily be assigned to large-scale continental extension, and thus the nature of the ‘post-collisional’ magmatism problem is easily understandable and tractable. However, for as long as intermediate composition batholiths form significantly after subduction, more nuanced petrologic and tectonic causative mechanisms are required.

Many authors have incorrectly used the magmatic record itself to fingerprint the timeline of events in the collisional history of an orogen. Consequently, there is major confusion with regard to what constitutes syn-collisional vs. post-collisional magmatism in the geologic record. Generally, the syn-collisional stage is related to thrusting and folding resulting in crustal thickening, whereas extensional faulting and basin formation, which are coeval with crustal thinning and stabilization, are included in the post-collisional setting (Liégeois, 1998; Sylvester, 1998). Slab break-off is mainly considered to be related to syn-collisional magmatism and may be a transitional process from syn-collision to post-collision (Davies & von Blanckenburg, 1995; Zhu *et al.*, 2017). One of the most difficult questions to sort out geologically in a collisional belt is the initiation and end of collision. This is well exemplified by the ongoing debate regarding the initiation of the Indo-Asian collision (globally the largest such event in

the Phanerozoic) during either the latest Cretaceous or the Cenozoic (e.g. Ding *et al.*, 2005; Cai *et al.*, 2011; Zhu *et al.*, 2015). For as long as the initiation of collision remains unresolved, it is impossible to assign with any certainty the various magmatic products to the collisional or subduction stage, especially when they appear to be compositionally similar.

With these overarching themes and uncertainties in mind, there is clearly much to learn about magmatism in the regional geologic record. To help understand the nature of magmatism in collisional orogenic systems, we have undertaken a study of the Huayang intrusive complex, the largest granitoid batholith in the South Qinling Belt (SQB). The Huayang intrusive complex was emplaced between ~214 and 195 Ma in a continental collisional setting (Liu *et al.*, 2011b; Lu *et al.*, 2016). The complex is mainly composed of medium to fine-grained biotite granite (MFG granite) and coarse to medium-grained biotite granite (CMG granite), as well as minor quartz diorite to granodiorite (Liu *et al.*, 2011b; Lu *et al.*, 2016). Its compositional diversity provides an excellent opportunity to study crustal melting processes, magmatic differentiation and interaction of melts from various sources.

We present an integrated study of the geological setting, petrology, mineralogy, whole-rock geochemistry and zircon U–Pb–Hf–O isotopic characteristics of the Huayang intrusive complex. Combined with previous studies of the Qinling Orogenic Belt, we constrain the timing of initial collision and regional extension, and explore the role of different source components during crustal melting and the mechanism of crustal melting.

GEOLOGICAL SETTING AND SAMPLING

The South Qinling Belt

The Qinling Orogenic Belt (QOB) is one of the most important continental collisional orogens in east Asia. It connects the Qilian–Kunlun Orogen to the west and the Dabie–Sulu Orogen to the east, marking the collision between the North China Craton (NCC) and the Yangtze Craton (YZC) (part of the South China Block (SCB)) (Fig. 1; Wu & Zheng, 2013). The QOB is separated from the NCC by the Lingbao–Lushan–Wuyang fault (LLWF) in the north, and from the YZC by the Mianlue–Bashan–Xiangguang fault (MBXF) in the south (Fig. 1; Dong & Santosh, 2016). Three well-documented sutures are exposed in the area, including the Kuanping suture, Shangdan suture and Mianlue suture from the north to south (Dong & Santosh, 2016). The QOB is subdivided into four tectonic domains: the southern margin of the NCC, North Qinling Belt (NQB), South Qinling Belt (SQB) and the northern margin of the YZC (Fig. 1; Dong & Santosh, 2016). Zhang *et al.* (2001) separated the QOB into eastern QOB and western QOB based on the location of the Baocheng railway (Fig. 1).

The SQB comprises several Precambrian basement blocks which are unconformably overlain by Proterozoic (Sinian) carbonates, Cambrian–Ordovician

limestones, Silurian shales, Devonian–Carboniferous limestones and Permian–Triassic sandstones (Yang *et al.*, 2012; Dong & Santosh, 2016; Hu *et al.*, 2016a). The Precambrian basement in the SQB is mainly composed of the Foping block, Douling Group, Wuguan Group, Yaolinghe Group, and Wudangshan Group (Zhang *et al.*, 2001; Shi *et al.*, 2013). Except for Neoproterozoic felsic gneisses exposed in the Douping Group (Wu *et al.*, 2014), most other Precambrian basement exposures are of Meso- to Neoproterozoic meta-volcanic and metasedimentary rocks (Ling *et al.*, 2008; Dong *et al.*, 2011, 2012; Shi *et al.*, 2013). Recent studies have reported a series of Neoproterozoic basement blocks containing subduction-related mafic to felsic intrusions in the SQB, interpreted as a Neoproterozoic subduction-accretionary complex (Hu *et al.*, 2016a; Dong *et al.*, 2017). These Precambrian basement blocks and overlying sedimentary sequences were intruded by widespread Mesozoic granitoids (Yang *et al.*, 2012; Deng *et al.*, 2016; Dong & Santosh, 2016; Hu *et al.*, 2016a, 2016b).

The Mianlue suture zone in the southern margin of the SQB consists chiefly of Paleozoic to Triassic ophiolites and arc-related volcanic rocks, which mark the Triassic continental collision between the NCC and SCB (Li *et al.*, 2007; Lai *et al.*, 2008). The intensively deformed middle Triassic and pre-Triassic strata in the Mianlue suture are dominated by folds with brittle thrusting, suggesting that collision could have begun during the Late Triassic (Li *et al.*, 2007). The age of ductile-brittle strike-slip shear deformation in the Mianlue suture zone is ~223 Ma and the metamorphic ages of the ophiolite mélanges are ~227–219 Ma (Li *et al.*, 1999; Chen *et al.*, 2010).

Middle to Upper Triassic flysch deposits in foreland basins at the northern margin of the YZC are overlain by Upper Triassic non-marine molasse (Liu *et al.*, 2005). The directions of paleocurrents in these foreland basin facies are mainly from north to south during the Late Triassic (Liu *et al.*, 2005). The Ningshan fault, a major strike-slip fault in the SQB, was proposed to be active during the Late Triassic (Li *et al.*, 2015). The Anzishan quasi-high pressure granulite in the Mianlue zone has an $^{40}\text{Ar}/^{39}\text{Ar}$ age of ~199 Ma, reflecting exhumation and extension during the Early Jurassic (Zhang *et al.*, 2002). However, E–W extending fold-thrust structures resulting from N–S compression during the Late Triassic to Early Jurassic were superimposed by a Late Jurassic–Early Cretaceous arcuate fold-thrust belt (Liu *et al.*, 2015). In general, the SQB experienced intense uplift during the Late Triassic to Early Jurassic.

Extensive early Mesozoic granitoid intrusions are exposed in the SQB (Fig. 1; Dong & Santosh, 2016). They include the Zhongchuan–Wenquan–Hejiazhuang–Mishuling intrusions in the western SQB, as well as the Guangtoushan granitoid suite, Huayang–Wulong granitoid suite, and the Dongjiangkou granitoid suites in the eastern SQB (Fig. 1; Dong *et al.*, 2011; Liu *et al.*, 2011a, 2011b; Yang *et al.*, 2012; Deng *et al.*, 2016; Hu *et al.*,

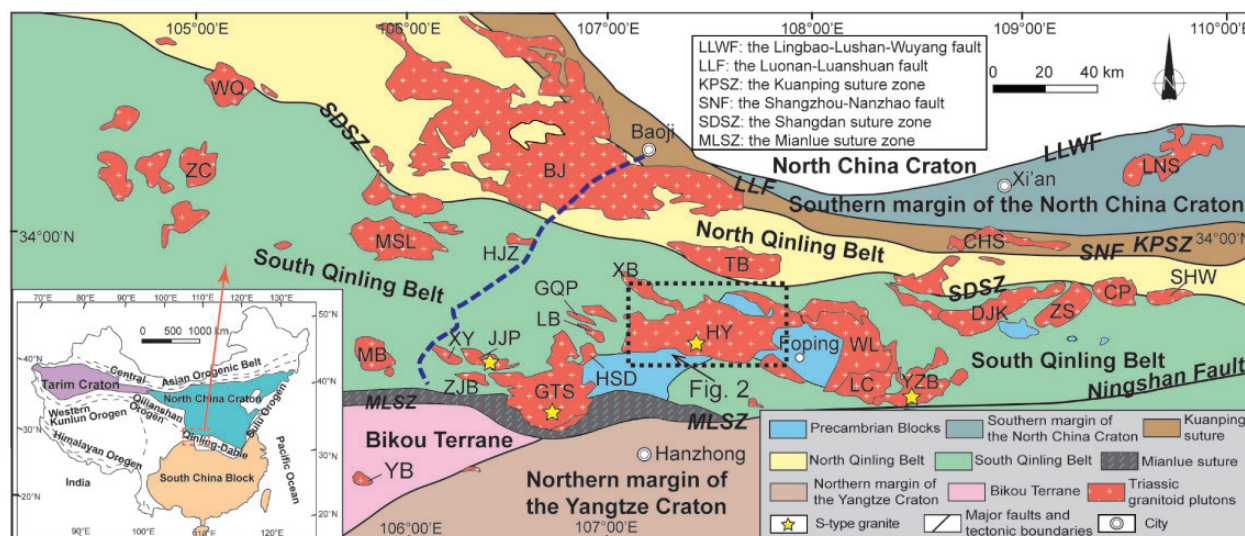


Fig. 1. Simplified geological map showing the distribution of tectonic units, sedimentary sequences, and the early Mesozoic granitoid rocks in the Qinling Orogenic Belt (modified from Dong *et al.*, 2011; Hu *et al.*, 2017b). The blue dashed line (Baoji–Chengdu railway) separates the eastern and western Qinling Orogenic Belt (Zhang *et al.*, 2001). The inset at the bottom left corner is a tectonic map showing the North China Craton, South China Craton, Tarim Craton, and major orogenic belts in China (modified from Hu *et al.*, 2017b). The study area is indicated by the dashed rectangle. Abbreviations for intrusions (from west to east): ZC, Zhongchuan; WQ, Wenquan; MSL, Mishuling; MB, Miba; HJZ, Hejiazhuang; BJ, Baoji; XY, Xinyuan; JJP, Jiangjiaping; ZJB, Zhangjiaba; GTS, Guangtoushan; HSD, Huoshaodian; LB, Liuba; GQP, Gaoqiaopu; XB, Xiba; HY, Huayang; TB, Taibai; XCH, Xichahe; LCP, Longcaoping; WL, Wulong; LC, Laocheng; YZB, Yanzhiba; DJK, Dongjiangkou; CHS, Cuihuashan; ZS, Zhashui; CP, Caoping; SHW, Shahewan; LNS, Laoniushan.

2016b, 2017b). Triassic granitoid intrusions also outcrop in the NQB (e.g. Baoji–Taibai–Cuihuashan intrusions) and south of the Mianlue suture zone (e.g. Yangba–Da’an intrusion) (Liu *et al.*, 2011a; Dong & Santosh, 2016). Geochronological data indicate that these granitoid intrusions were emplaced between c. 248 and 190 Ma, mainly c. 225–200 Ma (Qin *et al.*, 2010, 2013; Liu *et al.*, 2011a, b; Yang *et al.*, 2011, 2012, 2014; Zhang *et al.*, 2011, 2012; Wang *et al.*, 2015; Deng *et al.*, 2016; Dong & Santosh, 2016; Hu *et al.*, 2016b, 2017b). The >235 Ma granitoids are mainly considered to be subduction-related, including ~246–234 Ma andesites and ~245–238 Ma adakites (Li *et al.*, 2013a; Yang *et al.*, 2014). The 235–225 Ma granitoids are relatively scarce and exhibit significant ductile deformation fabrics and gneissic textures (Qin *et al.*, 2013; Deng & Santosh, 2016), whereas the <225 Ma granitoids in the SQB display mainly massive textures (Qin *et al.*, 2013; Deng *et al.*, 2016; Dong & Santosh, 2016; Hu *et al.*, 2016b). Sporadic late Mesozoic granitoid stocks, intruded between c. 160–140 Ma, are only exposed in the eastern SQB; these are thought to have formed in an intra-continental collisional setting (Yan *et al.*, 2014).

Huayang intrusive complex

The Huayang intrusive complex, c. 50 km north of Hanzhong city, is composed of MFG granite and CMG granite (Figs 2 and 3a). It has an exposed area of more than 1200 km² and was emplaced into sandy slates of the Devonian Liuling Group and Precambrian basement blocks (Fig. 2). The MFG granites display a transitional

contact relationship with the CMG granite, reflecting their similar emplacement ages (Fig. 3b). Apart from the biotite granites, minor granodiorites are also locally exposed and intruded by CMG granite (Fig. 3c). A particular feature of the Huayang intrusive complex is that abundant xenoliths are founded in this huge granitic batholith (Fig. 3d–f). Among those xenoliths, the rarest ones are mafic xenoliths, which are mainly coarse-grained amphibolites (Fig. 3d). Some felsic veins are observed in these mafic xenoliths (Fig. 3d). Precambrian felsic gneisses, marbles and metasedimentary rocks still exhibiting their original bedding, are also found as xenoliths in the Huayang intrusive complex (Fig. 3e–f).

We collected 36 samples from the Huayang intrusive complex, including 2 mafic xenoliths, 4 tonalites and granodiorites, 12 CMG granites and 18 MFG granites (Table 1). Mineral abundances were estimated by point counting under the microscope together with image analysis by ImageJ software. The mafic xenoliths (14HY02–5 and 16HY06–5) consist mainly of clinopyroxene (7–13%), amphibole (22–53%), plagioclase (32–34%), and biotite (3–30%), with an accessory mineral association of zircon, apatite and magnetite (Fig. 4a–c). Sample 14HY02–5 has more amphibole and less biotite relative to sample 16HY06–5 (Fig. 4a–c). The mafic xenoliths are generally unaltered based on their textures, absence of alteration minerals (e.g. chlorite, sericite, and calcite) and low loss of ignition (LOI) values.

The tonalites and granodiorites consist of quartz (22–28%), K-feldspar (6–24%), plagioclase (32–44%), biotite (13–26%) and minor muscovite, with an accessory

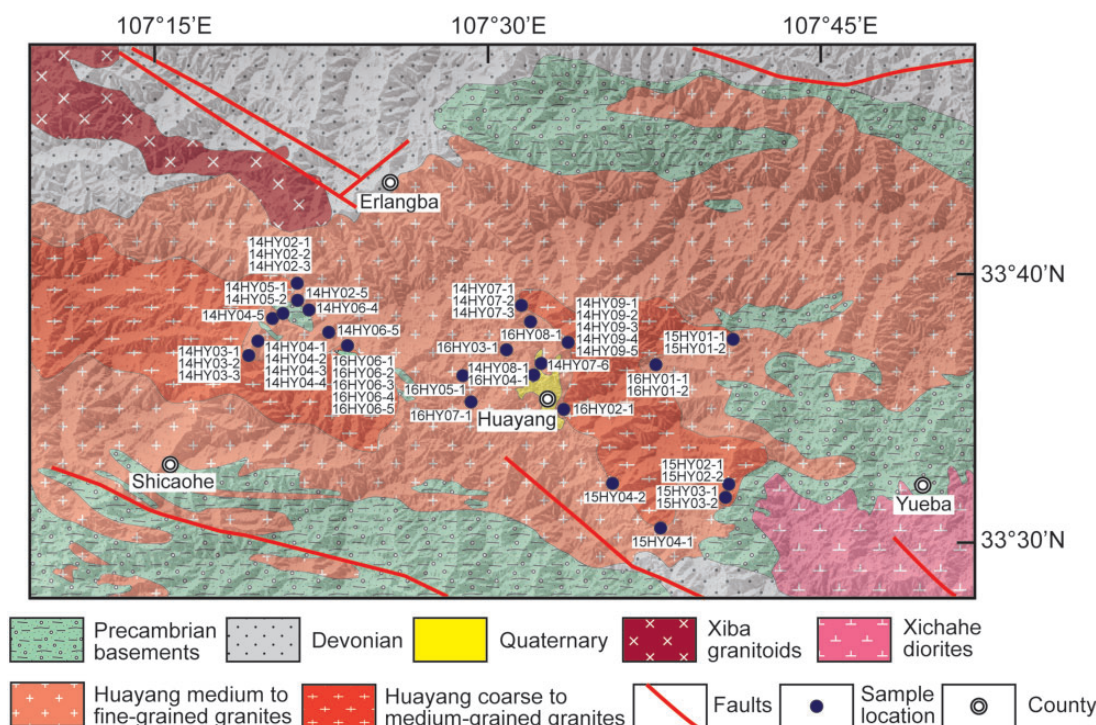


Fig. 2. Simplified geological map of the Huayang intrusive complex.

mineral association of ilmenite, apatite and zircon (Fig. 4d–f). The CMG granites are mainly composed of quartz (30–35%), K-feldspar (40–50%), plagioclase (10–18%), biotite (3–10%) and minor muscovite, with an accessory mineral assemblage of ilmenite, apatite, and zircon (Fig. 4g–i). The MFG granites are mainly composed of quartz (30–35%), K-feldspar (42–50%), plagioclase (8–16%), biotite (2–10%) and minor muscovite, with accessory ilmenite, apatite, and zircon (Fig. 4j–l). These felsic rocks show alteration to various degrees (Fig. 4d–l). Some biotites are chloritized (Fig. 4d, i–k) and some plagioclases are sericitized (Fig. 4f, h–k). Muscovites in granodiorites and granites form at the rim of biotites, and, or, within anhedral to subhedral feldspars, indicating that they may be secondary (Fig. 4f, h–l; Miller *et al.*, 1981; Ding *et al.*, 2012).

ANALYTICAL METHODS

Chemical analyses of major and trace elements were conducted upon a total of 36 representative whole-rock samples including two mafic xenoliths, four tonalites and granodiorites, 12 CMG granites and 18 MFG granites from the Huayang intrusive complex (Table 1). Fourteen samples, including two mafic xenoliths (14HY02–5 and 16HY06–5), three tonalites and granodiorites (14HY02–1, 16HY02–1, and 16HY06–3), four CMG granites (14HY04–4, 15HY03–1, 16HY06–2, and 16HY06–4) and five MFG granites (14HY04–3, 14HY06–4, 14HY06–5, 16HY04–1, and 16HY08–1) were selected for mineral composition analysis, including clinopyroxene, amphibole, feldspar, biotite, and muscovite.

Two representative mafic xenoliths (14HY02–5 and 16HY06–5), two representative tonalites and granodiorites (16HY02–1 and 16HY06–3), two representative CMG granites (14HY02–2 and 16HY06–2) and two representative MFG granites (14HY02–3 and 16HY04–1) were selected for zircon U–Pb dating and *in situ* zircon Lu–Hf isotopic analyses. Four of the samples (16HY06–5, 16HY02–1, 16HY06–2, and 16HY04–1) were analysed for *in situ* zircon O isotopes. Zircon grains were separated from the samples using conventional heavy liquid and magnetic techniques and the grains were handpicked under a binocular microscope. The sample zircons were cast in an epoxy mount. Zircon U–Pb and O isotopic standards Qinghu and Penglai were also cast in the epoxy mount. Prior to analysis, cathodoluminescence (CL) images were obtained using a FEL Quanta 200 FEG environmental scanning electron microscope (ESEM) at the Electron Microscopy Laboratory of Peking University. CL images were used to select sites for U–Pb dating, Lu–Hf and O analyses were determined.

Major and trace elements

Whole-rock samples were washed and trimmed in order to remove weathered surfaces. The samples were then pulverized and powdered in an agate mill to about 200 mesh for major and trace elements analysis. Volatile contents (e.g. CO₂ and H₂O) were determined by measuring the weight loss after heating the samples at 1050°C for 30 minutes. Major oxides were determined using an automatic X-ray fluorescence (XRF) spectrometer at the Key Laboratory of Orogenic Belts and Crustal

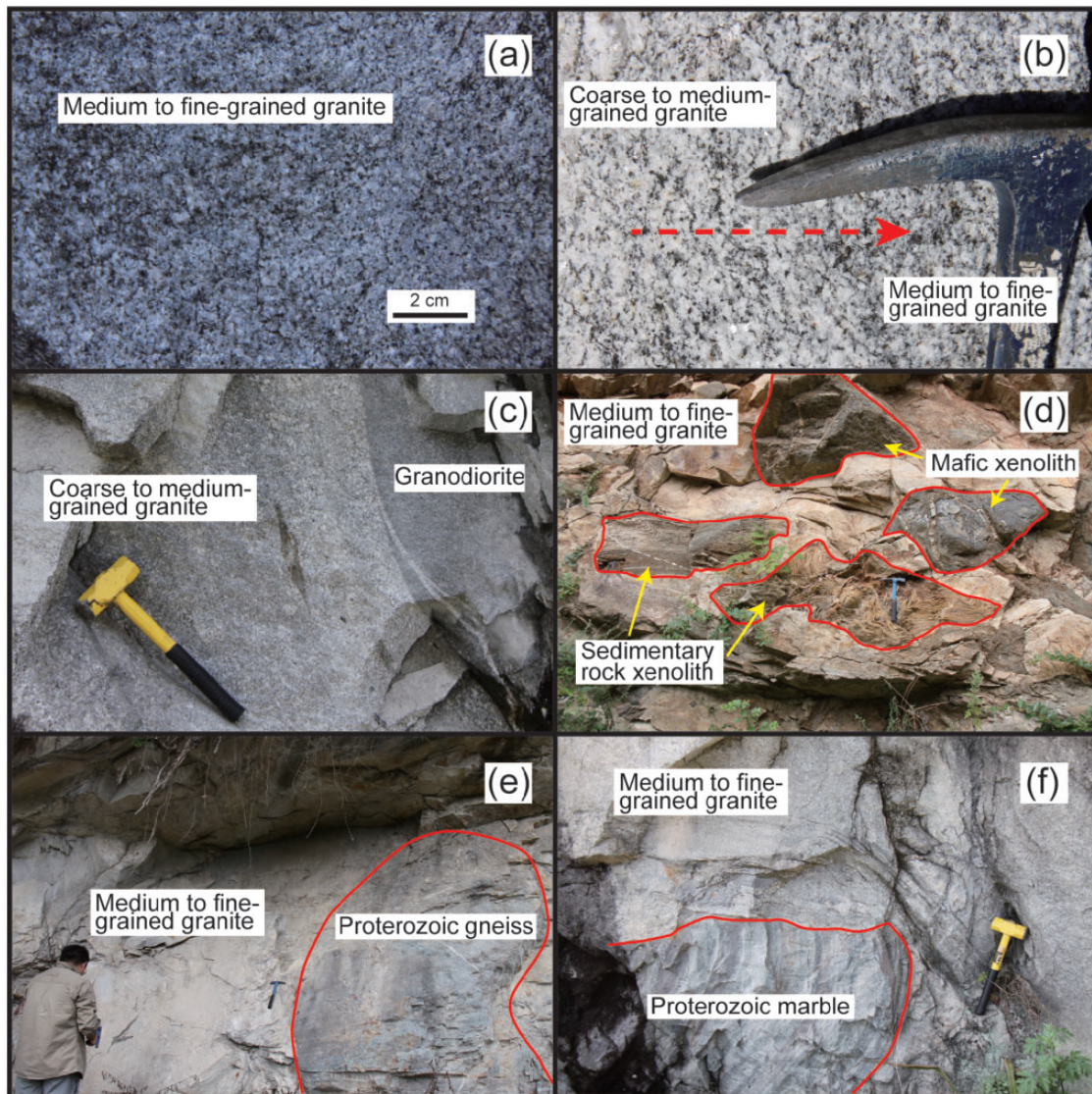


Fig. 3. Outcrop photographs of the Huayang intrusive complex showing (a) medium to fine-grained granite (MFG granite); (b) transitional contact between medium to fine-grained granite and coarse to medium-grained granite (CMG granite); (c) granodiorite intruded by CMG granite; (d) mafic xenoliths and sedimentary xenoliths in the Huayang intrusive complex; (e) Proterozoic gneiss xenolith in the Huayang intrusive complex; (f) Proterozoic marble xenolith in the Huayang intrusive complex.

Evolution, Ministry of Education, School of Earth and Space Sciences, Peking University. The analytical precision is at 0.5 % for major element oxides; detailed analytical procedures were given by Liu *et al.* (2004).

Trace elements, including rare earth elements, were analysed at the Key Laboratory of Orogenic Belts and Crustal Evolution, Ministry of Education, School of Earth and Space Sciences, Peking University. Pre-treatment of the sample powders was performed at Peking University. First, powders were weighed (25 mg) into Savillex Teflon beakers and then loaded into high-pressure bombs, adding a 1:1 HF and HNO₃ mixture. The beaker was heated at 80°C for 24 hours, and the remaining acid evaporated. Then, 1.5 ml HNO₃ and 1.5 ml HF plus 0.5 ml HClO₄ were added after the evaporation and the beakers were capped for digestion within a high-temperature oven at 180°C for 72 hours or longer, until the powders were completely

digested. Finally, the residue was diluted with 1 % HNO₃ to 50 ml for analysis. Trace elements, including rare earth elements (REE), were measured using an Agilent 7500 ICP-MS at the Key Laboratory of Orogenic Belts and Crustal Evolution, Ministry of Education, School of Earth and Space Sciences, Peking University. The international standards GSR-1 (granite), GSR-2 (andesite), GSR-9 (granodiorite), and GSR-15 (amphibolite) were used for analytical control. The measurement precision of trace elements is better than 5%.

Zircon oxygen isotopes

The *in situ* zircon oxygen isotope compositions of four samples were measured before U-Pb dating using a CAMECA IMS-1280HR secondary ion mass spectrometry (SIMS) at the Institute of Geology and Geophysics,

Table 1: The sample location and petrographic features of samples from the Huayang intrusive complex

Sample No.	Lithology	Latitude	Longitude	Texture	Mineral association
14HY02-5	Mafic xenolith	33°39'10"N	107°21'00"E	Medium to fine-grained	Cpx (7%) + Hb (53%) + Pl (34%) + Bt (3%) + Zr + Ap + Mag
16HY06-5	Mafic xenolith	33°36'59"N	107°23'10"E	Medium to fine-grained	Cpx (13%) + Hb (22%) + Pl (32%) + Bt (Phl) (30%) + Zr + Ap + Mag
14HY02-1	Tonalite	33°39'32"N	107°20'53"E	Medium to fine-grained	Qtz (20%) + Kf (6%) + Pl (46%) + Bt (26%) + Zr + Ap + Ilm
15HY03-2	Granodiorite	33°31'23"N	107°40'20"E	Fine-grained	Qtz (25%) + Kf (18%) + Pl (40%) + Bt (14%) + Ms (1%) + Zr + Ap + Ilm
16HY02-1	Granodiorite	33°34'44"N	107°32'59"E	Medium to fine-grained	Qtz (26%) + Kf (24%) + Pl (34%) + Bt (13%) + Ms (1%) + Zr + Ap + Ilm
16HY06-3	Tonalite	33°36'59"N	107°23'10"E	Fine-grained	Qtz (22%) + Kf (8%) + Pl (45%) + Bt (22%) + Zr + Ap + Ilm
14HY02-2	Biotite granite	33°39'32"N	107°20'53"E	Coarse to medium-grained	Qtz (35%) + Kf (48%) + Pl (12%) + Bt (3%) + Zr + Ap + Ilm
14HY03-3	Biotite granite	33°36'47"N	107°18'41"E	Coarse to medium-grained	Qtz (35%) + Kf (50%) + Pl (10%) + Bt (3%) + Zr + Ap + Ilm
14HY04-4	Biotite granite	33°37'29"N	107°19'10"E	Coarse to medium-grained	Qtz (32%) + Kf (46%) + Pl (13%) + Bt (5%) + Ms (2%) + Zr + Ap + Ilm
14HY04-5	Biotite granite	33°38'16"N	107°19'51"E	Coarse to medium-grained	Qtz (33%) + Kf (48%) + Pl (12%) + Bt (4%) + Ms (1%) + Zr + Ap + Ilm
14HY09-1	Biotite granite	33°37'17"N	107°33'11"E	Coarse to medium-grained	Qtz (30%) + Kf (43%) + Pl (16%) + Bt (9%) + Zr + Ap + Ilm
14HY09-4	Biotite granite	33°37'17"N	107°33'11"E	Coarse to medium-grained	Qtz (34%) + Kf (48%) + Pl (11%) + Bt (4%) + Zr + Ap + Ilm
14HY09-5	Biotite granite	33°37'17"N	107°33'11"E	Coarse to medium-grained	Qtz (31%) + Kf (45%) + Pl (15%) + Bt (7%) + Zr + Ap + Ilm
15HY01-1	Biotite granite	33°32'52"N	107°40'46"E	Coarse to medium-grained	Qtz (31%) + Kf (45%) + Pl (13%) + Bt (7%) + Ms (2%) + Zr + Ap + Ilm
15HY03-1	Biotite granite	33°31'23"N	107°40'20"E	Coarse to medium-grained	Qtz (32%) + Kf (46%) + Pl (13%) + Bt (6%) + Ms (1%) + Zr + Ap + Ilm
16HY06-2	Biotite granite	33°36'59"N	107°23'10"E	Coarse to medium-grained	Qtz (30%) + Kf (40%) + Pl (18%) + Bt (10%) + Ms (1%) + Zr + Ap + Ilm
16HY06-4	Biotite granite	33°36'59"N	107°23'10"E	Coarse to medium-grained	Qtz (34%) + Kf (48%) + Pl (11%) + Bt (4%) + Ms (1%) + Zr + Ap + Ilm
16HY07-1	Biotite granite	33°38'04"N	107°31'17"E	Coarse to medium-grained	Qtz (33%) + Kf (47%) + Pl (13%) + Bt (4%) + Ms (1%) + Zr + Ap + Ilm
14HY02-3	Biotite granite	33°39'32"N	107°20'53"E	Medium to fine-grained	Qtz (33%) + Kf (46%) + Pl (14%) + Bt (4%) + Ms (1%) + Zr + Ap + Ilm
14HY04-1	Biotite granite	33°37'20"N	107°19'06"E	Medium to fine-grained	Qtz (34%) + Kf (47%) + Pl (12%) + Bt (4%) + Ms (1%) + Zr + Ap + Ilm
14HY04-3	Biotite granite	33°37'29"N	107°19'10"E	Medium to fine-grained	Qtz (32%) + Kf (43%) + Pl (16%) + Bt (8%) + Zr + Ap + Ilm
14HY05-2	Biotite granite	33°38'31"N	107°20'30"E	Medium to fine-grained	Qtz (30%) + Kf (42%) + Pl (15%) + Bt (10%) + Zr + Ap + Ilm
14HY06-4	Biotite granite	33°38'31"N	107°21'25"E	Medium to fine-grained	Qtz (33%) + Kf (46%) + Pl (13%) + Bt (6%) + Zr + Ap + Ilm
14HY06-5	Biotite granite	33°37'40"N	107°22'19"E	Medium to fine-grained	Qtz (33%) + Kf (45%) + Pl (13%) + Bt (6%) + Ms (1%) + Zr + Ap + Ilm
14HY07-1	Biotite granite	33°38'39"N	107°31'12"E	Medium to fine-grained	Qtz (34%) + Kf (48%) + Pl (12%) + Bt (4%) + Zr + Ap + Ilm
14HY07-3	Biotite granite	33°38'22"N	107°31'04"E	Medium to fine-grained	Qtz (34%) + Kf (50%) + Pl (11%) + Bt (3%) + Zr + Ap + Ilm
14HY07-6	Biotite granite	33°36'22"N	107°31'55"E	Medium to fine-grained	Qtz (35%) + Kf (50%) + Pl (8%) + Bt (2%) + Ms (1%) + Zr + Ap + Ilm
14HY08-1	Biotite granite	33°35'46"N	107°31'58"E	Medium to fine-grained	Qtz (34%) + Kf (48%) + Pl (10%) + Bt (4%) + Ms (1%) + Zr + Ap + Ilm
15HY01-2	Biotite granite	33°32'52"N	107°40'46"E	Medium to fine-grained	Qtz (33%) + Kf (46%) + Pl (13%) + Bt (4%) + Ms (1%) + Zr + Ap + Ilm
15HY02-1	Biotite granite	33°31'53"N	107°40'29"E	Medium to fine-grained	Qtz (30%) + Kf (42%) + Pl (16%) + Bt (8%) + Ms (2%) + Zr + Ap + Ilm
15HY04-2	Biotite granite	33°31'55"N	107°35'12"E	Medium to fine-grained	Qtz (33%) + Kf (45%) + Pl (13%) + Bt (6%) + Ms (1%) + Zr + Ap + Ilm
15HY04-1	Biotite granite	33°36'26"N	107°37'10"E	Medium to fine-grained	Qtz (34%) + Kf (45%) + Pl (13%) + Bt (5%) + Ms (1%) + Zr + Ap + Ilm
16HY03-1	Biotite granite	33°37'00"N	107°30'23"E	Medium to fine-grained	Qtz (34%) + Kf (45%) + Pl (15%) + Bt (3%) + Ms (1%) + Zr + Ap + Ilm
16HY04-1	Biotite granite	33°35'56"N	107°31'46"E	Medium to fine-grained	Qtz (34%) + Kf (45%) + Pl (14%) + Bt (4%) + Ms (1%) + Zr + Ap + Ilm
16HY05-1	Biotite granite	33°36'01"N	107°28'35"E	Medium to fine-grained	Qtz (34%) + Kf (45%) + Pl (14%) + Bt (3%) + Ms (2%) + Zr + Ap + Ilm
16HY08-1	Biotite granite	33°38'04"N	107°31'17"E	Medium to fine-grained	Qtz (33%) + Kf (42%) + Pl (15%) + Bt (7%) + Ms (1%) + Zr + Ap + Ilm

Note: Qtz, quartz; Kf, K-feldspar; Pl, Plagioclase; Cpx, Clinopyroxene; Hb, Hornblende; Bt, Biotite; Ms, Muscovite; Phl, Phlogopite; Ap, Apatite; Zr, Zircon; Mag, Magnetite; Ilm, Ilmenite.

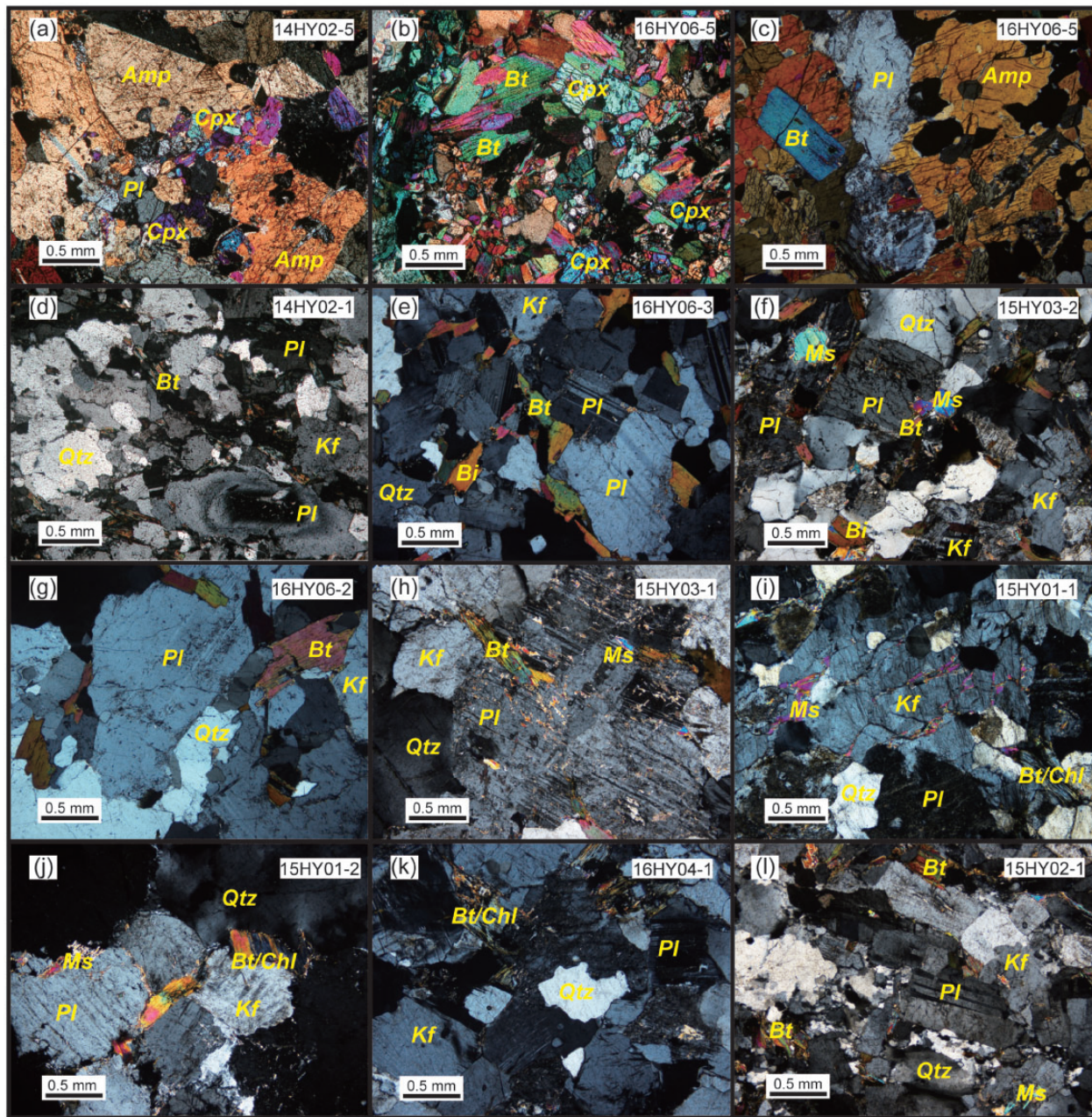


Fig. 4. Photomicrographs of the Huayang intrusive complex showing: (a) mafic xenolith (14HY02-5) containing clinopyroxene, amphibole and plagioclase; (b) mafic xenolith (16HY06-5) containing clinopyroxene and biotite; (c) mafic xenolith (16HY06-5) containing amphibole, plagioclase and biotite; (d) tonalite containing plagioclase with reverse zoning; (e) tonalite containing mainly plagioclase and biotite; (f) granodiorite containing plagioclase and biotite with muscovite in the plagioclase and next to biotite; (g) CMG granite containing plagioclase and biotite; (h) CMG granite containing altered plagioclase with muscovite; (i) muscovite in the CMG granite along a crevice; (j) MFG granite containing K-feldspar and altered biotite (chlorite) with muscovite next to plagioclase; (k) MFG granite containing mainly feldspar and quartz with altered biotite; (l) MFG granite containing feldspar and biotite with anhedral muscovite. Mineral abbreviations: Cpx, clinopyroxene; Amp, amphibole; Bt, biotite; Pl, plagioclase; Kf, potassic feldspar; Q, quartz; Ms, muscovite; Chl, chlorite.

Chinese Academy of Science in Beijing (IGGCAS). The detailed analytical procedures were similar to those described by Li *et al.* (2009). The primary Cs⁺ ion beam was accelerated at 10 kV, with a beam size of 10 × 15 μm. The measured ¹⁸O/¹⁶O ratios were normalized to the Vienna Standard Mean Ocean Water (VSMOW, ¹⁸O/¹⁶O = 0.0020052). The measured oxygen isotopic data were corrected for instrumental mass

fractionation (IMF) using the Penglai zircon standard with $\delta^{18}\text{O}_{\text{VSMOW}} = 5.31 \pm 0.10\text{‰}$ (2σ; Li *et al.*, 2010b) (measured $\delta^{18}\text{O}_{\text{VSMOW}} = 5.27 \pm 0.24\text{‰}$, 2σ, n = 20). The internal precision of ¹⁸O/¹⁶O ratios is ca 0.2‰ (2SE) from 20 cycles of measurement. Fourteen measurements of the Qinghu zircon as an unknown during the course of this study yielded a weighted mean $\delta^{18}\text{O} = 5.42 \pm 0.37\text{‰}$ (2σ), which is consistent within

error with the reported value of $5.39 \pm 0.22\%$ (2σ) (Li *et al.*, 2013b).

Zircon U–Pb dating

The U–Th–Pb elemental and isotopic composition of three samples (14HY02–5, 14HY02–2, and 14HY02–3) were analyzed using an Agilent 7500 quadrupole-based inductively coupled plasma mass spectrometer (ICP–MS) equipped with a GeoLas 193 nm laser (MicroLas, Göttingen) at the Key Laboratory of Orogenic Belts and Crustal Evolution, Ministry of Education, Peking University. The laser beam is 32 μm and the ablated depth is 20–40 μm , with a hit rate of 5 Hz and an energy density of 6 J/cm². The ablated material was delivered to the ICP–MS by He (0.46 L/min; carrier gas) and Ar (0.96 L/min; auxiliary gas) gas. Each analysis consists of 20 s blank time and 60 s ablation time. Zircon 91500 (primary standard) and Plešovice (secondary standard) were used as the standard for zircon U–Pb geochronological analyses. NIST 610 (primary standard), NIST 612 (secondary standard) and NIST 614 (secondary standard) were used as standards for trace elements (U, Th and Pb). ²⁰⁷Pb/²⁰⁶Pb, ²⁰⁷Pb/²³⁵U and ²⁰⁶Pb/²³⁸U ratios and corresponding uncertainties were calculated using the GLITTER program (van Achterbergh *et al.*, 2001) and common Pb was corrected using the method proposed by Anderson (2002). Reported uncertainties (1σ) of the ²⁰⁶Pb/²³⁸U ratio include the uncertainties from within-spot analysis and the reproducibility of standard zircon 91500 within the analytical session. The age of the primary standard 91500 zircon has been determined as 1063 ± 5 Ma (2σ , $n = 15$; ²⁰⁶Pb/²³⁸U age) in this study (the recommended ²⁰⁶Pb/²³⁸U age is 1065 ± 0.6 Ma; 2σ ; Wiedenbeck *et al.*, 1995), and the secondary standard Plešovice zircon was dated at 338 ± 2 Ma (2σ , $n = 8$; ²⁰⁶Pb/²³⁸U age) in this study (the recommended ²⁰⁶Pb/²³⁸U age is 337 ± 0.4 Ma; 2σ ; Sláma *et al.*, 2008). Weighted mean age calculations and concordia plots were made using Isoplot (ver 3.0) (Ludwig, 2003).

The other five samples (16HY06–5, 16HY02–1, 16HY06–3, 16HY06–2, and 16HY04–1) were dated using the same CAMECA IMS-1280HR SIMS at the IGGCAS. Detailed procedures can be found in Li *et al.* (2009, 2013b). The primary O^{2–} ion beam spot is about 20 \times 30 μm in size. Positive secondary ions were extracted with a 10 kV potential. Analyses of the standard zircon Plešovice (primary standard; ²⁰⁶Pb/²³⁸U age = 337 Ma, Sláma *et al.*, 2008) were interspersed with unknown grains. In order to monitor the external uncertainties of SIMS U–Pb zircon dating calibrated against the Plešovice standard, an in-house zircon standard Qinghu zircon (secondary standard) (²⁰⁶Pb/²³⁸U age = 159.5 Ma; Li *et al.*, 2013b) was analysed as an unknown together with the other unknown zircons. Pb/U calibration was performed relative to zircon standard Qinghu; U and Th concentrations were calibrated against zircon standard 91500 (Th = 29 ppm and U = 81 ppm; Wiedenbeck *et al.*, 1995). Nine

measurements on Qinghu zircon yield a weighted mean ²⁰⁶Pb/²³⁸U age of 160.6 ± 1.6 Ma (2σ , $n = 9$), which is identical within error with the recommended value of 159.5 ± 0.2 Ma (2σ ; Li *et al.*, 2013b). A long-term uncertainty of 1.5% (1 s RSD) for ²⁰⁶Pb/²³⁸U measurements of the standard zircons was propagated to the unknowns (Li *et al.*, 2010a), despite the fact that the measured ²⁰⁶Pb/²³⁸U error in a specific session is generally $<1\%$ (1 s RSD). Measured compositions were corrected for common Pb using non-radiogenic ²⁰⁴Pb. Corrections are sufficiently small to be insensitive to the choice of common Pb composition, and an average of present-day crustal compositions (Stacey & Kramers, 1975) is used for the common Pb assuming that the common Pb is largely surface contamination introduced during sample preparation. Data reduction was carried out using the Isoplot (ver 3.0) (Ludwig, 2003).

Zircon Lu–Hf isotopes

In situ Lu–Hf analyses for zircons were carried out using a Neptune MC–ICP–MS, equipped with a GeoLas 193 nm laser (MicroLas, Göttingen). All eight samples were analysed at the State Key Laboratory of Geological Process and Mineral Resources (GPMR), China University of Geosciences, Wuhan. The instrumental conditions and data acquisition were described by Hu *et al.* (2012). The analyses were conducted with a spot size of 44 μm , a hit rate of 8 Hz and laser energy density of 5.3 J/cm². Harvard zircon 91500 (primary standard), GJ-1 (secondary standard) and Temora 2 (secondary standard) were used as references during analysis, and Harvard zircon 91500 was used as the external standard for analyses. Off-line selection and integration of analytic signals, as well as isobaric interference and mass fractionation correction of Lu–Hf isotopic ratios, were performed using ICP–MS–DataCal (Liu *et al.*, 2010). The ¹⁷⁶Hf/¹⁷⁷Hf isotopic ratios of standard zircons are 0.282308 ± 13 for 91500 (1σ , $n = 30$; the recommended value is 0.282308 ± 3 ; Blichert-Toft, 2008); 0.282019 ± 21 for GJ-1 (1σ , $n = 10$; the recommended value is 0.282013 ± 11 ; Hu *et al.*, 2012); and 0.282689 ± 22 for Temora 2 (1σ , $n = 10$; the recommended value is 0.282686 ± 4 ; Woodhead & Hergt, 2005).

Mineral compositions

Quantitative analyses of certain minerals were carried out using a CAMECA SX100 electron microprobe at the Electron Microprobe Laboratory, Lunar and Planetary Laboratory, University of Arizona. All polished thin sections were carbon-coated before analysis. The operating conditions for clinopyroxene, amphibole, plagioclase and muscovite were 15 kV accelerating voltage with a beam current of 10 nA for Na, K, and F, and 20 nA for Si, Mg, Al, Ca, Fe, Mn, Ti, Cr, and Cl. The operating conditions for K-feldspar were 5 kV accelerating voltage with a beam current of 20 nA. The beam diameter is 5 μm for all operating conditions. The standards used for clinopyroxene, amphibole, plagioclase and

muscovite were albite (Na), K-feldspar (K), magnesium fluoride (F), olivine (Si, Mg), anorthite (Al, Ca), fayalite (Fe), rhodochrosite (Mn), rutile (Ti), chromite (Cr) and scapolite (Cl). The standards used for K-feldspar were albite (Na), K-feldspar (K, Si), magnesium fluoride (F), olivine (Mg), anorthite (Al, Ca), fayalite (Fe), rhodochrosite (Mn), rutile (Ti), chromite (Cr) and scapolite (Cl). The accuracy was better than 5% and precision is better than 1%.

RESULTS

Zircon U–Pb ages, and Hf–O isotopes

The analytical results of the U–Pb isotope analysis and calculated ages are listed in [Supplementary Data Table S1](#); [supplementary data](#) are available for downloading at <http://www.petrology.oxfordjournals.org>, the Lu–Hf isotope and calculated relevant parameters are listed in [Supplementary Data Table S2](#), and the O isotope data are listed in [Supplementary Data Table S3](#).

As shown in representative CL images ([Fig. 5](#)), all zircon grains exhibit similar morphological characteristics. They generally have round to long-prismatic shapes, with lengths between 100 and 400 μm and length/width ratios of 1:1 to 4:1 ([Fig. 5](#)). The zircon grains in the CMG granites are clearly larger than those in tonalites, granodiorites and MFG granites ([Fig. 5](#)). CL images of zircon grains from the mafic xenoliths show broad zoning and oscillatory zoning, and some have dark, poorly developed oscillatory zoning with bright rims, suggesting that zircon grains with a magmatic origin have experienced recrystallization and new metamorphic growth after magmatic crystallization ([Fig. 5](#); [Corfu et al., 2003](#)). CL images of zircon grains from granitoid rocks show clear inner structures of broad zoning and oscillatory zoning, but some zircons show chaotic textures indicating late-magmatic recrystallization ([Fig. 5](#); [Corfu et al., 2003](#)). Zircons from the mafic xenoliths have Th and U contents ranging from 19 to 1190 ppm and 41 to 1020 ppm, respectively, with Th/U ratios of 0.24–1.33 ([Supplementary Data Table S1](#)). Zircons grains from the granitoid samples exhibit higher Th (35–4795 ppm) and U (89–9720 ppm) contents, with Th/U ratios of 0.02–1.79 ([Supplementary Data Table S1](#)). The high U and low Th/U ratio of some zircons with chaotic or convoluted textures are primarily related to late-magmatic hydrothermal events ([Figs 4 and 5](#)) ([Rubatto, 2002](#); [Harley et al., 2007](#)). Most zircons, however, are of magmatic origin, based on their morphologies, inner structures and Th/U ratios ([Rubatto, 2002](#); [Corfu et al., 2003](#)).

A total of twenty zircon spots were analysed on twenty zircon grains for U–Pb dating of mafic xenolith sample 16HY06–5 ([Supplementary Data Table S1](#)). All analyses plot on the concordia curve, yielding a weighed mean $^{206}\text{Pb}/^{238}\text{U}$ age of 213 ± 1 Ma (MSWD = 0.42) ([Fig. 6a](#)), which is taken as the magmatic crystallization age of this sample. Fifteen initial Hf isotopic analyses give $\epsilon\text{Hf}(t)$ values of -0.8 to $+4.1$ ([Fig. 7](#); [Supplementary Data Table S2](#)). Fifteen analyses of O isotope

compositions are in the range of 5.9‰ to 6.4‰ , with an average of $6.1 \pm 0.3\text{‰}$ (2σ) ([Fig. 8](#); [Supplementary Data Table S3](#)).

Thirty zircon grains from mafic xenolith sample 14HY02–5 were analysed and four of them (spots #16, #18, #25, and #27) fall below the concordia curve, indicating possible Pb loss. The remaining twenty-six give a weighted average $^{206}\text{Pb}/^{238}\text{U}$ age of 218 ± 1 Ma (MSWD = 0.66) ([Fig. 6b](#); [Supplementary Data Table S1](#)). Fifteen of the zircons were selected for Hf isotope analysis, yielding $\epsilon\text{Hf}(t)$ values of -6.8 to -4.7 after correction to their magmatic crystallization age of 218 Ma ([Fig. 7](#); [Supplementary Data Table S2](#)).

Twenty zircon grains from granodiorite sample 16HY02–1 were selected for U–Pb isotopic analyses ([Supplementary Data Table S1](#)). One analysis (spot #9) gave an older apparent $^{206}\text{Pb}/^{238}\text{U}$ age of 229 ± 4 Ma, suggesting an inherited origin, and another one (spot #14) gave a younger apparent $^{206}\text{Pb}/^{238}\text{U}$ age of 194 ± 3 Ma, which may represent a later thermal event ([Fig. 6c](#)). The remaining eighteen analyses yield a weighted mean $^{206}\text{Pb}/^{238}\text{U}$ age of 210 ± 2 (MSWD = 1.16), which is interpreted to be the magmatic crystallization age ([Fig. 6c](#)). Among these, fifteen grains were analysed for Hf–O isotopes ([Supplementary Data Tables S2 and S3](#)). The 229 Ma zircon has an $\epsilon\text{Hf}(t)$ value of -37.3 , with $\delta^{18}\text{O}_{\text{VSMOW}}$ value of 6.7‰ ([Figs 7 and 8](#)). The 194 Ma zircon yields an initial $\epsilon\text{Hf}(t)$ value of -1.7 , with a $\delta^{18}\text{O}_{\text{VSMOW}}$ value of 6.2‰ ([Figs 7 and 8](#)). The remaining thirteen analyses yield $\epsilon\text{Hf}(t)$ values of -4.7 to $+1.9$ after correction to the age of 210 Ma ([Fig. 7](#)); their $\delta^{18}\text{O}_{\text{VSMOW}}$ values vary from 5.3‰ to 9.0‰ , with an average of $6.9 \pm 2.7\text{‰}$ (2σ) ([Fig. 8](#)).

A total of twenty spots were analysed on twenty zircon grains for U–Pb dating of tonalite sample 16HY06–3 ([Supplementary Data Table S1](#)). Among these, three analyses (spots #10, #14, and #20) fall below the concordia curve, indicating possible Pb loss. One analysis gave an older apparent $^{206}\text{Pb}/^{238}\text{U}$ age of 217 ± 3 Ma, with an $\epsilon\text{Hf}(t)$ value of -3.1 , indicating that it may be an inherited zircon ([Figs 6 and 7](#)). The remaining sixteen analyses yielded a weighed mean $^{206}\text{Pb}/^{238}\text{U}$ age of 207 ± 2 Ma (MSWD = 0.81), which is taken as the crystallization age ([Fig. 6d](#)). Fourteen of these zircons were analysed for Hf isotopes and yield $\epsilon\text{Hf}(t)$ values of -6.7 to $+1.9$ ([Fig. 7](#)).

Twenty spots were analysed on twenty zircon grains for CMG granite sample 16HY06–2 ([Supplementary Data Table S1](#)), and one of the analyses (spot #11) gave an older apparent $^{206}\text{Pb}/^{238}\text{U}$ age of 214 ± 3 Ma, suggesting an inherited origin ([Fig. 6e](#)). The remaining nineteen analyses yielded a weighted mean $^{206}\text{Pb}/^{238}\text{U}$ age of 207 ± 1 Ma (MSWD = 0.42) ([Fig. 6e](#)), which is interpreted as the crystallization age of this rock. The 214 Ma zircon has an $\epsilon\text{Hf}(t)$ value of $+2.1$, with a $\delta^{18}\text{O}_{\text{VSMOW}}$ value of 5.9‰ ([Figs 7 and 8](#); [Supplementary Data Tables S2 and S3](#)). Fourteen analyses gave initial $\epsilon\text{Hf}(t)$ values of -3.0 to $+1.5$ ([Fig. 7](#); [Supplementary Data Table S2](#)). The O isotope compositions of these

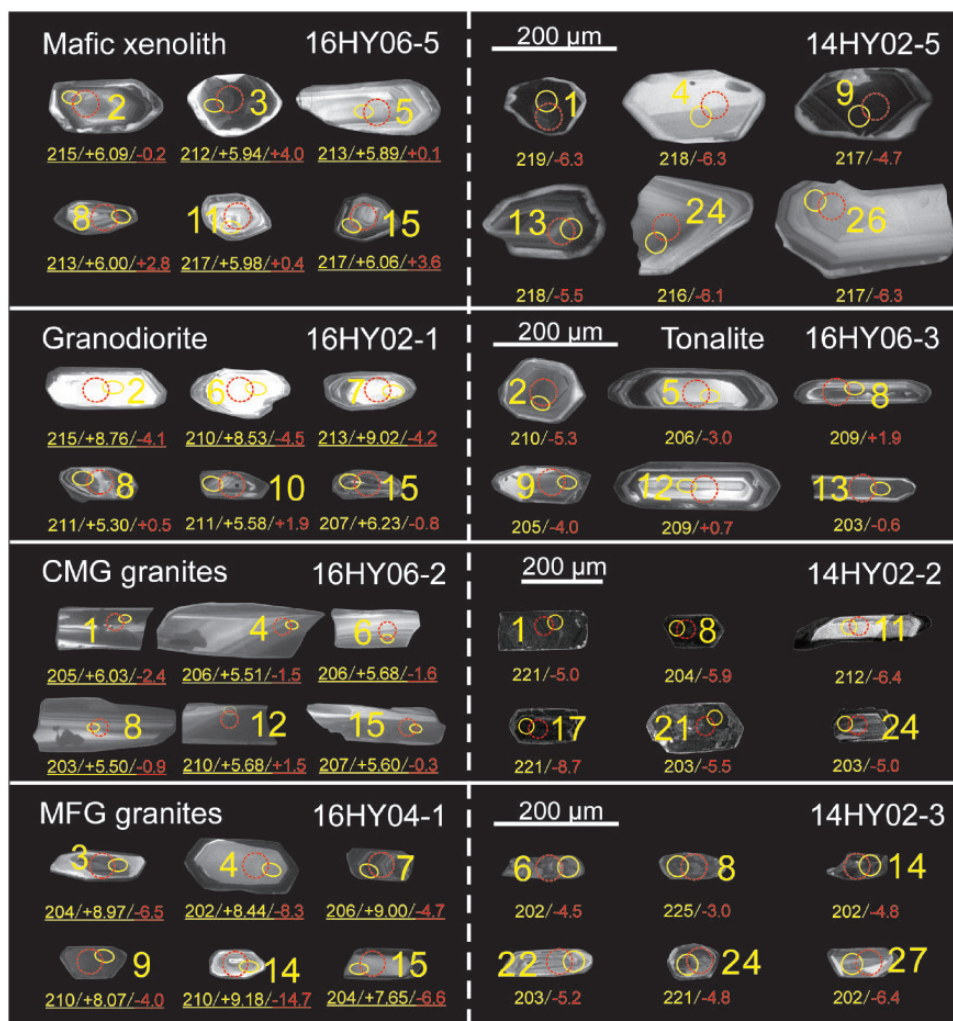


Fig. 5. Cathodoluminescence images of representative zircon grains from samples of mafic xenoliths (16HY06-5 and 14HY02-5), tonalites and granodiorites (16HY02-1 and 16HY06-3), CMG granites (16HY06-2 and 14HY02-2), and MFG granites (16HY04-1 and 14HY02-3) showing their internal structures and analysed locations. The yellow circles indicate zircon *in situ* U-Pb and O isotope analyses with beam diameters of 32 μm for LA-ICP-MS (U-Pb), 20 \times 30 μm for SIMS (U-Pb), and 15 \times 20 μm for SIMS (O isotopes), respectively. The red dashed circles indicate zircon *in situ* Lu-Hf isotope analyses with beam diameter of 44 μm . Apparent ages (in yellow), $\delta^{18}\text{O}_{\text{VSMOW}}$ (in yellow with underline), and $\epsilon_{\text{Hf}}(t)$ (in red) values are also shown. The white scale bars are 200 μm for each row. Numbers are equivalent to spot analyses given in [Supplementary Data Tables S1-S3](#).

fourteen zircons are in the range of 5.2‰ to 6.3‰, with an average of $5.7 \pm 0.5\%$ (2σ) (Fig. 8; [Supplementary Data Table S3](#)).

A total of twenty-nine zircon grains from CMG granite 14HY02-2 were selected for U-Pb isotopic analysis ([Supplementary Data Table S1](#)). Among these grains, one analysis (spot #28) yielded the oldest apparent $^{206}\text{Pb}/^{238}\text{U}$ age of 743 ± 13 Ma, and eight analyses gave an older weighted mean $^{206}\text{Pb}/^{238}\text{U}$ age of 218 ± 4 Ma (MSWD = 1.2) (Fig. 6f). The remaining twenty analyses yielded a weighted mean $^{206}\text{Pb}/^{238}\text{U}$ age of 204 ± 2 Ma (MSWD = 0.06), interpreted here as the crystallization age of this rock (Fig. 6f). Twenty zircon grains were selected for Hf isotopic analysis ([Supplementary Data Table S2](#)). The 743 Ma zircon gave an $\epsilon_{\text{Hf}}(t)$ value of -10.8 (Fig. 7). Four 218 Ma zircons yielded initial $\epsilon_{\text{Hf}}(t)$ values of -8.8 to -5.1 (Fig. 7). The remaining fifteen

analyses, corrected to the magmatic crystallization age of 204 Ma, gave $\epsilon_{\text{Hf}}(t)$ values of -7.3 to -3.7 (Fig. 7).

Twenty spots were analysed on nineteen zircon grains from MFG granite sample 16HY04-1 ([Supplementary Data Table S1](#)); one analysis (spot #14) fell below the concordia curve, probably indicating Pb loss. Two of analyses gave older apparent $^{206}\text{Pb}/^{238}\text{U}$ ages of 358 ± 5 Ma and 214 ± 3 Ma, indicating their inherited origin (Fig. 6g). The remaining seventeen analyses yielded a weighted mean $^{206}\text{Pb}/^{238}\text{U}$ age of 206 ± 2 Ma (MSWD = 0.98) (Fig. 6g), which is interpreted to be the crystallization age. The older 358 Ma zircon has an $\epsilon_{\text{Hf}}(t)$ value of -2.5, and its $\delta^{18}\text{O}_{\text{VSMOW}}$ value is 8.1‰ (Figs 7 and 8; [Supplementary Data Tables S2 and S3](#)). The remaining fourteen analyses exhibit initial $\epsilon_{\text{Hf}}(t)$ values of -14.7 to -4.0 (Fig. 7; [Supplementary Data Table S2](#)). The O isotope compositions of these fourteen zircons are in the range

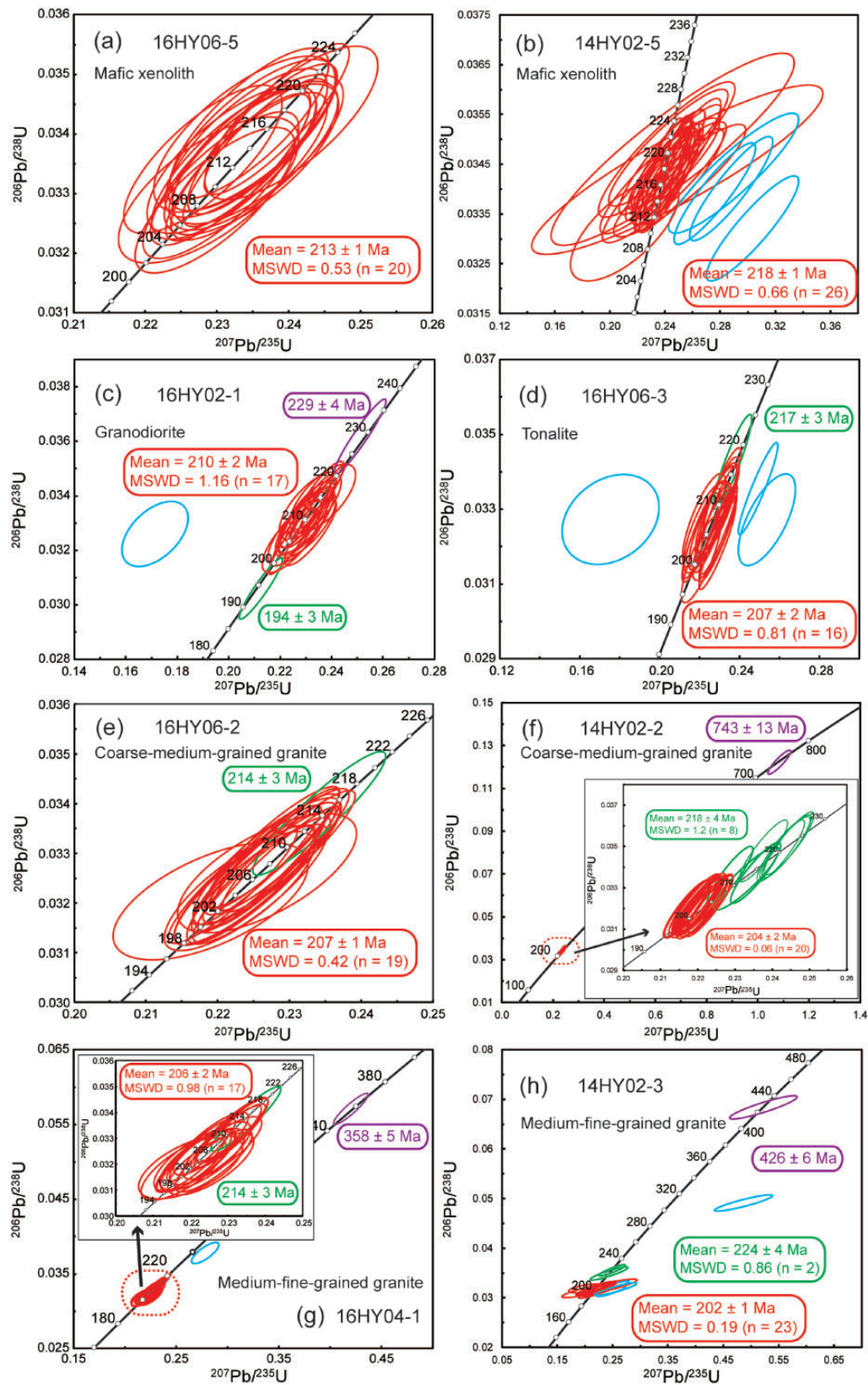


Fig. 6. U–Pb isotopic data for representative samples from the Huayang intrusive complex. (a) and (b) mafic xenoliths (16HY06–5 and 14HY02–5), (c) and (d) tonalites and granodiorites (16HY02–1 and 16HY06–3), (e) and (f) CMG granites (16HY06–2 and 14HY02–2), and (g) and (h) MFG granites (16HY04–1 and 14HY02–3). Data point error ellipses are 2σ . Analytical data are listed in Supplementary Data Table S1.

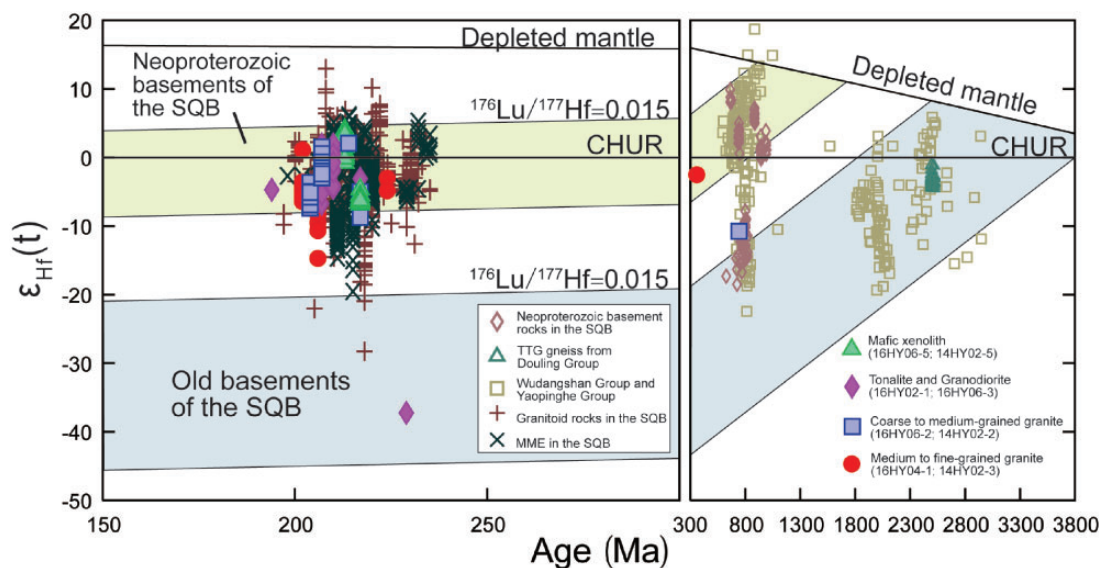


Fig. 7. Zircon Hf isotopic characteristics for rocks in the Huayang intrusive complex and other granitoid intrusions in the SQB. Plots of zircon $\epsilon_{\text{Hf}}(t)$ values versus crystallization ages for eight dated samples. The Archean basement of the SQB is defined based on initial Hf isotope ratios from magmatic zircons in the Douling Archean TTG gneisses and detrital zircons from the Wudangshan and Yaolinghe Groups (after Wang *et al.*, 2013; Wu *et al.*, 2014) at assumed $^{176}\text{Lu}/^{177}\text{Hf}$ ratios of 0.015. The Neoproterozoic basement of the SQB is defined based on initial Hf isotope ratios from detrital zircons in the Wudangshan and Yaolinghe Groups and newly-found intrusive rocks in the SQB (after Wang *et al.*, 2013; Hu *et al.*, 2016a) at assumed $^{176}\text{Lu}/^{177}\text{Hf}$ ratios of 0.015. Zircon $\epsilon_{\text{Hf}}(t)$ values of granitoid rocks and MME in the SQB are constructed using data from the following: Qin *et al.* (2009, 2010, 2013); Jiang *et al.* (2010, 2012); Wang *et al.* (2011); Yang *et al.* (2011, 2012b); Ping *et al.* (2013); Deng *et al.* (2016); Hu *et al.* (2016b, 2017b). Reference lines representing meteoritic Hf evolution (CHUR) and that of the depleted mantle (DM) are from Blichert-Toft & Albarède (1997) and Griffin *et al.* (2000), respectively. Analytical data are listed in Supplementary Data Table S2.

7.5‰ to 9.3‰, with an average of $8.4 \pm 1.1\%$ (2 σ) (Fig. 8; Supplementary Data Table S3).

Thirty zircon grains from MFG granite 14HY02–3 were selected for U–Pb isotopic analysis (Supplementary Data Table S1); four analyses (spots #3, #11, #16, and #29) fell below the concordia curve, indicating possible Pb loss. One analysis gave an older apparent $^{206}\text{Pb}/^{238}\text{U}$ age of 426 ± 6 Ma, and two analyses yielded an older weighted mean $^{206}\text{Pb}/^{238}\text{U}$ age of 224 ± 4 Ma (MSWD = 0.86) (Fig. 6h). The remaining twenty-three analyses yielded a weighted mean $^{206}\text{Pb}/^{238}\text{U}$ age of 202 ± 1 Ma, and are interpreted as the crystallization age of this rock (MSWD = 0.33) (Fig. 6h). Thirteen zircon grains were selected for the analysis of Hf isotopes (Supplementary Data Table S2). Two zircons, corrected to an age of 224 Ma, yield $\epsilon_{\text{Hf}}(t)$ values of -4.8 to -3.0 (Fig. 7). The remaining analyses, corrected to the magmatic crystallization age of 202 Ma, yield $\epsilon_{\text{Hf}}(t)$ values of -6.4 to +1.1 (Fig. 7).

Mineral chemistry and thermobarometry

Representative major element compositions of clinopyroxene, amphibole, plagioclase, biotite and muscovite from the mafic xenoliths and granitoid rocks of the Huayang intrusive complex are shown in Figs 9 and 10 and reported in Supplementary Data Table S4.

Clinopyroxene

Clinopyroxene phenocrysts from mafic xenolith sample 16HY06–5 are characterized by higher MgO

(15.2–16.5 wt %), CaO (24.2–25.0 wt %), and Mg# (84–89), and lower Al_2O_3 (0.29–0.89 wt %) and FeO^{T} (3.49–4.93 wt %), relative to those in mafic xenolith sample 14HY02–5 which have lower MgO (14.2–14.7 wt %), CaO (24.1–24.5 wt %), and Mg# (78–80), and higher Al_2O_3 (0.63–1.07 wt %) and FeO^{T} (6.40–6.83 wt %). Collectively, the clinopyroxenes have mainly diopsidic composition ($\text{Wo}_{49}\text{En}_{40-41}\text{Fs}_{10-11}$ (14HY02–5), $\text{Wo}_{49-50}\text{En}_{43-45}\text{Fs}_{6-8}$ (16HY06–5); Fig. 9a). Crystallization temperatures and pressures of the clinopyroxene phenocrysts were estimated using thermobarometers for hydrous systems from Putirka *et al.* (2003); the errors of the calculated data are less than $\pm 35^\circ\text{C}$ and ± 2 kbar. The results are listed in Supplementary Data Table S4. Overall, the calculated temperatures range from 1224 to 1284°C (average $1251^\circ\text{C} \pm 20$ (standard deviation (std))), and calculated pressures range from 3.4 to 11.0 kbar (average 7.1 kbar ± 2.6 (std)) using the thermobarometers from Putirka *et al.* (2003). This large variation may reflect crystallization during magma ascent or lack of equilibrium required for these calculations. To estimate the original crystallization pressure of the clinopyroxene, we ignored those calculated pressures that were lower than 5 kbar; the remaining data range from 6.4 to 11 kbar (average 8.7 kbar ± 1.5 (std)).

Amphibole

Amphiboles from the mafic xenoliths are all calcic amphibole with high Mg# (65–83), of which sample

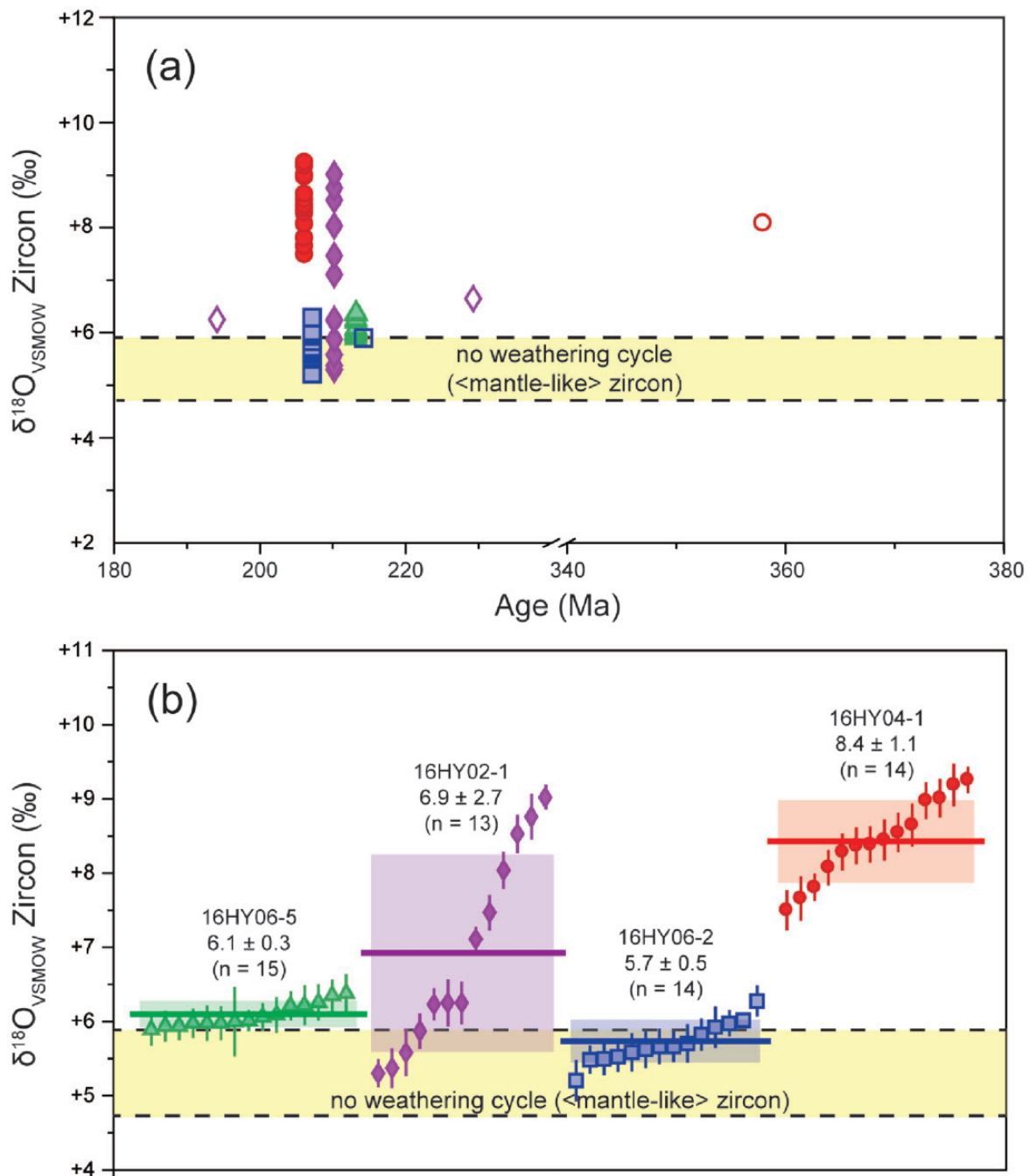


Fig. 8. Zircon O isotopic characteristics of rocks from the Huayang intrusive complex. (a) Plots of zircon $\delta^{18}\text{O}_{\text{VSMOW}}$ values vs crystallization ages for rocks from the Huayang intrusive complex. The $\delta^{18}\text{O}$ for the mantle is from Valley *et al.* (1998). (b) Zircon oxygen isotope composition of rocks from the Huayang intrusive complex. For each sample are displayed the mean and 2 S.D. confidence level. Error bars are the analytical standard errors of each measurement plotted at 2σ . Analytical data are listed in Supplementary Data Table S3.

16HY06-5 has higher Mg# (78–83) than sample 14HY02-5 (65–72), based on the classification of Hawthorne *et al.* (2012) (Supplementary Data Table S4). Specific names of these calcic amphiboles according to this nomenclature show that amphibole phenocrysts from sample 14HY02-5 are paragasite and magnesiohornblende, whereas amphibole phenocrysts from sample 16HY06-5 are magnesiohornblende and actinolite (Supplementary Data Table S4). Crystallization

temperatures and pressures of the amphibole phenocrysts were estimated using the amphibole–plagioclase geothermometer and corresponding geobarometer of Blundy & Holland (1990) and are thought to be accurate within $\pm 40^\circ\text{C}$ and ± 1 kbar. The composition of the plagioclase which is next to the analysed amphibole was used for calculation. The results are listed in Supplementary Data Table S4. The calculated temperatures range from 732 to 812°C (average $770^\circ\text{C} \pm 19$

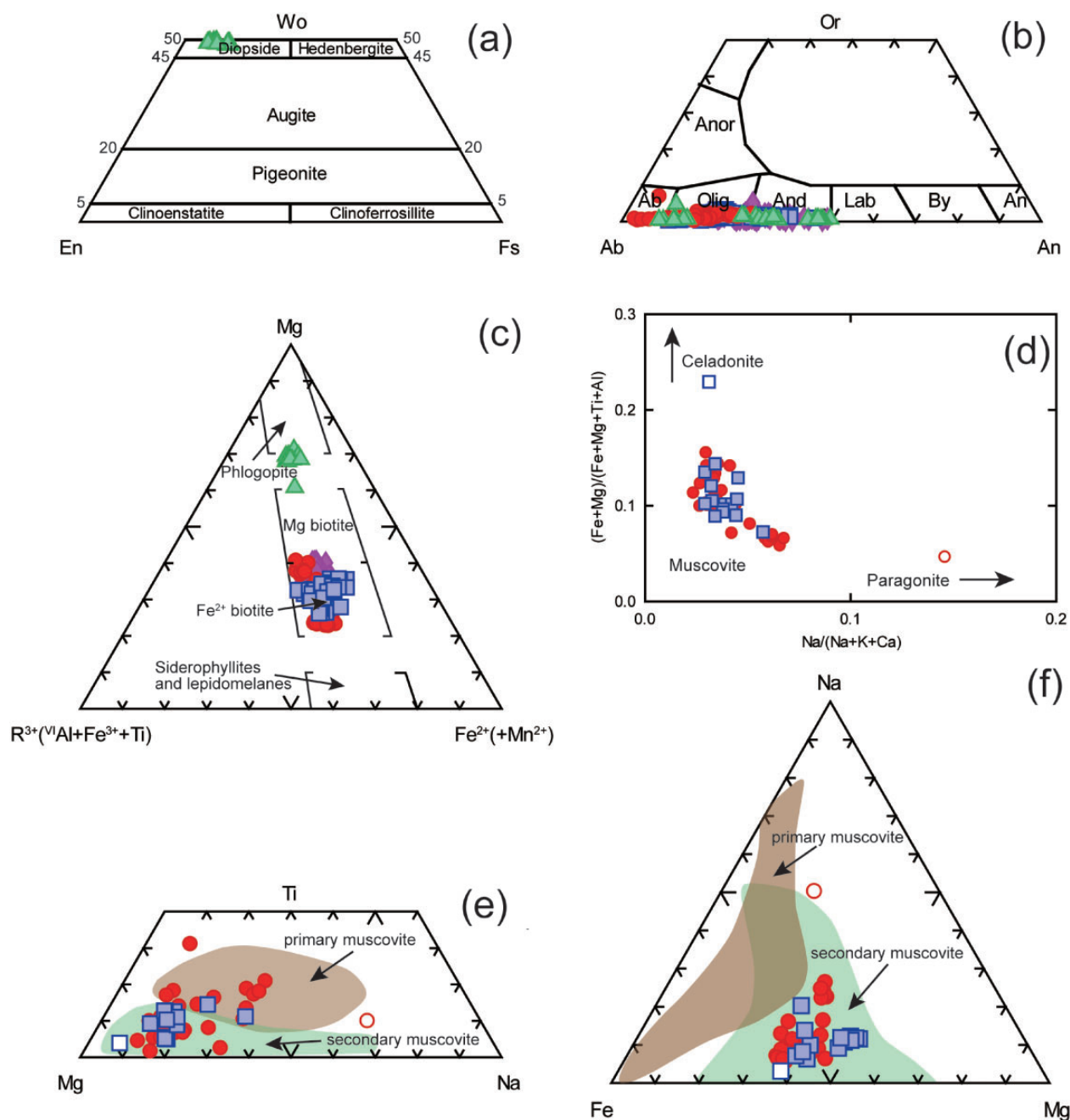


Fig. 9. Mineral composition and classification diagrams for rocks of the Huayang intrusive complex. (a) Clinopyroxenes from the mafic xenoliths plotted on the enstatite–ferrosillite–diopside–hedenbergite quadrilateral of Morimoto (1988). (b) Ab–Or–An diagram for feldspar. Or, potassium feldspar; Anor, anorthoclase; Ab, albite; Olig, oligoclase; And, andesine; Lab, labradorite; By, bytownite; An, anorthite. (c) Classification of biotite according to the nomenclature of Foster (1960). (d) Composition diagram for muscovite after Clarke (1981). (e) and (f) Composition diagram in terms of Ti, Mg and Na (Miller *et al.*, 1981) and Na, Fe and Mg for discrimination between primary and secondary muscovite (Ding *et al.*, 2012). Analytical data are listed in Supplementary Data Table S4. Symbols: mafic xenoliths, green triangles; tonalite and granodiorite, purple diamonds; coarse to medium-grained granite (CMG granite), blue squares; medium to fine-grained granite (MFG granite), red circles.

(std)), and calculated pressures range from 3.8 to 7.7 kbar (average $5.8 \text{ kbar} \pm 1 \text{ (std)}$).

Feldspar

In the mafic xenoliths, plagioclase phenocrysts are mainly andesine ($An = 31\text{--}49$), but some are oligoclase and albite ($An = 9\text{--}29$) (Supplementary Data Table S4).

Plagioclase in the tonalites and granodiorites is generally oligoclase to andesine, showing both normal and reverse compositional zoning (Figs 9b and 10a; $An = 22\text{--}49$; Supplementary Data Table S4). In the CMG granites, plagioclase varies from albite to andesine and also shows normal and reverse compositional zoning (Figs 9b and 10b; $An = 22\text{--}49$; Supplementary Data Table S4).

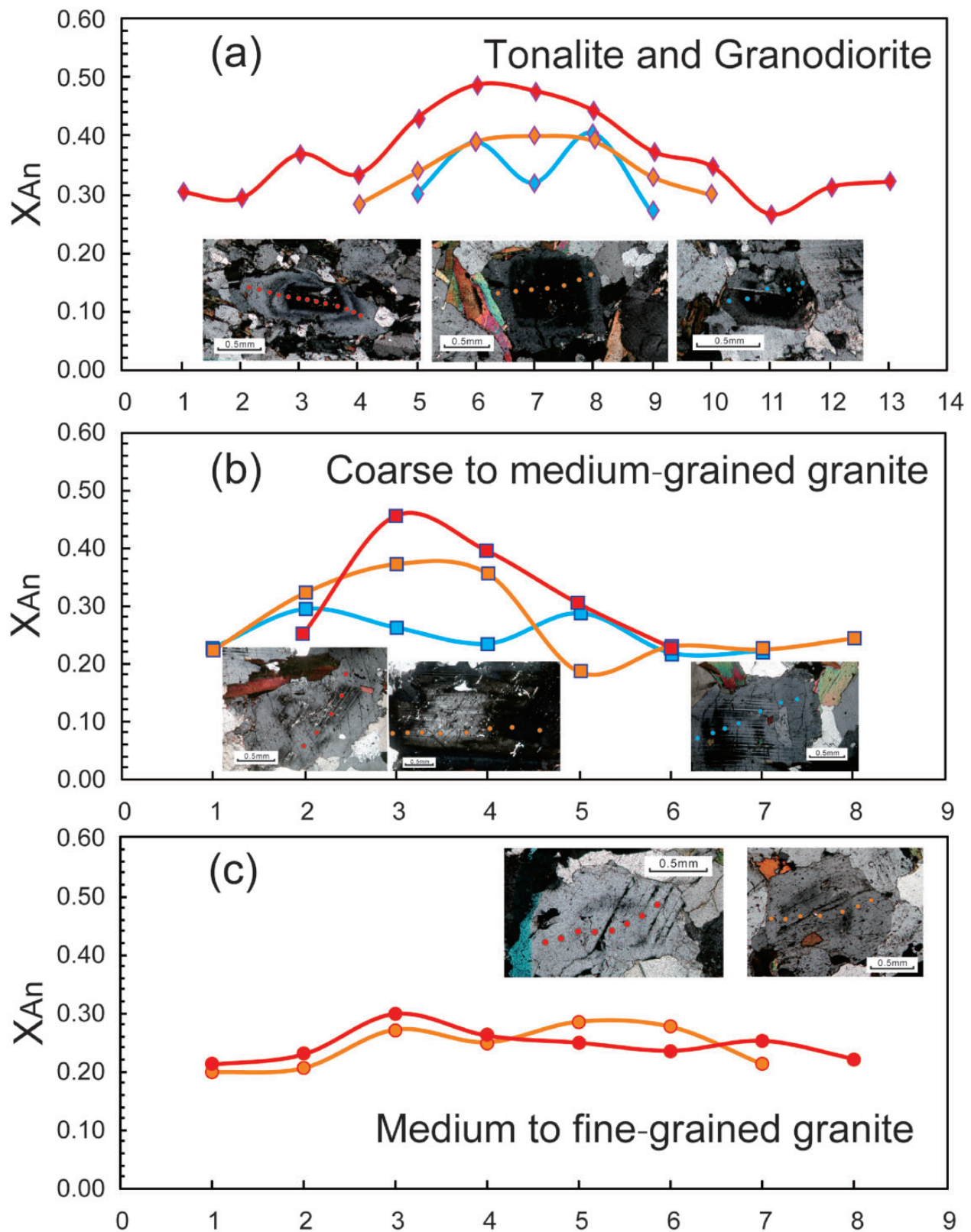


Fig. 10. Compositional zoning in plagioclase from rocks of the Huayang intrusive complex. (a) Tonalites and granodiorites; (b) CMG granites; (c) MFG granites. The different colors correspond to different analysed mineral grains. Analytical data are listed in Supplementary Data Table S4.

However, the plagioclases showing reverse zoning as a whole have low CaO (An) contents (Fig. 10b). Plagioclase in the MFG granites is mainly oligoclase with minor albite, showing compositional variations during crystallization (Figs 9b and 10c; An = 3–30; Supplementary Data Table S4).

Biotite

Biotite in the mafic xenoliths is mainly Mg-biotite (14HY02–5) and Mg-biotite to phlogopite (16HY06–5), exhibiting relatively high concentrations of SiO₂ (37.2–38.6 wt %), MgO (15.7–18.9 wt %) and Mg# (68–77), and low Al₂O₃ (14.1–15.8 wt %), FeO^T (10.0–13.1 wt %) and TiO₂ (1.42–2.23 wt %) (Fig. 9c; Supplementary Data Table S4). In the tonalites and granodiorites, biotite is mainly Fe²⁺-biotite to Mg-biotite with lower SiO₂ (35.1–36.4 wt %), MgO (7.65–9.98 wt %) and Mg# (39–47), and higher Al₂O₃ (15.0–17.5 wt %), FeO^T (19.5–21.4 wt %) and TiO₂ (2.51–4.43 wt %) relative to that in the mafic xenoliths (Fig. 9c; Supplementary Data Table S4). Biotites in the CMG granites are all Fe²⁺-biotite with low MgO (6.24–8.80 wt %) and Mg# (33–42), and high Al₂O₃ (15.2–18.1 wt %) and FeO^T (20.5–24.2 wt %) (Fig. 9c; Supplementary Data Table S4). In the MFG granites, biotites are also generally Fe²⁺-biotite with lower MgO (5.37–8.08 wt %) and Mg# (29–40), and high Al₂O₃ (14.9–18.7 wt %) and FeO^T (21.4–24.6 wt %) (Fig. 9c; Supplementary Data Table S4). However, one MFG granite sample (16HY08–1) exhibits higher MgO (8.52–10.1 wt %) and Mg# (42–49) (Fig. 9c; Supplementary Data Table S4). Overall, the Al₂O₃ and FeO^T concentrations of biotite increase and MgO content decrease along with the increase of the SiO₂ content of the whole-rock samples. Biotites with high Al₂O₃ values usually coexist with muscovite, suggesting high alumina contents in the parental magma.

The crystallization temperature and pressure of biotite in granitic magma can be estimated using the empirical geothermometer of Henry *et al.* (2005) (error less than ± 30°C), and Al-in-biotite geobarometer of Uchida *et al.* (2007) (error less than ± 1 kbar). The results are listed in Supplementary Data Table S4. The calculated temperature for tonalites and granodiorites ranges from 652 to 736°C (average 701°C ± 26 (std)), and calculated pressure ranges from 1.7 to 3.1 kbar (average 2.5 kbar ± 0.4 (std)). The temperature for CMG granites is 648 to 718°C (average 695°C ± 17 (std)), corresponding to pressures between 2.0 to 3.8 kbar (average 2.8 kbar ± 0.5 (std)). The MFG granites give crystallization temperatures ranging from 657 to 752°C (average 698°C ± 20 (std)), and pressures between 1.7 and 4.0 kbar (average 2.9 kbar ± 0.7 (std)).

Muscovite

We only analysed muscovite in the CMG and MFG granites to identify whether they are primary muscovite or secondary muscovite (Supplementary Data Table S4). On the whole, all analysed minerals are muscovites, except for two which have paragonitic or celadonic

components (Fig. 9d). The muscovites have generally low TiO₂ (0.06–0.80 wt %; except for one that has 1.56 wt %) and Na₂O (0.17–0.50 wt %) contents, and high MgO (0.83–2.75 wt %) concentrations. Some of the muscovites analysed in this study plot in the primary muscovite field in the Ti–Mg–Na diagram, whereas all muscovites plot in the secondary muscovite field in the Na–Fe–Mg diagram (Fig. 9e and f). Combined with their petrographic characteristics, we consider that these muscovites are mainly of metasomatic origin formed by replacement of early crystallized biotite, or hydrothermal muscovite formed from late or post-magmatic hydrothermal fluids (Zhang *et al.*, 2010; Ding *et al.*, 2012). Therefore, they cannot reflect the physico-chemical conditions during magma crystallization, and are not suitable for indicating the composition and formation environment of the parental magmas (Miller *et al.*, 1981; Zhang *et al.*, 2010; Ding *et al.*, 2012).

Whole-rock geochemistry

The major and trace element compositions of the mafic xenoliths and granitoid rocks from the Huayang intrusive complex are given in Supplementary Data Table S5.

Mafic xenoliths

The mafic xenoliths have low SiO₂ (46.9–49.9 wt %), and plot in the sub-alkaline gabbro field in a SiO₂ vs (Na₂O + K₂O) diagram (Fig. 11a). In a SiO₂ vs K₂O diagram, they plot on the boundary between medium-K and high-K calc-alkaline rock series (Fig. 11b). These samples have high MgO (11.3–12.6 wt %), Mg# (68–73), CaO (12.6–12.9 wt %), TiO₂ (0.79–1.22 wt %), Cr (491–1768 ppm) and Sc (152–260 ppm) contents, and low P₂O₅ (0.08–0.12 wt %) and Rb/Sr (0.06–0.29) ratios (Fig. 11). Chondrite-normalized REE patterns are slightly fractionated with low (La/Yb)_N, (La/Sm)_N, and (Gd/Yb)_N of 5.32–6.02, 1.96–2.01 and 1.92–2.20, respectively, and show weak negative Eu anomalies (δEu = 0.89–0.9) (δEu = Eu_N/SQRT(Sm_N*Gd_N); subscript N represents the chondrite-normalized value; Sun & McDonough, 1989), Fig. 12a. These samples have low concentrations of large ion lithophile elements (LILE), such as Rb, Ba and Th, and show negative Nb–Ta anomalies and moderately negative P anomalies in primitive mantle-normalized multi-element patterns (Fig. 12b). The trace element patterns of the mafic xenoliths are similar to those of the average lower continental crust, except for slightly higher light rare earth elements (LREE) (Fig. 12b; Rudnick & Gao, 2003). Their major and trace element characteristics are roughly the same as those of mafic magmatic enclaves (MME) and mafic dykes in the SQB (Figs 11 and 12).

Tonalites and granodiorites

The tonalites and granodiorites have intermediate SiO₂ (61.3–69.0 wt %), and plot in the monzonite and quartz monzonite fields in the SiO₂ vs (Na₂O + K₂O) diagram (Fig. 11a). They are high-K calc-alkaline rocks according

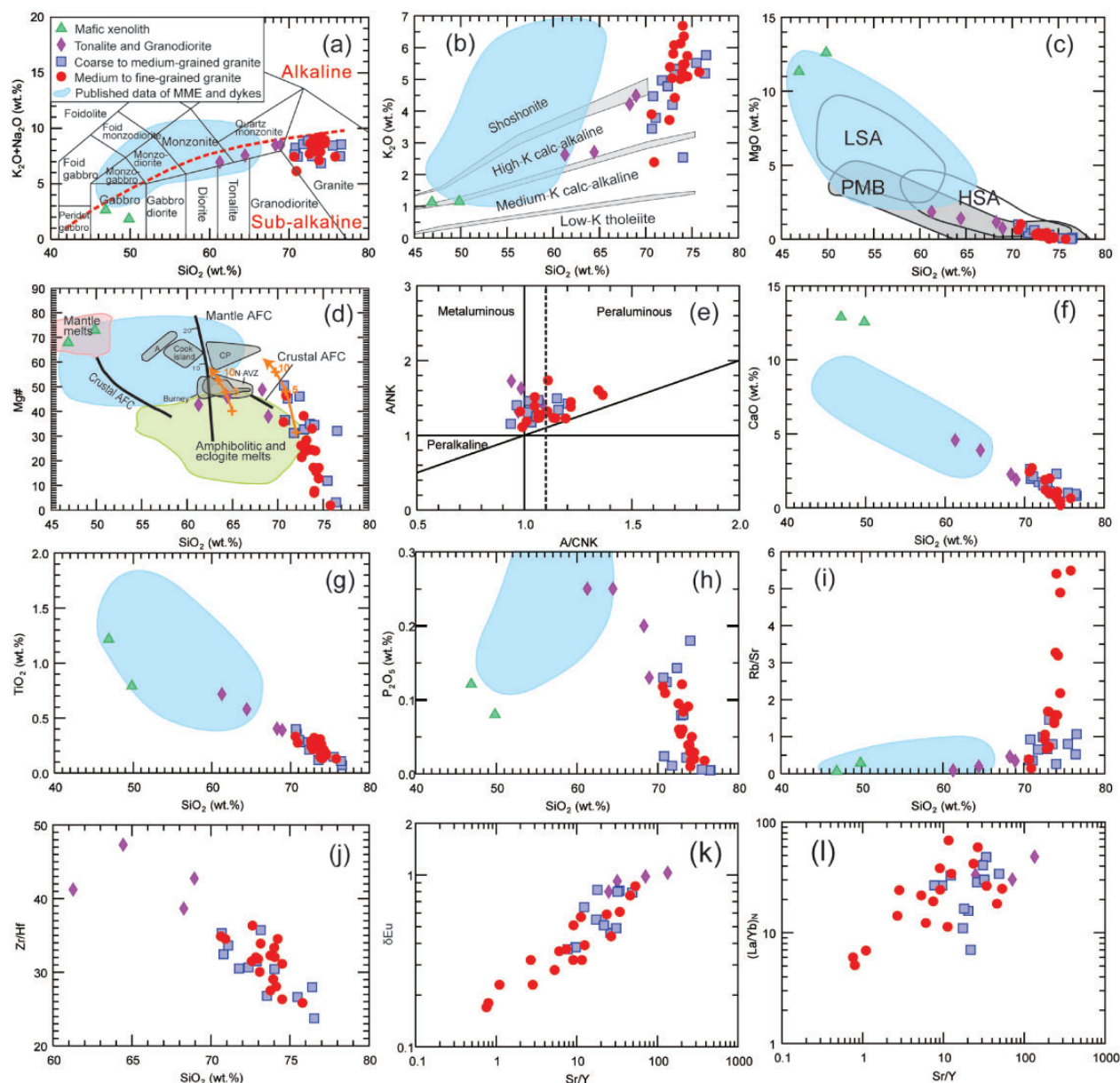


Fig. 11. Petrochemical classification of samples from the Huayang intrusive complex and their geochemical characteristics. (a) Total alkalis vs silica diagram (TAS, after Middlemost, 1994). (b) K_2O vs SiO_2 classification diagram (after Rollinson, 1993). (c) MgO vs SiO_2 diagram (after Martin *et al.*, 2005). (d) $Mg\#$ vs SiO_2 diagram (modified after Stern & Killian, 1996). This also shows the field for pure crustal partial melts obtained in experimental studies by dehydration melting of amphibolitic rocks and eclogites (Rapp & Watson, 1995; Rapp *et al.*, 1999; Smithies, 2000; Sisson *et al.*, 2005). The mixing trends illustrate between mafic magma (16HY06–5) and granitoid magmas, starting with the sample 14HY09–5, and experimental data from Qian & Hermann (2013). (e) A/NK (molar $Al_2O_3/(Na_2O + K_2O)$) vs A/CNK (molar $Al_2O_3/(CaO + Na_2O + K_2O)$) (after Maniar & Piccoli, 1989). (f)–(j) Covariation of selected whole-rock major oxides, trace elements and trace element ratios vs SiO_2 . (k) and (l) Covariation of δEu and $(La/Yb)_N$ vs Sr/Y . The published data for MME and dykes are from Wang *et al.* (2007b, 2011), Qin *et al.* (2009, 2010, 2013), Jiang *et al.* (2012), and Hu *et al.* (2016a, 2017b). Abbreviations: LSA, low- SiO_2 adakites; HAS, high- SiO_2 adakites; PMB, melts obtained by experimental melting of basalts or amphibolites. Legends as in Fig. 9.

to the SiO_2 vs K_2O classification (Fig. 11b). These samples have moderate MgO (0.74–1.85 wt %), $Mg\#$ (38–49), CaO (1.91–4.58 wt %), TiO_2 (0.39–0.72 wt %) and high P_2O_5 (0.13–0.25 wt %) contents, with metaluminous to weakly peraluminous characteristics ($A/CNK=0.94$ – 1.09) (Fig. 11). They are characterized by steep chondrite-normalized REE patterns with high $(La/Yb)_N$, $(La/Sm)_N$, and $(Gd/Yb)_N$ ratios of 30.26–48.62, 4.72–7.25

and 3.71–4.63, respectively, with no or weak negative Eu anomalies ($\delta Eu = 0.80$ – 1.03) (Fig. 12c). They display moderate to high Sr/Y (24.91–134.04) and Zr/Hf (38.65–47.32), and low Rb/Sr (0.09–0.46) (Fig. 11). These samples are enriched in LILE (Rb, Ba, Th, and U), and show distinctly negative Nb–Ta anomalies and negative P anomalies in primitive mantle-normalized multi-element patterns. Compared to the upper continental crust,

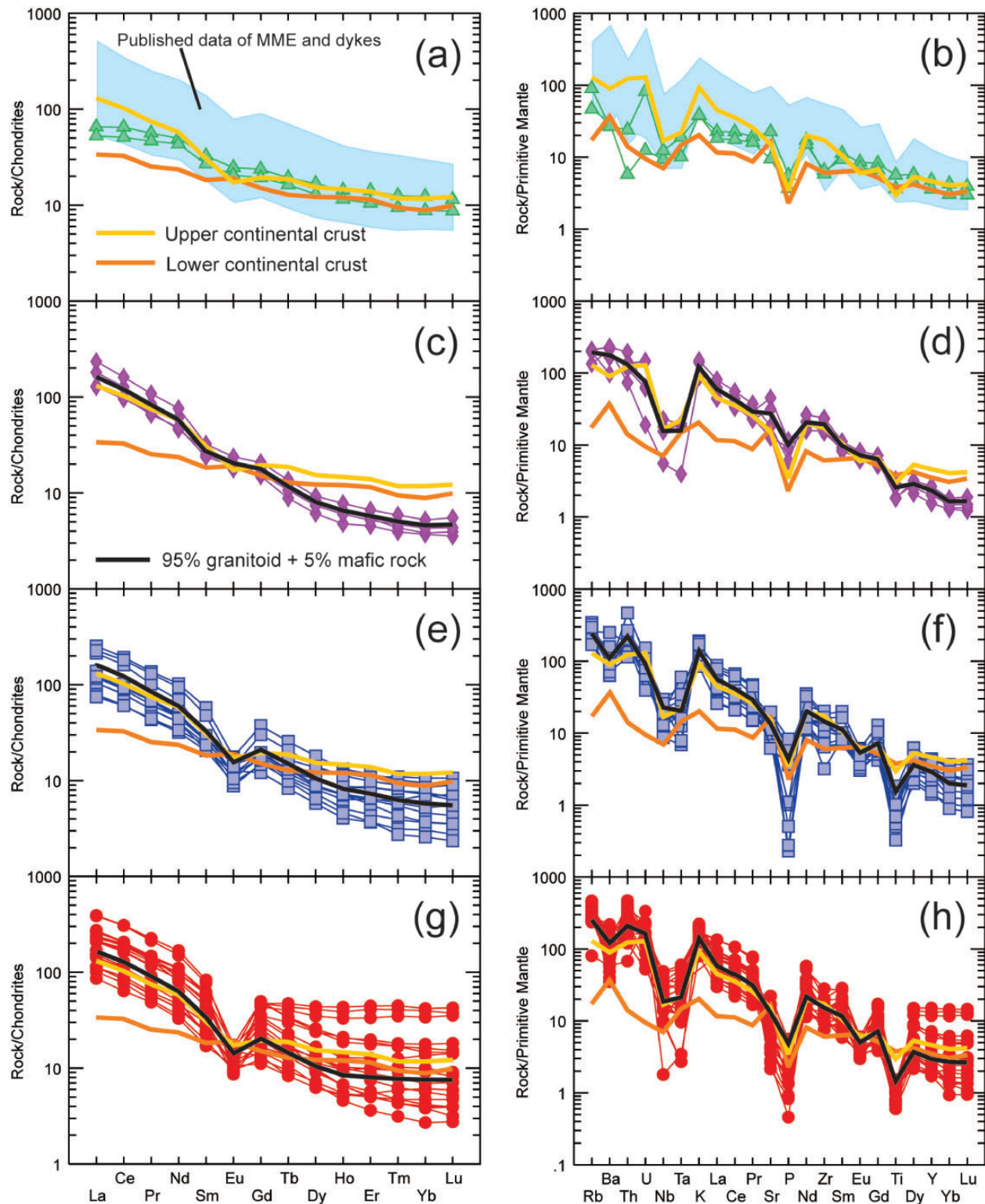


Fig. 12. Chondrite-normalized REE patterns and primitive mantle-normalized multi-element patterns for samples from (a) and (b) mafic xenoliths; (c) and (d) tonalites and granodiorites; (e) and (f) CMG granites; (g) and (h) MFG granites. Normalization values are from Sun & McDonough (1989). The upper continental crust and lower continental crust data are from Rudnick & Gao (2003). The data for MME and dykes are from Wang *et al.* (2007b, 2011), Qin *et al.* (2009, 2010, 2013), Jiang *et al.* (2012), and Hu *et al.* (2016a, 2017b). The mixing lines between granitoid and mafic rock represent 95% average concentration of the granitoids ($\text{SiO}_2 < 73 \text{ wt } \%$) and 5% average concentration of the mafic xenoliths and MME. Symbols as in Fig. 9.

they share similar LILE and LREE concentrations, but exhibit lower contents of heavy rare earth elements (HREE) (Fig. 12d; Rudnick & Gao, 2003).

CMG granites and MFG granites

The CMG granites and MFG granites have high SiO₂ (70.6–76.5 wt %), and plot in the granite field (Fig. 11a), and belong to metaluminous to strongly peraluminous rock series (A/CNK=0.94–1.36) (Fig. 11e). They are mainly high-K calc-alkaline series to shoshonitic series according to the SiO₂ vs K₂O diagram (Fig. 11b). These samples have lower MgO (0.01–1.02 wt %), Mg# (2–51), CaO (0.18–2.70 wt %), P₂O₅ (0.01–0.18 wt %), Zr/Hf (23.73–36.33) and Sr/Y (0.76–53.25), and higher Rb/Sr (0.14–5.49) relative to tonalites and granodiorites (Fig. 11). The main differences between CMG granites and MFG granites are the higher Rb/Sr (average 2.09) and lower Sr/Y (average 14.67) ratios of the MFG granites in comparison to the CMG granites (0.74 and 23.24, respectively) (Fig. 11i and k). Both are characterized by steep to smooth chondrite-normalized REE patterns with high (La/Yb)_N, (La/Sm)_N, and (Gd/Yb)_N ratios of 5.09–68.25, 3.17–7.21 and 1.13–7.09, respectively, with weak to strong negative Eu anomalies ($\delta\text{Eu} = 0.17\text{--}0.86$) (Fig. 12e and g). Relative to CMG granites, some MFG granite samples exhibit higher HREE and more negative Eu anomalies (Fig. 12e and g). In primitive mantle-normalized multi-element diagrams, these samples are enriched in LILE (Rb, Ba, Th, and U), and show distinct negative Nb–Ta, P and Ti anomalies (Fig. 12f and h). Overall, they have similar trace element concentrations to those of the upper continental crust, but some samples exhibit lower heavy rare earth elements (HREE) and more negative Eu, P and Ti anomalies (Fig. 12f and h; Rudnick & Gao, 2003).

DISCUSSION

Age of the Huayang intrusive complex

Zircon crystals extracted from mafic xenoliths in the Huayang intrusive complex show a single U–Pb age population and lack inherited zircons (Fig. 6a and b), indicating that the mafic xenoliths in the Huayang intrusive complex were formed from ~218–213 Ma, coeval with most MME and mafic dykes in the SQB (Qin *et al.*, 2010; Wang *et al.*, 2011; Jiang *et al.*, 2012; Yang *et al.*, 2012; Hu *et al.*, 2016b, 2017b). The zircon U–Pb ages of the tonalites and granodiorites suggest their emplacement from 210–207 Ma (Fig. 6c and d), consistent with previous studies (Liu *et al.*, 2011b). The tonalites and granodiorites were emplaced slightly later than the crystallization of the mafic xenoliths. Our new zircon chronological data reveal that the CMG granites (~207–204 Ma) were formed concurrently with the MFG granites (~206–202 Ma) (Fig. 6). The narrow range of ages indicates that the CMG and MFG granites, which are the most volumetrically significant magmatic event in the

Huayang intrusive complex, were emplaced in a relatively short time period (a few Myr).

Inherited zircons (based on U–Pb ages) were identified in the CMG, MFG, tonalites and granodiorites. Prominent age populations include: ~743 Ma, ~426 Ma, ~358 Ma, ~229–213 Ma (Fig. 6). The ~743 Ma age from the inherited populations is thought to be related to Neoproterozoic magmatism in the SQB (e.g. Hu *et al.*, 2016a; Dong *et al.*, 2017). Zircons with ages of ~426 Ma and ~358 Ma may be captured from Paleozoic crustal materials during magma transfer and emplacement (Qin *et al.*, 2010; Deng *et al.*, 2016). The ~229–213 Ma zircon age population is consistent with widespread Norian magmatism in the SQB (Li *et al.*, 2015; Wang *et al.*, 2015). All of the older ages are considered to be either inherited from the source region or assimilated from wall-rocks.

Constraints on the timing of initial collision and extension

The compositional similarity between subduction-related magmas and collision-related magmas leads to difficulty in distinguishing between these two processes based solely on geochemistry. In this study, we use independent geological evidence and magmatism in the SQB to constrain the timing of initial collision and extension.

The collision between the NCC and SCB was scissor-like with clockwise rotation of the SCB based on paleomagnetic evidence (Zhao & Coe, 1987). According to paleomagnetism studies, the initial collision took place at the Dabie Orogen during the Late Permian to Early Triassic (Zhu *et al.*, 1998). This is also confirmed by the *P–T–t* paths of eclogites in the Dabie Orogen (Zhang *et al.*, 2009). With regard to QOB, some authors have suggested that the collision started during the Late Triassic (<220 Ma) (Jiang *et al.*, 2010; Dong & Santosh, 2016; Lu *et al.*, 2016); whereas others have proposed that the initial collision occurred during the Middle to Late Triassic (~225–240 Ma) (Qin *et al.*, 2013; Wang *et al.*, 2015). A third hypothesis postulates that the collision started after the Triassic (<200 Ma) (Li *et al.*, 2015).

The depositional history of foreland basins along the northern margin of the YZC provides valuable information about the continental collision. During the Early to Middle Triassic, marine flysch deposition characterized these foreland basins (Liu *et al.*, 2005). However, non-marine molasse began to be deposited in the foreland basins during the Norian, indicating that the closure of the Mianlue Ocean should have started before the Norian (~227 Ma) (Liu *et al.*, 2005). Metamorphic ages of metabasites (⁴⁰Ar/³⁹Ar ages of ~227 Ma to 219 Ma) in the ophiolite mélangé of the Mianlue zone also suggest that the initial collision began before ~227 Ma (Li *et al.*, 1999; Chen *et al.*, 2010). The emplacement ages of stitching plutons (e.g. the Guangtoushan pluton) are ~224–218 Ma, which suggests the closure of the Mianlue Ocean occurred before ~224 Ma (Deng *et al.*,

2016). In addition, paleomagnetism data suggest that the collision between the NCC and SCB was completed before the end of the Triassic (~200 Ma) (Zhu *et al.*, 1998). Therefore, the initial collision between the NCC and SCB must have taken place prior to ~230 Ma (probably during the Middle to Late Triassic).

The extensional history in the SQB is more complicated because an intracontinental collision event during the Jurassic to Cretaceous was followed by the collision of the NCC and SCB (Dong & Santosh, 2016). Triassic structures were reactivated by Jurassic–Cretaceous structures in the SQB (Liu *et al.*, 2015). The SQB experienced widespread and prominent extension-related tectonic collapse during the Cretaceous to Cenozoic forming today's landform and crustal structure (Hu *et al.*, 2006; Liu *et al.*, 2015). However, some evidence still exists to track regional post-collisional extension during the Triassic. The Anzishan quasi-high pressure granulite in the Mianlue zone yields retrograde metamorphic ages of ~199 Ma, which is considered to be the time of exhumation and extension during the post-collision period (Zhang *et al.*, 2002). In addition, the rapid uplift and exhumation of granitoid intrusions from ~210 to 180 Ma in the SQB is supported by their cooling history (Wang *et al.*, 2007a, 2014). A recent study of the crustal thickness in the SQB based on geochemical indices (Sr/Y and La/Yb) suggested that crustal thinning in the SQB started at ~210 Ma (Hu *et al.*, 2017a). Consequently, we propose that the SQB experienced regional extension, which could be regarded as an indicator of a post-collisional tectonic setting, from ~210 to 180 Ma. Therefore, the Huayang intrusive complex comprises magmatic rocks formed during the syn-collisional to post-collisional stages of the orogen's evolution.

Petrogenesis

Mafic xenoliths

The chemical compositions of the SQB mafic xenoliths indicate that they were either formed by partial melting of a mantle source (Patiño Douce, 1999; Clements & Stevens, 2012), or are restites of partially melted continental crust (Chappell *et al.*, 1987; Chappell & White, 2001). Because there are no old inherited ages in the zircons analysed from these mafic xenoliths, we interpret their parental magma to have been generated in the upper mantle.

Mafic xenoliths are relatively rare in the SQB. They have similar whole-rock geochemical compositions to the MME and lamprophyre dykes in the SQB (Figs 11 and 12; Qin *et al.*, 2010; Hu *et al.*, 2016b, 2017b). The mafic xenoliths have relatively high Rb/Sr (0.06–0.29) and low Ba/Rb (3.27–7.15) which is comparable to the MME with Rb/Sr of 0.12–0.30 and Ba/Rb of 5.29–12.89 (Hu *et al.*, 2017b). Previous studies have suggested that melts in equilibrium with phlogopite should have high K₂O, Rb/Sr (>0.1) and low Ba/Rb (<20) (Furman & Graham, 1999). As a result, the MME and mafic dykes in the SQB have been proposed to be derived from partial

melting of phlogopite-bearing metasomatized lithospheric mantle (Wang *et al.*, 2007b; Qin *et al.*, 2010; Hu *et al.*, 2016b, 2017b). Such a model, could be also suitable for explaining mafic xenoliths with medium to high-K compositions (Foley *et al.*, 1992; Yang *et al.*, 2004).

The mafic xenoliths have zircon εHf(t) values (-6.8 to +4.1) within the range of the MME in the SQB (-10.2 to +6.1), which also supports a lithospheric mantle source (Qin *et al.*, 2010; Wang *et al.*, 2011; Jiang *et al.*, 2012; Hu *et al.*, 2016b, 2017b). There are no comparable zircon δ¹⁸O isotope data available for MME or mafic dykes in the SQB, but the zircon δ¹⁸O isotope composition of the SQB mafic xenoliths show slightly higher values (average 6.1‰) than typical asthenosphere-derived magmas (average 5.3‰; Valley *et al.*, 1994) (Fig. 8). The zircon δ¹⁸O values are within the range of magmas derived from sub-continental lithospheric mantle (Fig. 8; Valley *et al.*, 1994). Collectively, we propose that the parental magmas of the mafic xenoliths were generated by partial melting of a phlogopite-bearing sub-continental lithospheric mantle source.

Tonalites and granodiorites

Several petrogenetic models have been proposed for the formation of granitoid rocks, including: (1) vapour-present/vapour-absent dehydration melting of crustal materials (Inger & Harris, 1993; Patiño Douce, 1999; Weinberg & Hasalová, 2015); (2) magma mixing between mantle-derived melts and crust-derived melts (Bonin, 2004; Barbarin, 2005), and (3) differentiation of basaltic to dioritic magmas (Wu *et al.*, 2003; Castillo, 2012). The chemical composition of the SQB tonalites and granodiorites are similar to those of I-type granites (Fig. 11; Chappell & White, 2001). The plagioclases in the tonalites and granodiorites show reverse zoning, which may indicate input and assimilation of mafic magmas (Fig. 10a). MgO and Mg# in the tonalites and granodiorites plot mainly in the range of partial melts of basaltic rocks (Fig. 11c and d), suggesting that the granitoid magma are chiefly derived from a crustal source with minor (less than 5%) mafic magma input. Our calculations suggest that minor input of mafic magma will not significantly change the trace element concentrations (Fig. 12c and d). The high Sr/Y and Zr/Hf ratios, high P₂O₅ contents, low Rb/Sr and δEu values close to 1.0, suggest that fractional crystallization of feldspar, zircon and apatite was not significant (Figs 11 and 12).

According to the Rb/Sr vs Ba diagram (Fig. 13a), these rocks either are derived from vapour-present, muscovite-dehydration melting or experienced low degrees of plagioclase and/or biotite fractionation. Experiments show that fluid-saturated muscovite melting will lead to a considerable decrease in Ba and increase in Sr, with little change in Rb/Sr (Inger & Harris, 1993; Weinberg & Hasalová, 2015). The tonalites and granodiorites display a coupled decrease in both Ba and Sr, with little change in Rb/Sr (Fig. 13a and b).

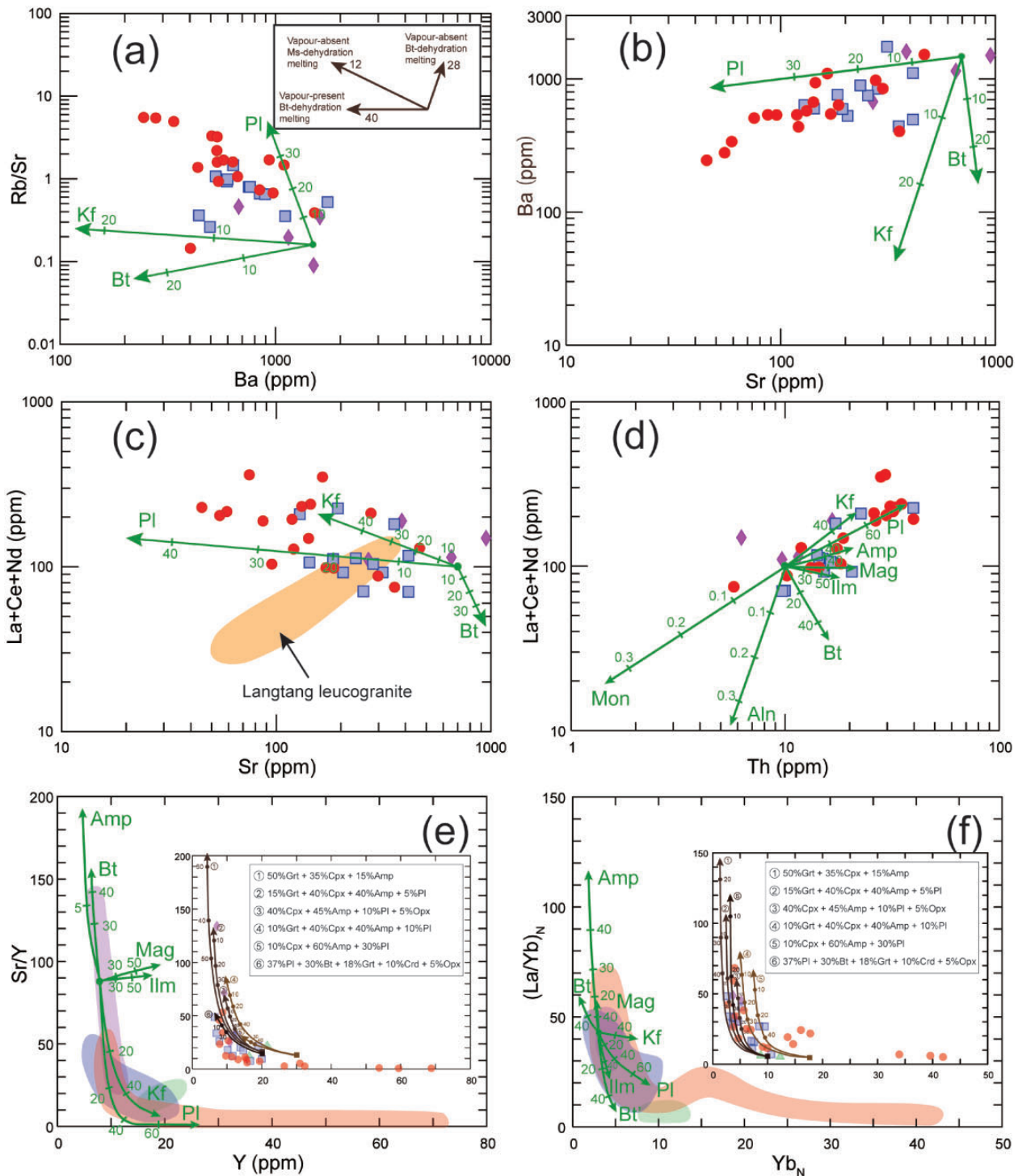


Fig. 13. Petrogenetic discrimination diagrams for rocks from the Huayang intrusive complex. (a) Rb/Sr vs Ba (ppm). Inset shows a partial melting trend after Inger & Harris (1993). (b) Ba (ppm) vs Sr (ppm). (c) and (d) La + Ce + Nd (ppm) vs Sr and Th (ppm). The Langtang leucogranites are from Inger & Harris (1993). (e) Sr/Y vs Y (ppm). (f) (La/Yb)_N vs Yb_N. The green curves represent modeled fractional crystallization trends for different minerals. The brown curves in the insets of (e) and (f) represent modeled batch partial melting trends with different starting materials and residual mineral assemblages. The numbers on the fractional crystallization curves are fractions of crystallized minerals and numbers on the melting curves are melting fractions. The detailed parameters used in the modeling are listed in Table 2. Legends as in Fig. 9.

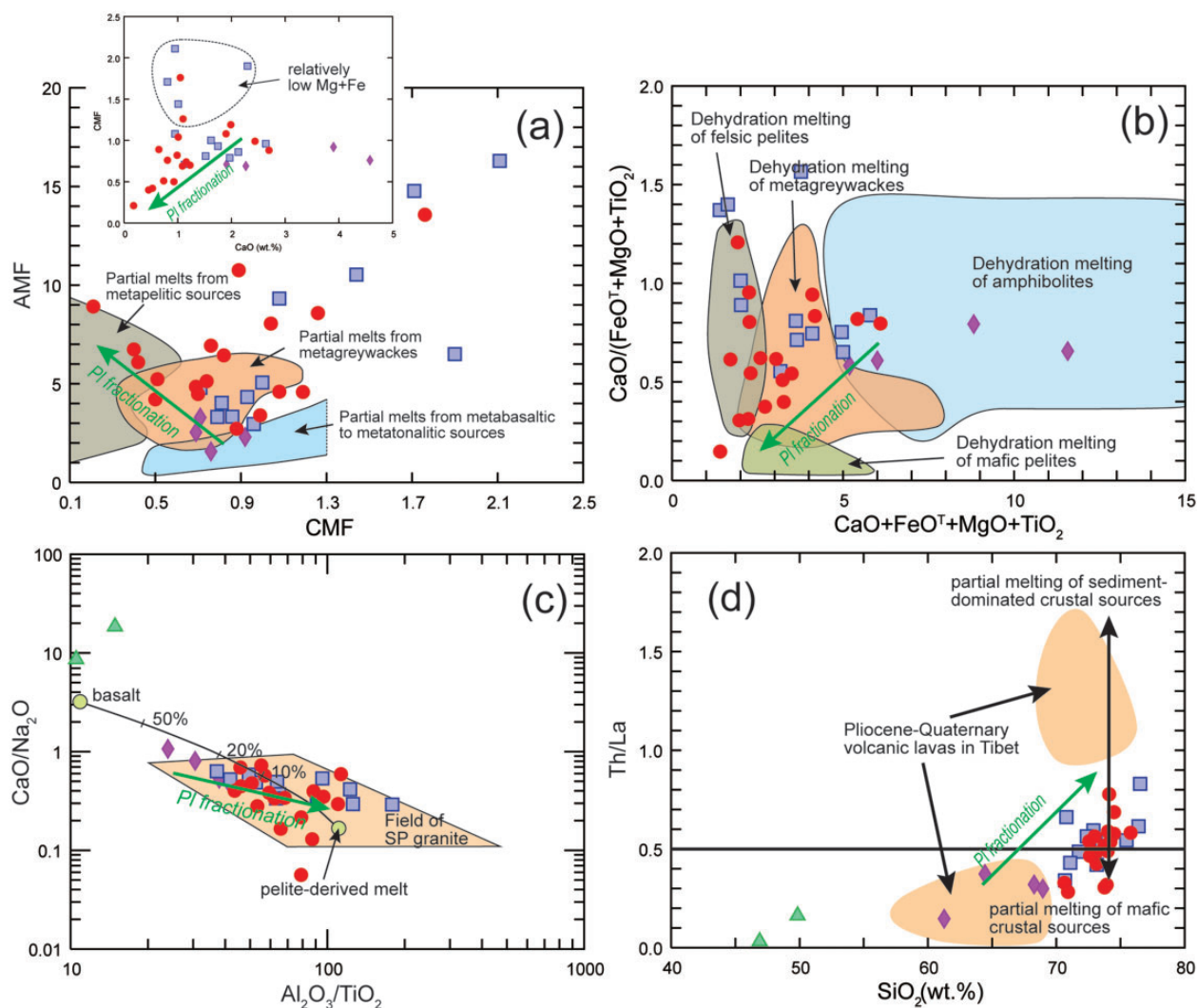


Fig. 14. Source discrimination diagrams for granitoid rocks from the Huayang intrusive complex. (a) Molar $\text{Al}_2\text{O}_3/(\text{MgO} + \text{FeO}^{\text{T}})$ (AMF) vs $\text{CaO}/(\text{MgO} + \text{FeO}^{\text{T}})$ (CMF) showing the source composition for the granitoid rocks from the Huayang intrusive complex, modified after Altherr *et al.* (2000). Inset is CMF vs CaO (wt %) diagram (b) $\text{CaO}/(\text{FeO}^{\text{T}} + \text{MgO} + \text{TiO}_2)$ vs $\text{CaO} + \text{FeO}^{\text{T}} + \text{MgO} + \text{TiO}_2$, modified after Patiño Douce (1999). (c) $\text{CaO}/\text{Na}_2\text{O}$ vs $\text{Al}_2\text{O}_3/\text{TiO}_2$, after Sylvester (1998). (d) Th/La vs SiO_2 , after Wang *et al.* (2016). Symbols as in Fig. 9.

Therefore, the tonalites and granodiorite are not the products of vapour-present muscovite-dehydration melting.

We used a batch partial melting model to explore possible melt sources and residual mineral assemblages for the granitoids of the Huayang intrusive complex. The chemical compositions of the starting materials are based on the composition of the mafic xenoliths in the complex, Neoproterozoic gabbroic rocks and tonalitic rocks in the SQB and metagreywackes (Otamendi & Patiño Douce, 2001; Kamei *et al.*, 2009; Hu *et al.*, 2016a). According to our geochemical modeling, their high Sr/Y (up to 134.04) and $(\text{La}/\text{Yb})_{\text{N}}$ (up to 48.62) ratios are most likely to be caused by variable degrees of partial melting of basaltic rocks, leaving clinopyroxene, amphibole and, or, garnet as major residual minerals, along with minor plagioclase (Fig. 13e and f). Experiments have demonstrated that granitoid

rocks with such high Sr/Y and La/Yb could be formed by partial melting of mafic crust at ~ 10 – 13 kbar, corresponding to ~ 35 – 45 km depth for typical continental crust (Qian & Hermann, 2013). The relatively low Sr/Y and $(\text{La}/\text{Yb})_{\text{N}}$ of the granodiorites is most likely the result of 10–20% plagioclase fractionation (Fig. 13). In source discrimination diagrams, tonalites plot mainly in the field of melts derived from partial melting of metabasaltic rocks and amphibolites (Fig. 14a and b), whereas the granodiorites plot close to the boundary between metabasaltic-derived melts and metagreywacke-derived melts (Fig. 14a–c). This phenomenon could result from the fractionation of plagioclase. The low Th/La ratio (< 0.5) indicates that the melt source is primarily basaltic rocks (Fig. 14d).

The zircon Hf isotope compositions of tonalites and granodiorites plot near CHUR (chondritic uniform reservoir) and are within the evolution range of Neoproterozoic

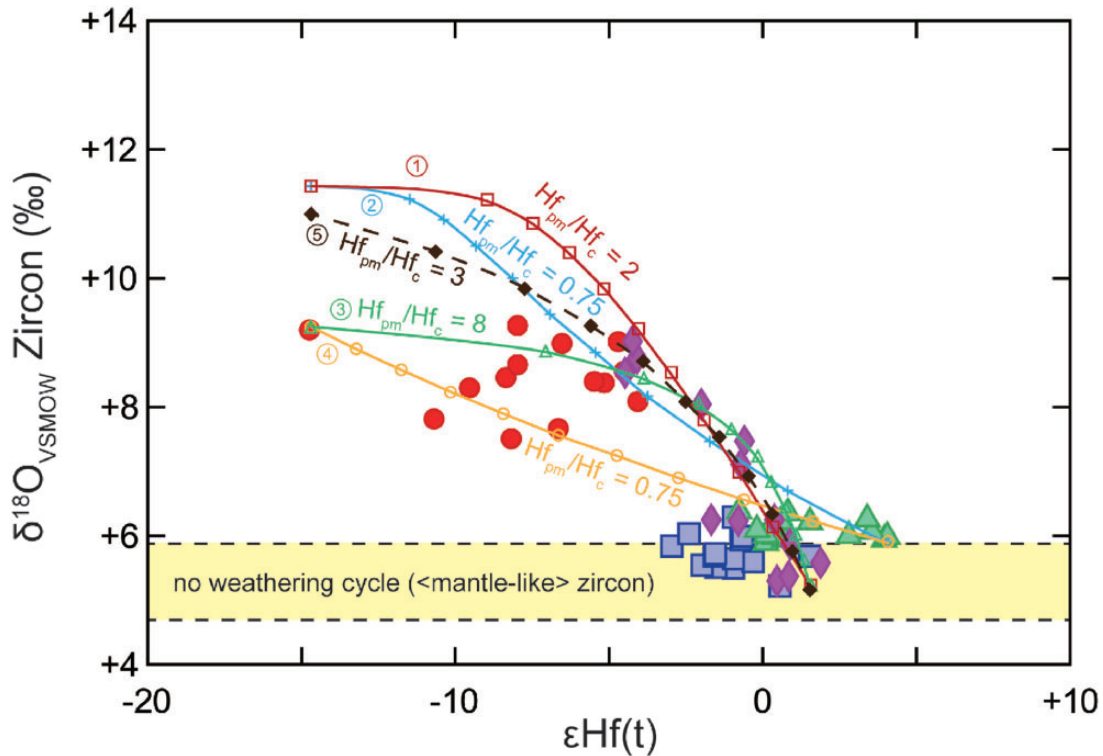


Fig. 15. Variation of $\delta^{18}\text{O}$ versus $\epsilon\text{Hf}(t)$ for zircons of this study, showing calculated curves corresponding to magma evolution by simple mixing and crustal assimilation-fractional crystallization (AFC). The $\delta^{18}\text{O}$ for the mantle is from Valley *et al.* (1998). Ticks on the curves represent 10% increments, and the ratio of Hf concentrations in the parental magma (pm) and crustal (c) end-members ($\text{Hf}_{\text{pm}}/\text{Hf}_{\text{c}}$) is indicated for each. The detailed parameters used in the modeling are listed in Table 3. Symbols as in Fig. 9.

basement rocks in the SQB. The rocks analysed in this study are similar to other granitoid intrusions in the SQB, except for one analysis on a zircon with an inherited age, which shows very low $\epsilon\text{Hf}(t)$ values (-37.3) (Fig. 7). Although, zircon Hf isotope compositions are generally constant for the tonalites and granodiorites, the zircon $\delta^{18}\text{O}$ values display quite large variations from 5.3‰ to 9.0‰ (Fig. 8). This result indicates that at least two source materials with different O isotope compositions participated in the formation of the tonalites and granodiorites. We modeled zircon Hf and O isotopic mixing to determine the potential isotopic components (Fig. 15). The zircon Hf–O isotopic data for mafic xenoliths, CMG and MFG granites were selected as three potential source materials. Although Lu *et al.* (2016) reported a zircon $\delta^{18}\text{O}$ value of $\sim 11\%$ for the Huayang granite, the corresponding high zircon $\epsilon\text{Hf}(t)$ (-5.4 to -2.0) values are not suitable for being an end-member to the samples analysed in this study. Our modeling suggests that melts equivalent to the mafic xenoliths are not a potential source because the calculated simple mixing and AFC (assimilation and fractional crystallization) lines cannot fit the range of tonalite and granodiorite isotopic compositions (Fig. 15). On the contrary, the calculated simple mixing and AFC lines between the isotopic compositions of the CMG and MFG granites are in good agreement with mixing lines for the tonalite and granodiorite (Fig. 15). However, the simple mixing model between these two sources requires a very high ratio of

$\text{Hf}_{\text{pm}}/\text{Hf}_{\text{c}}$ (whole-rock Hf ratio between low $\delta^{18}\text{O}$ parental magma source and high $\delta^{18}\text{O}$ crustal source), and an extremely high degree of mixing (up to 80%), which are unrealistic (Kemp *et al.*, 2007). We suggest an AFC process between the sources of the CMG and MFG granites is the most plausible explanation for the data, although simple mixing between an undefined source having $\epsilon\text{Hf}(t)$ of $c. -15$ with $\sim 11\%$ $\delta^{18}\text{O}$ and the source rock of the CMG granite is also plausible (Fig. 15). The tonalites and granodiorites, therefore, are most likely derived from partial melting of Neoproterozoic low $\delta^{18}\text{O}$ basaltic rocks and experienced assimilation of high $\delta^{18}\text{O}$ crustal materials as well as fractional crystallization processes with negligible input of mantle-derived melts during magma ascent and emplacement.

CMG and MFG granites

The geochemical compositions of the CMG and MFG granites are similar to those of highly fractionated I-type granites (Fig. 11; Chappell & White, 2001). Although they are mainly peraluminous granites, the negative correlation between P_2O_5 and SiO_2 argues against typical S-type classification (Chappell & White, 2001; Wu *et al.*, 2003). The fractionation of monazite or allanite, which are common minerals in S-type granites, is not obvious in the CMG and MFG granites, which suggests these rocks are not derived from partial

Table 2: Starting compositions and partition coefficients used in the geochemical modeling

Rayleigh fractional crystallization model										
Element	C0	Kd Kf	Kd Pl	Kd Bt	Kd Mon	Kd Aln	Kd Mag	Kd Hb	Kd Ilm	
Rb	120	1.2	0.15	4	n.a.	0.19	0.045	0.37	n.a.	
Sr	700	3	7	0.45	n.a.	1.8	0.017	0.01	0.17	
Ba	1500	11	2	8	n.a.	n.a.	0.1	0.28	n.a.	
La	30	0.07	0.7	1.9(2.59)	481	820	0.8	0.36	1.31	
Ce	50	0.04	0.275	2.7(2.15)	476	635	1.02	0.68	1.19	
Nd	20	0.035	0.215	3.5(1.8)	487	463	1.5	1.6	0.96	
Yb	0.5	0.01	0.06	2.2(0.32)	41	8.9	1.1	1.8	0.55	
Lu	0.1	0.03	0.095	1.5(0.39)	33	7.7	0.91	1.8	0.74	
Th	10	0.025	0.055	0.32	563	168	0.1	0.16	0.427	
Y	8	0.067	0.120	1.4	107	95.5	0.12	8.28	0.21	

Batch partial melting model										
Elements	C ₀ (1-3)	C ₀ (4-5)	C ₀ (6)	Kd Grt	Kd Pl	Kd Amp	Kd Cpx	Kd Opx	Kd Bt	Kd Crd
La	13	20	13	0.009	0.125	0.089	0.28	0.022	0.06	0.06
Yb	1.7	3	1.7	15	0.087	3.786	1.2	1.097	1.47	1.77
Sr	320	400	300	0.01	2.262	0.358	0.28	0.033	0.01	0.12
Y	20	30	20	11.028	0.128	3.156	1.5	0.743	1.23	0.99

Elements	D (1) (Grt/Cpx/Amp) (50/35/15)	D (2) (Grt/Cpx/Amp/Pl) (15/40/40/5)	D (3) (Cpx/Amp/Pl/Opx) (40/45/10/5)	D (4) (Grt/Cpx/Amp/Pl) (10/40/40/10)	D (5) (Cpx/Amp/Pl) (10/60/30)	D (6) (Pl/Bt/Grt/Crd/Opx) (37/30/18/10/5)
La	0.12	0.16	0.17	0.16	0.12	0.07
Yb	8.49	4.25	2.25	3.50	2.42	3.41
Sr	0.16	0.37	0.50	0.48	0.92	0.86
Y	6.51	3.52	2.07	2.98	2.08	2.54

Note: D denotes the bulk distribution coefficients; Kd, partition coefficient of minerals; C₀, the weight concentration of elements in the source rock. The partition coefficients are from <https://earthref.org/GERM/KDD/>.

Kf, K-feldspar; Pl, Plagioclase; Amp, amphibole; Cpx, Clinopyroxene; Bt, biotite; Grt, Garnet; Opx, Orthopyroxene; Mon, monzonite; Aln, allanite; Mag, magnetite; Ilm, ilmenite; Crd, cordierite.

The partition coefficients in the brackets of biotite are used for Bt'.

The numbers in the brackets of batch partial melting model correspond to different melting curves in the Fig. 13.

Table 3: Parameters used for zircon Hf–O modeling

Assimilation and fractional crystallization (AFC) model			
D(Hf) = 0.42	r = 0.6	ΔO = -1.3	
	Hf (ppm)	εHf(t)	δ ¹⁸ O
Low δ ¹⁸ O end member 1 (CMG granite) (curve 1)	4	+1.5	5.2
Low δ ¹⁸ O end member 2 (mafic xenolith) (curve 2)	1.5	+4.1	5.9
High δ ¹⁸ O end member (MFG granite) (curve 1 and 2)	2	-14.7	9.3

Simple mixing model			
	Hf (ppm)	εHf(t)	δ ¹⁸ O
Low δ ¹⁸ O end member 1 (CMG granite) (curve 3 and 5)	16	+1.5	5.2
Low δ ¹⁸ O end member 2 (mafic xenolith) (curve 4)	1.5	+4.1	5.9
High δ ¹⁸ O end member 1 (MFG granite) (curve 3 and 4)	2	-14.7	9.3
High δ ¹⁸ O end member 2 (unseen rock) (curve 5)	5.3	-14.7	11.0

Note: D denotes the partition coefficient of Hf element; r is assimilation rate; ΔO = δ_{zircon} - δ_{magma} = δ_{zircon} - δ_{whole-rock} = -0.0612 × SiO₂ (in wt %) + 2.5 (Valley *et al.*, 2005), where SiO₂ = 62.5 (wt %) is used in this study.

The partition coefficients are from <https://earthref.org/GERM/KDD/>.

The AFC model and simple mixing model are based on DePaolo (1981).

melting of metapelites. The fluctuation of plagioclase An contents and the relatively high Mg# of some samples suggests periods of magma recharge and input of mafic magma (less than 5%) (Fig. 10b and c; Martin *et al.*, 2005). Our calculations suggest that minor input of mafic magma will not significantly change the trace

element concentrations (Fig. 12e–h). Moderate to low MgO and Mg# in the CMG and MFG granites (Fig. 11c and d) also indicate that they are chiefly derived from partial melting of a crustal source (Martin *et al.*, 2005). They display low Sr/Y, Zr/Hf and P₂O₅ contents and high Rb/Sr, along with wide range of δEu (~1.0 to 0.1),

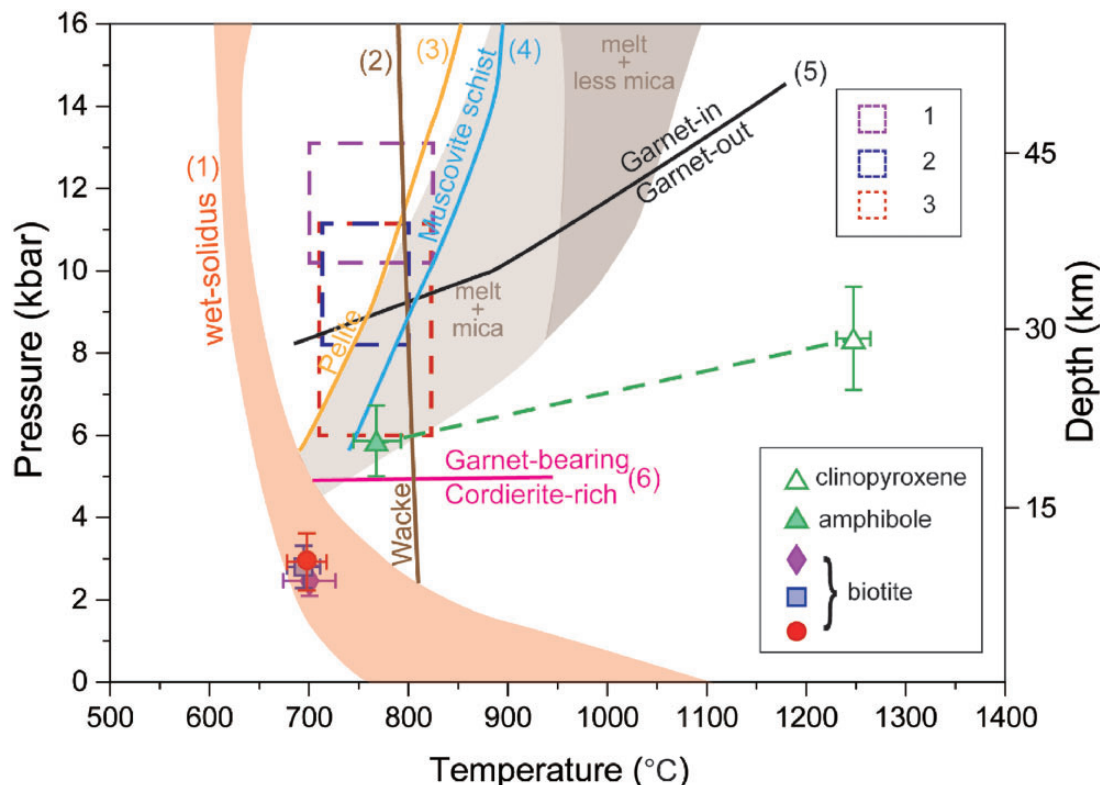


Fig. 16. The possible P - T conditions for melting and crystallization of the magmatic rocks from the Huayang intrusive complex. The data points represent P - T conditions calculated from mineral thermobarometry. The dashed rectangles (1–3) represent P - T conditions estimated from Zr-saturation thermometers (Watson & Harrison, 1983; Boehnke *et al.*, 2013) and Sr/Y and (La/Yb)_N ratios. (1: tonalites and granodiorites, 2: CMG granites, 3: MFG granites). Curves or fields for melting or mineral stability: (1) wet solidus area for crustal rocks (Vielzeuf & Montel, 1994; Patiño Douce & Beard, 1995; Patiño Douce & McCarthy, 1998; Patiño Douce, 2005; Qian & Hermann, 2013); (2–4) dehydration solidi for crustal rocks (Hacker *et al.*, 2014); (5) garnet-in/out curve during dehydration melting of metabasalts (Rapp & Watson, 1995); (6) the boundary line for garnet-bearing melts (above line) and cordierite-rich (below line) melts during dehydration melting of metasedimentary rocks (Wang *et al.*, 2012). The fields for melt + mica and melt + less mica are from Hacker *et al.* (2014). Legends as in Fig. 9.

indicating fractional crystallization of feldspar, zircon and apatite (Figs 11 and 12).

Most CMG and MFG granites show increasing Rb/Sr with decreasing Sr and Ba, and negative Eu anomalies, indicating they may be derived from vapour-absent muscovite-dehydration melting (Fig. 13a; Inger & Harris, 1993; Weinberg & Hasalová, 2015). However, these characteristics could also result from fractionation of feldspar, mainly plagioclase. The Langtang leucogranites (Himalaya), for which the vapour-absent muscovite-dehydration melting model was originally proposed, show positive correlation between LREE and Sr/Y (Inger & Harris, 1993), which is in contrast to our samples (Fig. 13c). This observation indicates that the geochemical characteristics of the CMG and MFG granites is most likely controlled by fractional crystallization processes.

The high Sr/Y and La/Yb samples with low SiO₂ can be used to trace the source materials and residues of partial melting. The highest Sr/Y (48.75 for CMG granite; 53.25 for MFG granite) and (La/Yb)_N (48.25 for CMG granite; 68.25 for MFG granite) ratios are most likely to be the result of either low-degree partial melting of basaltic to tonalitic rocks with plagioclase and amphibole

as major residual minerals or low-degree partial melting of metagreywackes with plagioclase + garnet + biotite as major residues (Fig. 13e, f; Kamei *et al.*, 2009; Qian & Hermann, 2013). Experimental studies have demonstrated that these rocks could be formed by melting of mafic crust at <12 kbar, corresponding to <40 km depth for typical continental crust (Conrad *et al.*, 1988; Qian & Hermann, 2013) or melting of metagreywackes at ~6–10 kbar (~20–30 km depth) (Moyen, 2009). The high La/Yb relative to Sr/Y of the MFG granites suggests that they originated from partial melting of metagreywackes (Fig. 13e and f; Otamendi & Patiño Douce, 2001; Moyen, 2009). Fractional crystallization of feldspar will lower Sr/Y and (La/Yb)_N (Fig. 13). The CMG and MFG granites plot in a variety of fields in source discrimination diagrams, including metabasaltic rocks, metagreywackes, and metapelites (Fig. 14a and b). This phenomenon could also be explained by fractional crystallization. The rocks display decreasing CaO and CMF values with increasing AMF values, which is mainly caused by fractionation of plagioclase (Fig. 14a and b). The low CaO with high CMF features are linked to the low Mg + Fe value, which may be related to fractionation of biotite and titanomagnetite (Fig. 14a and b).

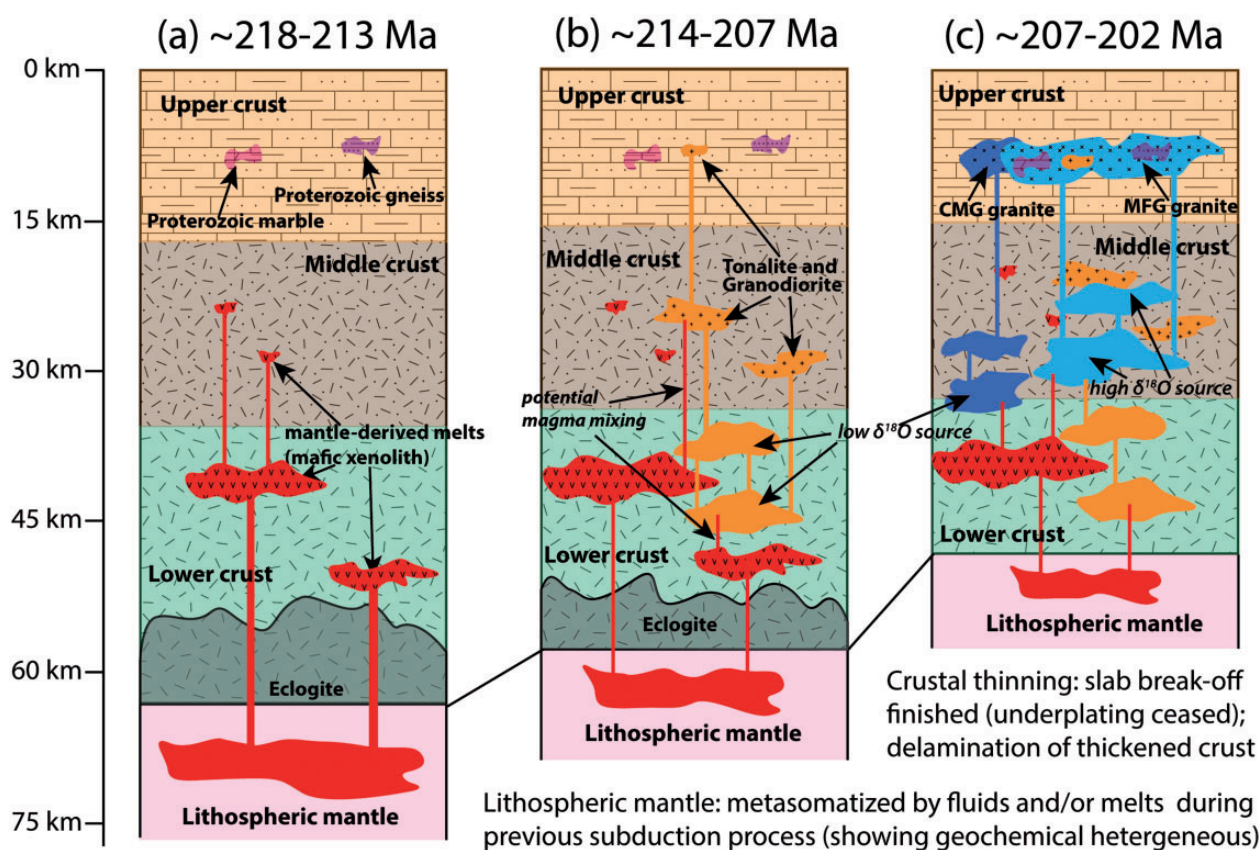


Fig. 17. Schematic lithospheric profiles of the SQB showing magma generation with time and interaction with each other in the SQB. (a) From ~218 to 213 Ma, partial melting of the lithospheric mantle generated mafic magma which was emplaced into the lower to middle crust. The lithospheric mantle source had been metasomatized by crustal-derived melts and, or, fluids during previous subduction cycles. (b) From ~214 to 207 Ma, low $\delta^{18}\text{O}$ metabasaltic rocks in the lower crust were heated by underplated mafic magmas and started to melt, forming tonalites and granodiorites after mixing with mafic magma and high $\delta^{18}\text{O}$ metagreywackes and finally emplaced at middle and upper crust depths. (c) From ~207 to 202 Ma, low $\delta^{18}\text{O}$ metabasaltic rocks and high $\delta^{18}\text{O}$ metagreywackes were heated and partially melted by underplated mafic magmas and formed the CMG granites and MFG granite magmas, respectively, after feldspar-dominated fractionation and were finally emplaced in the upper crust. Magma mixing and crustal assimilation also took place. The parental magmas of the CMG and MFG granites entrained xenoliths of Proterozoic sedimentary rocks, marble and mafic rocks, and were intruded into the tonalites and granodiorites. The intensity of mantle-derived magmatism decreased with time resulting in the crust-derived magma becoming progressively richer in silica. Intense fractional crystallization contributed to the formation of the high-silica rocks. Mafic magmas could be responsible for crustal growth in the SQB. However, the continental crust in the SQB had started to thin since ~210 Ma (Hu *et al.*, 2017a) and such a mechanism may lead to the newly-formed continental crust becoming delaminated into the mantle. Therefore, the amount of crustal growth during the post-collision period is still enigmatic.

The decreasing $\text{CaO}/\text{Na}_2\text{O}$ and increasing $\text{Al}_2\text{O}_3/\text{TiO}_2$, Th/La , and SiO_2 also suggest the separation of plagioclase (Fig. 14c and d).

Zircon Hf–O isotope data provide detailed information about the source rocks of the CMG and MFG granites. The granites have Hf isotopic compositions similar to those of the tonalites and granodiorites, although the MFG granites have more negative $\epsilon_{\text{Hf}}(t)$ values (-14.7 to +1.1) compared to the CMG granites (-7.3 to +1.5). In addition to the Hf isotopic evidence, the occurrence of ~743 Ma inherited ages in zircon crystals suggest that the CMG and MFG granites were mainly derived from partial melting of the Neoproterozoic basement rocks of the SQB (Fig. 7). It is also possible that they could be derived from partial melting of late Triassic basaltic rocks (the protolith of the mafic xenoliths and MME) because these also show similar $\epsilon_{\text{Hf}}(t)$ values to these

granitoids (Fig. 7). However, the analysed zircon $\delta^{18}\text{O}$ isotope compositions of the CMG and MFG granite samples are distinctly different from each other and from the mafic xenoliths (Fig. 8). The CMG granite sample (16HY06-2) has mantle-like zircon $\delta^{18}\text{O}$ values (average 5.7‰), whereas the MFG granite sample (16HY04-1) shows zircon $\delta^{18}\text{O}$ values more typical of sedimentary rocks (average 8.4‰) (Fig. 8). Therefore, the source of CMG granites may be Neoproterozoic meta-igneous rocks which did not experience near-surface hydrologic exposure that could have raised the zircon $\delta^{18}\text{O}$ values. The source of the MFG granites is interpreted to be Neoproterozoic metagreywackes (Bindeman, 2008). It is worth noting that a negative correlation between SiO_2 and P_2O_5 is a typical feature used to discriminate I-type granites from S-type granites (Chappell & White, 2001; Wu *et al.*, 2003). The high $\delta^{18}\text{O}$ of the MFG granites

suggests that they may be S-type granites (Lu *et al.*, 2016), however, the negative correlation between SiO₂ and P₂O₅ for these rocks suggest that criterion is not suitable for all S-type granites (Fig. 11h; Chappell & White, 2001). The range of variation of zircon $\delta^{18}\text{O}$ in the MFG granites suggest there may have been magma assimilation or mixing, which is consistent with the relatively high Mg#, reverse zoning of plagioclases in some samples, and the existence of $\sim 11\%$ $\delta^{18}\text{O}$ zircon in the granites (Figs 8, 10 and 11; Lu *et al.*, 2016). Because of the similar whole-rock geochemistry between the CMG and MFG granites, we hypothesize that they were both formed from similar source materials, and that the high $\delta^{18}\text{O}$ values may reflect altered or weathered low $\delta^{18}\text{O}$ source rocks. We suggest that the CMG granites are mainly derived from low $\delta^{18}\text{O}$ Neoproterozoic metabasaltic to metatonalitic rocks, and that the MFG granites are mainly derived from high $\delta^{18}\text{O}$ Neoproterozoic metagreywackes. Both granites experienced feldspar-dominated fractional crystallization.

Interaction among magmas from various sources

We suggest that multiple magmas interacted with each other in the SQB during continental collision. Chronologically, the mantle-derived magmas (represented by the mafic xenoliths) were formed first in the Huayang area (Fig. 6). They share the same age (~ 218 – 213 Ma) with widespread MME (~ 220 – 210 Ma) in the SQB (Hu *et al.*, 2016b, 2017b). The zircon Hf–O isotopic compositions of the mafic xenoliths suggest that they were derived from an enriched sub-continental lithospheric mantle source. These mantle-derived magmas mainly occur as MME in granitoid intrusions (e.g. Dongjiangkou–Caoping–Shahewan intrusions) reflecting a magma mixing process (Qin *et al.*, 2010, 2013; Liu *et al.*, 2011a; Yang *et al.*, 2012; Hu *et al.*, 2016b, 2017b). The majority of these mafic magmas would likely have been emplaced in the lower crust due to their density and our calculations suggest that they would be emplaced at middle crust depths (~ 20 km; Figs 16 and 17a).

The tonalites and granodiorites formed slightly after the emplacement of the mafic magmas, between ~ 214 and 207 Ma (Fig. 6; Liu *et al.*, 2011b). Their low MgO contents and Mg# values, relative to the granitoids associated with MME (e.g. the ~ 218 – 215 Ma Xiba intrusion and ~ 214 – 212 Ma Xichahe intrusion in the adjacent area) (Fig. 11; Qin *et al.*, 2008; Zhang *et al.*, 2012), suggest they are mainly derived from a crustal source with limited input of mantle-derived magma (possibly less than 5%). The zircon Hf–O isotope data indicate that the tonalites and granodiorites were derived from low $\delta^{18}\text{O}$ Neoproterozoic metabasaltic rocks and that the parental magmas were contaminated by high $\delta^{18}\text{O}$ metagreywackes (Fig. 15; Lu *et al.*, 2016). The calculated P – T conditions, based on biotite, suggest crystallization near the wet solidus at shallow depths (~ 10 km), reflecting upper crustal emplacement (Figs 16 and 17b). The Zr-saturation thermometer and high Sr/Y and La/Yb ratios

suggest that the tonalites and granodiorites formed at higher temperatures and pressures, possibly at ~ 40 – 45 km depth (Figs 13 and 16; Qian & Hermann, 2013).

The biotite granites in the Huayang intrusive complex formed between ~ 207 and 202 Ma, marking the final stage of magmatism in the SQB during continental collision (Dong & Santosh, 2016; Hu *et al.*, 2016b, 2017b). Their whole-rock geochemical compositions (Figs 11 and 12) reflect feldspar-dominated fractional crystallization and zircon Hf–O isotopic data indicate that they were derived from two different crustal sources (Figs 13–15). One of the sources was low $\delta^{18}\text{O}$ metabasaltic to metatonalitic rocks and the other source was high $\delta^{18}\text{O}$ metagreywackes. The calculated crystallization P – T conditions based on biotite plot on the wet solidus at shallow depths (~ 10 km) (Figs 16 and 17c). However, Zr-saturation thermometry and the Sr/Y and La/Yb ratios of the most primitive samples of the CMG and MFG granites suggest that they originated from greater depths (~ 20 – 40 km) and higher temperatures (Figs 13 and 16; Qian & Hermann, 2013). Because the MFG granites were derived from partial melting of metagreywackes, we estimate they may have formed at shallower depths than the CFG granites (Figs 16 and 17c). As some samples of the CMG and MFG granites have high Mg# values and record reverse zoning in plagioclase, we propose that melting of the sub-continental lithospheric mantle continued from ~ 207 to 202 Ma.

In conclusion, at least three different source materials are involved in the late Triassic magmatism in the SQB, including lithospheric mantle-derived mafic magmas, Neoproterozoic low $\delta^{18}\text{O}$ (metabasaltic to metatonalitic rocks), and high $\delta^{18}\text{O}$ (metagreywackes) crustal rocks (Fig. 17). The low $\delta^{18}\text{O}$ crustal rocks in the lower and middle crust were heated by the mantle-derived magmas, which are interpreted to have been underplated. Heat from underplating may have melted the crustal source rocks to generate the parental magma of the tonalites, granodiorites, and CMG granites. The high $\delta^{18}\text{O}$ crustal rocks in the middle and upper crust are also interpreted to have been heated by the mantle-derived magmas, forming the MFG granites. The melts derived from low $\delta^{18}\text{O}$ crustal rocks were contaminated by high $\delta^{18}\text{O}$ crustal rocks during magma ascent and emplacement.

Crustal melting mechanism during continental collision

Continental subduction and ultra-high pressure metamorphism in the Dabie Orogen has been confirmed by the presence of coesite-bearing eclogites (Zhang *et al.*, 2009). Continental subduction was also proposed to have occurred in the QOB, but structural and metamorphic studies suggest that the subduction depth was relatively shallow (Ratschbacher *et al.*, 2003; Wu & Zheng, 2013; Hu *et al.*, 2016b). The Dabie Orogen has a similar basement and Mesozoic tectonic evolutionary

history to the QOB (Wu & Zheng, 2013; Dong & Santosh, 2016). The granites in the QOB and the Dabie Orogen have similar Th (mostly ~10–20 ppm), U (mostly <5 ppm) and K₂O (high-K series) contents (Xu *et al.*, 2007, 2013; Jiang *et al.*, 2010; Qin *et al.*, 2010, 2013; Wang *et al.*, 2011; Deng *et al.*, 2016; Hu *et al.*, 2016b, 2017b), suggesting similar amounts of heat-producing elements in both orogens. Therefore, the crustal melting in the QOB is not required to solely depend on radioactive heating of the thickened crust (Zheng, 2008; Bea, 2012). Evidence for extensive Late Triassic mantle-derived melts in the SQB (e.g. MME in the granitoid intrusions, mafic dykes and mafic xenoliths) is compatible with crustal melting in the QOB during continental collision related to heating from these high-temperature mafic melts (Hu *et al.*, 2016b, 2017b).

Mantle-derived mafic magmatism in the SQB was coeval with retrograde metamorphism in the Dabie Orogen, which has been interpreted to be related to break-off of subducted oceanic lithosphere and melting of overlying sub-continental lithospheric mantle (Zhang *et al.*, 2009; Hu *et al.*, 2016b). Mantle melting would be suppressed if slab detachment occurred in the deep mantle, which has been proposed for the Dabie Orogen (Atherton & Ghani, 2002; Hu *et al.*, 2016b). Therefore, deep slab break-off could explain the lack of magmatism in the Dabie Orogen and shallow slab break-off could explain the magmatism in the QOB (Davies & von Blanckenburg, 1995; Atherton & Ghani, 2002; Hu *et al.*, 2016b; Wang *et al.*, 2016). Nevertheless, slab break-off is not the only possible explanation (Niu, 2017). If the oceanic slab did not fully break-off, dehydration of oceanic crust during continental collision could induce partial melting of the lithospheric mantle (Zhu *et al.*, 2015). However, dehydration of subducted continental crust will only induce small-scale regional anatexis (Zhang *et al.*, 2011). The deep subduction of continental crust (>120 km) (Zhang *et al.*, 2009), therefore, could suppress the dehydration of the oceanic slab and only release a small amount of fluids. In addition, the lithospheric mantle beneath the Dabie Orogen may not have been fertile enough to generate significant volumes of partial melt. In contrast, more water may be released from the oceanic slab due to shallow continental subduction in the QOB which then induced melting of the lithospheric mantle. Both mechanisms, slab break-off and dehydration of the slab, could be responsible for the partial melting of the sub-continental lithospheric mantle during syn-collisional orogenesis. The underplated mafic magmas that we postulate are responsible for the evolution of the QOB have also been suggested to have thickened the continental crust during continental collision (Hu *et al.*, 2017a; Zhu *et al.*, 2017).

Mantle-derived mafic magmas provide heat for melting lower crustal metabasaltic rocks which could then further mix with crustal-derived felsic magmas to generate I-type granitoid intrusions with abundant MME in the SQB (Annen *et al.*, 2006; Hu *et al.*, 2016b, 2017b). However, the mechanism for generating S-type granites

in the SQB (e.g. Yanzhiba muscovite-bearing granite, Guangtoushan two-mica granite, and the Huayang MFG granite) may be slightly different. These rocks are mainly derived from partial melting of sedimentary rocks in the middle to upper crust with limited to no input of mafic magma (Yang *et al.*, 2012; Deng *et al.*, 2016; Lu *et al.*, 2016). In addition, shallowly subducted sediments may be incorporated into the melt source region (Zheng *et al.*, 2011; Lu *et al.*, 2016). It should be noted that almost all of the S-type granites in the SQB were formed during the post-collision (<210 Ma) stage in contrast to the I-type granitoids (mainly formed between ~225 and 210 Ma) (Yang *et al.*, 2012; Deng *et al.*, 2016; Hu *et al.*, 2016b). This reflects the decreasing intensity of mafic magmatism resulting in little magma mixing, which is also evidenced by the presence of only minor amounts of mafic rocks exposed after ~210 Ma in the SQB (Patiño Douce, 1999; Bea, 2012; Dong & Santosh, 2016). The decreasing of the intensity of mafic magmatism may be related to slab foundering and/or dehydration of slab. The scale of lithospheric delamination may be limited during the post-collisional period because of the lack of extensive magmatism in the SQB at this time (Dong & Santosh, 2016; Hu *et al.*, 2017a). In comparison to oceanic subduction zones where adding water to the mantle wedge is the primary mechanism for generating magma, the data from the SQB suggests that heat provided by mafic magmas may be the key factor for initiating crustal melting during continental collision.

CONCLUSIONS

(1) Initial continental collision in the SQB occurred prior to ~230 Ma and regional extension started at ~210 Ma. The Huayang intrusive complex formed during the syn-collision to post-collision stage and is mainly composed of ~207–202 Ma CMG and MFG biotite granites, and small amounts of ~214–207 Ma tonalites and granodiorites, with rare ~218–213 Ma mafic xenoliths.

(2) The parental magmas of the mafic xenoliths were derived from partial melting of a phlogopite-bearing sub-continental lithospheric mantle source. The tonalites and granodiorites were derived from partial melting of low $\delta^{18}\text{O}$ Neoproterozoic basaltic rocks, followed by assimilation of high $\delta^{18}\text{O}$ crustal materials, and experienced fractional crystallization of plagioclase. The CMG granites originated from partial melting of low $\delta^{18}\text{O}$ Neoproterozoic metabasaltic to metatonalitic rocks, and the MFG granites were derived from high $\delta^{18}\text{O}$ Neoproterozoic metagreywackes. Both granite types experienced plagioclase-dominated fractional crystallization during magma ascent and emplacement. Mixing of mantle-derived mafic magmas into the granitoid magmas was negligible. Three different melt source materials were involved in continental collisional magmatism in the SQB including: lithospheric mantle, Neoproterozoic low $\delta^{18}\text{O}$ metabasaltic to metatonalitic rocks, and Neoproterozoic high $\delta^{18}\text{O}$ metagreywackes.

(3) Based on Zr-saturation thermometry, experimental petrology and mineral thermobarometry, we suggest: (a) mafic magmas were emplaced in the middle crust (~20 km); (b) the parental magmas of the tonalites and granodiorites originated in the lower crust (~35–45 km) and were emplaced in the upper crust (~10 km), and (c) the parental magmas of the CMG and MFG granites were formed in the lower to middle crust (~20–40 km) and were emplaced in the upper crust (~10 km).

(4) Slab break-off and/or dehydration of a subducted slab may induce melting of the sub-continental lithospheric mantle. Melts derived from the lithospheric mantle may provide heat for crustal melting and could mix with crustal-derived melts during continental collision.

ACKNOWLEDGEMENTS

We are grateful to Editor Simon Turner and Executive Editor Marjorie Wilson, an anonymous reviewer and Georg Zellmer for their thoughtful and insightful reviews, which greatly improved the original manuscript. We also want to thank Kenneth Domanik for assistance during mineral electron microprobe analyses at the Electron Microprobe Laboratory of University of Arizona, Li Chen for CL imaging at the Electron Microscopy Laboratory of Peking University, Bin Yang and Libing Gu and Fang Ma at the Key Laboratory of Orogenic Belts and Crustal Evolution, Peking University for help with whole-rock major and trace element and zircon U–Th–Pb isotopic analyses, Xiaoxiao Ling for assistance with zircon U–Pb–O isotopic analyses at the Institute of Geology and Geophysics, Chinese Academy of Science in Beijing, and Prof. Zhaochu Hu for assistance with zircon Lu–Hf isotopic analyses at the State Key Laboratory of Geological Process and Mineral Resources, China University of Geosciences, Wuhan.

FUNDING

This work was supported by the National Natural Science Foundation of China [41530207, 41772188 to S.W.L.], the Romanian Executive Agency for Higher Education, Research, Development and Innovation Funding project [PN-III-P4-ID-PCE-2016–0127 to M.N.D.], the China Geological Survey (1212011085534 to S.W.L.), and China Scholarship Council [201606010070 to F.Y.H.].

SUPPLEMENTARY DATA

Supplementary data are available at *Journal of Petrology* online.

REFERENCES

- Altherr, R., Holl, A., Hegner, E., Langer, C. & Kreuzer, H. (2000). High-potassium, calc-alkaline I-type plutonism in the European Variscides: northern Vosges (France) and northern Schwarzwald (Germany). *Lithos* **50**, 51–73.
- Andersen, T. (2002). Correction of common lead in U–Pb analyses that do not report ^{204}Pb . *Chemical Geology* **192**, 59–79.
- Annen, C., Blundy, J. D. & Sparks, R. S. J. (2006). The Genesis of intermediate and silicic magmas in deep crustal hot zones. *Journal of Petrology* **47**, 505–539.
- Atherton, M. P. & Ghani, A. A. (2002). Slab breakoff: a model for Caledonian, Late Granite syn-collisional magmatism in the orthotectonic (metamorphic) zone of Scotland and Donegal, Ireland. *Lithos* **62**, 65–85.
- Barbarin, B. (2005). Mafic magmatic enclaves and mafic rocks associated with some granitoids of the central Sierra Nevada batholith, California: nature, origin, and relations with the hosts. *Lithos* **80**, 155–177.
- Bea, F. (2012). The sources of energy for crustal melting and the geochemistry of heat-producing elements. *Lithos* **153**, 278–291.
- Bindeman, I. (2008). Oxygen isotopes in mantle and crustal magmas as revealed by single crystal analysis. *Reviews in Mineralogy and Geochemistry* **69**, 445–478.
- Blasband, B., White, S., Brooijmans, P., de Boorder, H. & Visser, W. (2000). Late Proterozoic extensional collapse in the Arabian–Nubian Shield. *Journal of the Geological Society* **157**, 615–628.
- Blichert-Toft, J. (2008). The Hf isotopic composition of zircon reference material 91500. *Chemical Geology* **253**, 252–257.
- Blichert-Toft, J. & Albarède, F. (1997). The Lu–Hf isotope geochemistry of chondrites and the evolution of the mantle-crust system. *Earth and Planetary Science Letters* **148**, 243–258.
- Blundy, J. D. & Holland, T. J. B. (1990). Calcic amphibole equilibria and a new amphibole-plagioclase geothermometer. *Contributions to Mineralogy and Petrology* **104**, 208–224.
- Boehnke, P., Watson, E. B., Trail, D., Harrison, T. M. & Schmitt, A. K. (2013). Zircon saturation re-revisited. *Chemical Geology* **351**, 324–334.
- Bonin, B. (2004). Do coeval mafic and felsic magmas in post-collisional to within-plate regimes necessarily imply two contrasting, mantle and crustal, sources? A review. *Lithos* **78**, 1–24.
- Bouilhol, P., Jagoutz, O., Hanchar, J. M. & Dudas, F. O. (2013). Dating the India–Eurasia collision through arc magmatic records. *Earth and Planetary Science Letters* **366**, 163–175.
- Cai, F., Ding, L. & Yue, Y. (2011). Provenance analysis of upper Cretaceous strata in the Tethys Himalaya, southern Tibet: implications for timing of India–Asia collision. *Earth and Planetary Science Letters* **305**, 195–206.
- Castillo, P. R. (2012). Adakite petrogenesis. *Lithos* **134–135**, 304–316.
- Chapman, J. B., Scoggin, S. H., Kapp, P., Carrapa, B., Ducea, M. N., Worthington, J., Oimahmadov, I. & Gadoev, M. (2018). Mesozoic to Cenozoic magmatic history of the Pamir. *Earth and Planetary Science Letters* **482**, 181–192.
- Chappell, B. W. & White, A. J. R. (2001). Two contrasting granite types: 25 years later. *Australian Journal of Earth Sciences* **48**, 489–499.
- Chappell, B. W., White, A. J. R. & Wyborn, D. (1987). The importance of residual source material (restite) in granite petrogenesis. *Journal of Petrology* **28**, 1111–1138.
- Chen, H., Hu, J. M., Wu, G. L. & Gao, W. (2010). Study on the intracontinental deformation of the Mian-Lue suture belt, western Qinling. *Acta Petrologica Sinica* **26**, 1277–1288. (in Chinese with English abstract).
- Chung, S.-L., Chu, M.-F., Zhang, Y., Xie, Y., Lo, C.-H., Lee, T.-Y., Lan, C.-Y., Li, X., Zhang, Q. & Wang, Y. (2005). Tibetan tectonic evolution inferred from spatial and temporal variations in post-collisional magmatism. *Earth-Science Reviews* **68**, 173–196.

- Clarke, D. B. (1981). The mineralogy of peraluminous granites; a review. *The Canadian Mineralogist* **19**, 3–17.
- Clemens, J. D. & Stevens, G. (2012). What controls chemical variation in granitic magmas? *Lithos* **134–135**, 317–329.
- Conrad, W. K., Nicholls, I. A. & Wall, V. J. (1988). Water-saturated and-undersaturated melting of metaluminous and peraluminous crustal compositions at 10 kb: evidence for the origin of silicic magmas in the Taupo Volcanic Zone, New Zealand, and other occurrences. *Journal of Petrology* **29**, 765–803.
- Corfu, F., Hanchar, J. M., Hoskin, P. W. O. & Kinny, P. (2003). Atlas of zircon textures. *Reviews in Mineralogy and Geochemistry* **53**, 469–500.
- Couzinié, S., Laurent, O., Moyen, J.-F., Zeh, A., Bouilhol, P. & Villaros, A. (2016). Post-collisional magmatism: crustal growth not identified by zircon Hf–O isotopes. *Earth and Planetary Science Letters* **456**, 182–195.
- Davies, J. H. & von Blanckenburg, F. (1995). Slab breakoff: a model of lithosphere detachment and its test in the magmatism and deformation of collisional orogens. *Earth and Planetary Science Letters* **129**, 85–102.
- Deng, Z. B., Liu, S. W., Zhang, W. Y., Hu, F. Y. & Li, Q. G. (2016). Petrogenesis of the Guangtoushan granitoid suite, central China: implications for Early Mesozoic geodynamic evolution of the Qinling Orogenic Belt. *Gondwana Research* **30**, 112–131.
- DePaolo, D. J. (1981). Trace element and isotopic effects of combined wallrock assimilation and fractional crystallization. *Earth and Planetary Science Letters* **53**, 189–202.
- Dilek, Y. & Altunkaynak, S. (2007). Cenozoic crustal evolution and mantle dynamics of post-collisional magmatism in Western Anatolia. *International Geology Review* **49**, 431–453.
- Ding, L., Kapp, P. & Wan, X. (2005). Paleocene–Eocene record of ophiolite obduction and initial India–Asia collision, south central Tibet. *Tectonics* **24**, TC3001.
- Ding, X., Sun, W. D., Wang, F. Y., Chen, L. L., Li, Q. L. & Chen, F. K. (2012). Single-grain mica Rb–Sr isochron ages and mineral chemistry for the Weishan pluton in Hunan Province and implications on petrogenesis and mineralization of Mesozoic composite granite in South China. *Acta Petrologica Sinica* **28**, 3823–3840. (in Chinese with English abstract).
- Dong, Y. P. & Santosh, M. (2016). Tectonic architecture and multiple orogeny of the Qinling Orogenic Belt, Central China. *Gondwana Research* **29**, 1–40.
- Dong, Y. P., Zhang, G. W., Neubauer, F., Liu, X. M., Genser, J. & Hauzenberger, C. (2011). Tectonic evolution of the Qinling orogen, China: review and synthesis. *Journal of Asian Earth Sciences* **41**, 213–237.
- Dong, Y. P., Liu, X. M., Santosh, M., Chen, Q., Zhang, X. N., Li, W., He, D. F. & Zhang, G. W. (2012). Neoproterozoic accretionary tectonics along the northwestern margin of the Yangtze Block, China: constraints from zircon U–Pb geochronology and geochemistry. *Precambrian Research* **196–197**, 247–274.
- Dong, Y. P., Sun, S. S., Yang, Z., Liu, X. M., Zhang, F. F., Li, W., Cheng, B., He, D. F. & Zhang, G. W. (2017). Neoproterozoic subduction-accretionary tectonics of the South Qinling Belt, China. *Precambrian Research* **293**, 73–90.
- Ducea, M. N., Paterson, S. R. & DeCelles, P. G. (2015a). High-volume magmatic events in subduction systems. *Elements* **11**, 99–104.
- Ducea, M. N., Saleeby, J. B. & Bergantz, G. (2015b). The architecture, chemistry, and evolution of continental magmatic arcs. *Annual Review of Earth and Planetary Sciences* **43**, 299–331.
- Foley, S. (1992). Vein-plus-wall-rock melting mechanisms in the lithosphere and the origin of potassic alkaline magmas. *Lithos* **28**, 435–453.
- Foster, M. D. (1960). Interpretation of the composition of trioctahedral micas. *United States Geological Survey Professional Paper* **354**, 1–49.
- Furman, T. & Graham, D. (1999). Erosion of lithospheric mantle beneath the East African Rift system: geochemical evidence from the Kivu volcanic province. *Lithos* **48**, 237–262.
- Gao, S., Rudnick, R. L., Yuan, H. L., Liu, X. M., Liu, Y. S., Xu, W. L., Ling, W. L., Ayers, J., Wang, X. C. & Wang, Q. H. (2004). Recycling lower continental crust in the North China craton. *Nature* **432**, 892–897.
- Girbacea, R. & Frisch, W. (1998). Slab in the wrong place: lower lithospheric mantle delamination in the last stage of the Eastern Carpathian subduction retreat. *Geology* **26**, 611–614.
- Griffin, W. L., Pearson, N. J., Belousova, E., Jackson, S. E., van Achterbergh, E., O'Reilly, S. Y. & Shee, S. R. (2000). The Hf isotope composition of cratonic mantle: LAM–MC–ICPMS analysis of zircon megacrysts in kimberlites. *Geochimica et Cosmochimica Acta* **64**, 133–147.
- Grove, T. L., Till, C. B. & Krawczynski, M. J. (2012). The Role of H₂O in subduction zone magmatism. *Annual Review of Earth and Planetary Sciences* **40**, 413–439.
- Hacker, B. R., Ritzwoller, M. H. & Xie, J. (2014). Partially melted, mica-bearing crust in Central Tibet. *Tectonics* **33**, 1408–1424.
- Harley, S. L., Kelly, N. M. & Moller, A. (2007). Zircon behaviour and the thermal histories of mountain chains. *Elements* **3**, 25–30.
- Harris, N. B. W., Pearce, J. A. & Tindle, A. G. (1986). Geochemical characteristics of collision-zone magmatism. *Geological Society, London, Special Publications* **19**, 67–81.
- Hawthorne, F. C., Oberti, R., Harlow, G. E., Maresch, W. V., Martin, R. F., Schumacher, J. C. & Welch, M. D. (2012). Nomenclature of the amphibole supergroup. *American Mineralogist* **97**, 2031–2048.
- Henry, D. J., Guidotti, C. V. & Thomson, J. A. (2005). The Ti-saturation surface for low-to-medium pressure metapelitic biotites: Implications for geothermometry and Ti-substitution mechanisms. *American Mineralogist* **90**, 316–328.
- Hosseinpour, M., Williams, S., Seton, M., Barnett-Moore, N. & Müller, R. D. (2016). Tectonic evolution of Western Tethys from Jurassic to present day: coupling geological and geophysical data with seismic tomography models. *International Geology Review* **58**, 1616–1645.
- Hu, F. Y., Ducea, M. N., Liu, S. W. & Chapman, J. B. (2017a). Quantifying crustal thickness in continental collisional belts: global perspective and a geologic application. *Scientific Reports* **7**, 7058.
- Hu, F., Liu, S., Ducea, M. N., Zhang, W. & Deng, Z. (2017b). The geochemical evolution of the granitoid rocks in the South Qinling Belt: insights from the Dongjiangkou and Zhashui intrusions, central China. *Lithos* **278–281**, 195–214.
- Hu, F. Y., Liu, S. W., Santosh, M., Deng, Z. B., Wang, W., Zhang, W. Y. & Yan, M. (2016a). Chronology and tectonic implications of Neoproterozoic blocks in the South Qinling Orogenic Belt, Central China. *Gondwana Research* **30**, 24–47.
- Hu, F. Y., Liu, S. W., Zhang, W. Y., Deng, Z. B. & Chen, X. (2016b). A westward propagating slab tear model for Late Triassic Qinling Orogenic Belt geodynamic evolution: insights from the petrogenesis of the Caoping and Shahewan intrusions, central China. *Lithos* **262**, 486–506.
- Hu, S., Raza, A., Min, K., Kohn, B. P., Reiners, P. W., Ketcham, R. A., Wang, J. & Gleadow, A. J. W. (2006). Late Mesozoic and Cenozoic thermotectonic evolution along a transect from

- the north China craton through the Qinling orogen into the Yangtze craton, central China. *Tectonics* **25**, TC6009.
- Hu, Z., Liu, Y., Gao, S., Liu, W., Zhang, W., Tong, X., Lin, L., Zong, K., Li, M., Chen, H., Zhou, L. & Yang, L. (2012). Improved in situ Hf isotope ratio analysis of zircon using newly designed X skimmer cone and jet sample cone in combination with the addition of nitrogen by laser ablation multiple collector ICP-MS. *Journal of Analytical Atomic Spectrometry* **27**, 1391–1399.
- Inger, S. & Harris, N. (1993). Geochemical constraints on leucogranite magmatism in the Langtang Valley, Nepal Himalaya. *Journal of Petrology* **34**, 345–368.
- Jagoutz, O. & Kelemen, P. B. (2015). Role of arc processes in the formation of continental crust. *Annual Review of Earth and Planetary Sciences* **43**, 363–404.
- Jiang, Y.-H., Jin, G.-D., Liao, S.-Y., Zhou, Q. & Zhao, P. (2010). Geochemical and Sr–Nd–Hf isotopic constraints on the origin of Late Triassic granitoids from the Qinling orogen, central China: implications for a continental arc to continent–continent collision. *Lithos* **117**, 183–197.
- Jiang, Y.-H., Jin, G.-D., Liao, S.-Y., Zhou, Q. & Zhao, P. (2012). Petrogenesis and tectonic implications of ultrapotassic microgranitoid enclaves in Late Triassic arc granitoids, Qinling orogen, central China. *International Geology Review* **54**, 208–226.
- Kamei, A., Miyake, Y., Owada, M. & Kimura, J. I. (2009). A pseudo adakite derived from partial melting of tonalitic to granodioritic crust, Kyushu, southwest Japan arc. *Lithos* **112**, 615–625.
- Kemp, A. I. S., Hawkesworth, C. J., Foster, G. L., Paterson, B. A., Woodhead, J. D., Hergt, J. M., Gray, C. M. & Whitehouse, M. J. (2007). Magmatic and crustal differentiation history of granitic rocks from Hf–O isotopes in zircon. *Science* **315**, 980–983.
- Lai, S., Qin, J., Chen, L. & Grapes, R. (2008). Geochemistry of ophiolites from the Mian-Lue suture zone: implications for the tectonic evolution of the Qinling Orogen, Central China. *International Geology Review* **50**, 650–664.
- Lee, C. T. A., Cheng, X. & Horodyskyj, U. (2006). The development and refinement of continental arcs by primary basaltic magmatism, garnet pyroxenite accumulation, basaltic recharge and delamination: insights from the Sierra Nevada, California. *Contributions to Mineralogy and Petrology* **151**, 222–242.
- Li, J. Y., Wang, Z. Q. & Zhao, M. (1999). $^{40}\text{Ar}/^{39}\text{Ar}$ thermochronological constraints on the timing of collisional orogeny in the Mian–Lue collision belt, southern Qinling Mountains. *Acta Geologica Sinica - English Edition* **73**, 208–215. (in Chinese with English abstract).
- Li, N., Chen, Y. J., Santosh, M. & Pirajno, F. (2015). Compositional polarity of Triassic granitoids in the Qinling Orogen, China: implication for termination of the northernmost paleo-Tethys. *Gondwana Research* **27**, 244–257.
- Li, Q. L., Li, X. H., Liu, Y., Tang, G. Q., Yang, J. H. & Zhu, W. G. (2010a). Precise U–Pb and Pb–Pb dating of Phanerozoic baddeleyite by SIMS with oxygen flooding technique. *Journal of Analytical Atomic Spectrometry* **25**, 1107–1113.
- Li, S., Kusky, T. M., Wang, L., Zhang, G., Lai, S., Liu, X., Dong, S. & Zhao, G. (2007). Collision leading to multiple-stage large-scale extrusion in the Qinling orogen: insights from the Mianlue suture. *Gondwana Research* **12**, 121–143.
- Li, X.-H., Liu, Y., Li, Q.-L., Guo, C.-H. & Chamberlain, K. R. (2009). Precise determination of Phanerozoic zircon Pb/Pb age by multicollector SIMS without external standardization. *Geochemistry Geophysics Geosystems* **10**, Q04010.
- Li, X.-H., Long, W.-G., Li, Q.-L., Liu, Y., Zheng, Y.-F., Yang, Y.-H., Chamberlain, K. R., Wan, D.-F., Guo, C.-H., Wang, X.-C. & Tao, H. (2010b). Penglai zircon megacrysts: a potential new working reference material for microbeam determination of Hf–O isotopes and U–Pb age. *Geostandards and Geoanalytical Research* **34**, 117–134.
- Li, X.-W., Mo, X.-X., Yu, X.-H., Ding, Y., Huang, X.-F., Wei, P. & He, W.-Y. (2013a). Geochronological, geochemical and Sr–Nd–Hf isotopic constraints on the origin of the Cretaceous intraplate volcanism in West Qinling, Central China: implications for asthenosphere–lithosphere interaction. *Lithos* **177**, 381–401.
- Li, X., Tang, G., Gong, B., Yang, Y., Hou, K., Hu, Z., Li, Q., Liu, Y. & Li, W. (2013b). Qinghu zircon: a working reference for microbeam analysis of U–Pb age and Hf and O isotopes. *Chinese Science Bulletin* **58**, 4647–4654.
- Liégeois, J. P. (1998). Some words on the post-collisional magmatism. *Lithos* **45**, 15–18.
- Ling, W. L., Reng, B. F., Duan R. C., Liu X. M., Mao X. W., Peng L. H., Liu Z. X., Cheng J. P. & Yang, H.M. (2008). Timing of the Wudangshan, Yaolinghe volcanic sequences and mafic sills in South Qinling: U–Pb zircon geochronology and tectonic implication. *Science Bulletin* **53**, 2192–2199.
- Liu, M. & Yang, Y. (2003). Extensional collapse of the Tibetan Plateau: results of three-dimensional finite element modeling. *Journal of Geophysical Research* **108**, 2361.
- Liu, S., Li, W., Wang, K., Qian, T. & Jiang, C. (2015). Late Mesozoic development of the southern Qinling–Dabieshan foreland fold-thrust belt, Central China, and its role in continent–continent collision. *Tectonophysics* **644–645**, 220–234.
- Liu, S., Pan, Y., Xie, Q., Zhang, J. & Li, Q. (2004). Archean geodynamics in the Central Zone, North China Craton: constraints from geochemistry of two contrasting series of granitoids in the Fuping and Wutai complexes. *Precambrian Research* **130**, 229–249.
- Liu, S., Steel, R. & Zhang, G. (2005). Mesozoic sedimentary basin development and tectonic implication, northern Yangtze Block, eastern China: record of continent–continent collision. *Journal of Asian Earth Sciences* **25**, 9–27.
- Liu, S. W., Li, Q. G., Tian, W., Wang, Z. Q., Yang, P. T., Wang, W., Bai, X. & Guo, R. R. (2011a). Petrogenesis of Indosinian granitoids in middle-segment of South Qinling Tectonic Belt: constraints from Sr–Nd isotopic systematics. *Acta Geologica Sinica - English Edition* **85**, 610–628.
- Liu, S. W., Yang, P. T., Li, Q. G., Wang, Z. Q., Zhang, W. Y. & Wang, W. (2011b). Indosinian granitoids and orogenic processes in the middle segment of the Qinling Orogen, China. *Journal of Jilin University (Earth Science Edition)* **41**, 1928–1943. (in Chinese with English abstract).
- Liu, Y. S., Gao, S., Hu, Z. C., Gao, C. G., Zong, K. Q. & Wang, D. B. (2010). Continental and oceanic crust recycling-induced melt-peridotite interactions in the Trans-North China Orogen: U–Pb dating, Hf isotopes and trace elements in zircons from mantle xenoliths. *Journal of Petrology* **51**, 537–571.
- Lu, Y. H., Zhao, Z. F. & Zheng, Y. F. (2016). Geochemical constraints on the source nature and melting conditions of Triassic granites from South Qinling in central China. *Lithos* **264**, 141–157.
- Ludwig, K. R. (2003). *ISOPLLOT 3.0: A Geochronological Toolkit for Microsoft Excel*. Los Angeles, Berkeley: Berkeley Geochronology Center Special Publication.
- Maniar, P. D. & Piccoli, P. M. (1989). Tectonic discrimination of granitoids. *Geological Society of America Bulletin* **101**, 635–643.
- Martin, H., Smithies, R. H., Rapp, R., Moyen, J. F. & Champion, D. (2005). An overview of adakite, tonalite–trondhjemite–granodiorite (TTG), and sanukitoid: relationships and some implications for crustal evolution. *Lithos* **79**, 1–24.

- Matte, P. (2001). The Variscan collage and orogeny (480–290 Ma) and the tectonic definition of the Armorica microplate: a review. *Terra Nova* **13**, 122–128.
- Middlemost, E. A. K. (1994). Naming materials in the magma/igneous rock system. *Earth-Science Reviews* **37**, 215–224.
- Miller, C. F., Stoddard, E. F., Bradfish, L. J. & Dollase, W. A. (1981). Composition of plutonic muscovite: genetic implications. *Canadian Mineralogist* **19**, 25–34.
- Morimoto, N. (1988). Nomenclature of pyroxenes. *Mineralogy and Petrology* **39**, 55–76.
- Moyen, J.-F. (2009). High Sr/Y and La/Yb ratios: the meaning of the “adakitic signature”. *Lithos* **112**, 556–574.
- Niu, Y. (2017). Slab breakoff: a causal mechanism or pure convenience? *Science Bulletin* **62**, 456–461.
- Otamendi, J. E. & Patiño Douce, A. E. (2001). Partial melting of aluminous Metagreywackes in the Northern Sierra de Comechingones, Central Argentina. *Journal of Petrology* **42**, 1751–1772.
- Patiño Douce, A. E. (1999). What do experiments tell us about the relative contributions of crust and mantle to the origin of granitic magmas? *Geological Society, London, Special Publications* **168**, 55–75.
- Patiño Douce, A. E. (2004). Vapor-absent melting of tonalite at 15–32 kbar. *Journal of Petrology* **46**, 275–290.
- Patiño Douce, A. E. & Beard, J. S. (1995). Dehydration-melting of Biotite Gneiss and Quartz Amphibolite from 3 to 15 kbar. *Journal of Petrology* **36**, 707–738.
- Patiño Douce, A. E. & McCarthy, T. C. (1998). Melting of crustal rocks during continental collision and subduction. In: Hacker, B. R. & Liou, J. G. (eds) *When Continents Collide: Geodynamics and Geochemistry of Ultrahigh-Pressure Rocks*. Dordrecht: Springer Netherlands, pp. 27–55.
- Payne, J. L., McInerney, D. J., Barovich, K. M., Kirkland, C. L., Pearson, N. J. & Hand, M. (2016). Strengths and limitations of zircon Lu-Hf and O isotopes in modelling crustal growth. *Lithos* **248–251**, 175–192.
- Putirka, K. D., Mikaelian, H., Ryerson, F. & Shaw, H. (2003). New clinopyroxene-liquid thermobarometers for mafic, evolved, and volatile-bearing lava compositions, with applications to lavas from Tibet and the Snake River Plain, Idaho. *American Mineralogist* **88**, 1542–1554.
- Qian, Q. & Hermann, J. (2013). Partial melting of lower crust at 10–15 kbar: constraints on adakite and TTG formation. *Contributions to Mineralogy and Petrology* **165**, 1195–1224.
- Qin, J. F., Lai, S.-C. & Li, Y.-F. (2008). Slab breakoff model for the Triassic post-collisional adakitic granitoids in the Qinling Orogen, Central China: Zircon U-Pb Ages, geochemistry, and Sr-Nd-Pb isotopic constraints. *International Geology Review* **50**, 1080–1104.
- Qin, J.-F., Lai, S.-C. & Li, Y.-F. (2013). Multi-stage granitic magmatism during exhumation of subducted continental lithosphere: evidence from the Wulong pluton, South Qinling. *Gondwana Research* **24**, 1108–1126.
- Qin, J.-F., Lai, S.-C., Grapes, R., Diwu, C.-R., Ju, Y.-J. & Li, Y.-F. (2009). Geochemical evidence for origin of magma mixing for the Triassic monzonitic granite and its enclaves at Mishuling in the Qinling orogen (central China). *Lithos* **112**, 259–276.
- Qin, J.-F., Lai, S.-C., Grapes, R., Diwu, C.-R., Ju, Y.-J. & Li, Y.-F. (2010). Origin of Late Triassic high-Mg adakitic granitoid rocks from the Dongjiangkou area, Qinling orogen, central China: implications for subduction of continental crust. *Lithos* **120**, 347–367.
- Rapp, R. P. & Watson, E. B. (1995). Dehydration melting of metabasalt at 8–32 kbar: implications for continental growth and crust-mantle recycling. *Journal of Petrology* **36**, 891–931.
- Rapp, R. P., Shimizu, N., Norman, M. D. & Applegate, G. S. (1999). Reaction between slab-derived melts and peridotite in the mantle wedge: experimental constraints at 3.8 GPa. *Chemical Geology* **160**, 335–356.
- Ratschbacher, L., Hacker, B. R., Calvert, A., Webb, L. E., Grimmer, J. C., McWilliams, M. O., Ireland, T., Dong, S. & Hu, J. (2003). Tectonics of the Qinling (Central China): tectonostratigraphy, geochronology, and deformation history. *Tectonophysics* **366**, 1–53.
- Rollinson, H. (1993). *Using Geochemical Data: Evaluation, Presentation, Interpretation*. London: Longman Scientific and Technical.
- Rubatto, D. (2002). Zircon trace element geochemistry: partitioning with garnet and the link between U–Pb ages and metamorphism. *Chemical Geology* **184**, 123–138.
- Rudnick, R. L. & Gao, S. (2003). Composition of the continental crust. In: Holland, H. D. & Turekian, K. K. (eds) *Treatise on Geochemistry*, Vol. 3. Amsterdam: Elsevier Science, pp. 1–56.
- Seghedi, I. & Downes, H. (2011). Geochemistry and tectonic development of Cenozoic magmatism in the Carpathian–Pannonian region. *Gondwana Research* **20**, 655–672.
- Seghedi, I., Downes, H., Szakács, A., Mason, P. R. D., Thirlwall, M. F., Roşu, E., Pécskay, Z., Márton, E. & Panaiotu, C. (2004). Neogene–Quaternary magmatism and geodynamics in the Carpathian–Pannonian region: a synthesis. *Lithos* **72**, 117–146.
- Shi, Y., Yu, J. H. & Santosh, M. (2013). Tectonic evolution of the Qinling orogenic belt, Central China: new evidence from geochemical, zircon U–Pb geochronology and Hf isotopes. *Precambrian Research* **231**, 19–60.
- Sisson, T. W., Ratajeski, K., Hankins, W. B. & Glazner, A. F. (2005). Voluminous granitic magmas from common basaltic sources. *Contributions to Mineralogy and Petrology* **148**, 635–661.
- Sláma, J., Košler, J., Condon, D. J., Crowley, J. L., Gerdes, A., Hanchar, J. M., Horstwood, M. S. A., Morris, G. A., Nasdala, L., Norberg, N., Schaltegger, U., Schoene, B., Tubrett, M. N. & Whitehouse, M. J. (2008). Plešovice zircon—a new natural reference material for U–Pb and Hf isotopic microanalysis. *Chemical Geology* **249**, 1–35.
- Smithies, R. H. (2000). The Archaean tonalite–trondhjemite–granodiorite (TTG) series is not an analogue of Cenozoic adakite. *Earth and Planetary Science Letters* **182**, 115–125.
- Stacey, J. T. & Kramers, J. D. (1975). Approximation of terrestrial lead isotope evolution by a two-stage model. *Earth and Planetary Science Letters* **26**, 207–221.
- Stern, R. J. (2002). Subduction zones. *Reviews of Geophysics* **40**, 1012.
- Stern, C. R. & Kilian, R. (1996). Role of the subducted slab, mantle wedge and continental crust in the generation of adakites from the Andean Austral Volcanic Zone. *Contributions to Mineralogy and Petrology* **123**, 263–281.
- Sun, S.-S. & McDonough, W. F. (1989). Chemical and isotopic systematics of oceanic basalts: implications for mantle composition and processes. *Geological Society, London, Special Publications* **42**, 313–345.
- Sylvester, P. J. (1998). Post-collisional strongly peraluminous granites. *Lithos* **45**, 29–44.
- Uchida, E., Endo, S. & Makino, M. (2007). Relationship between solidification depth of granitic rocks and formation of hydrothermal ore deposits. *Resource Geology* **57**, 47–56.
- Valley, J. W., Chiarenzelli, J. R. & McLelland, J. M. (1994). Oxygen isotope geochemistry of zircon. *Earth and Planetary Science Letters* **126**, 187–206.
- Valley, J. W., Kinny, P. D., Schulze, D. J. & Spicuzza, M. J. (1998). Zircon megacrysts from kimberlite: oxygen isotope

- variability among mantle melts. *Contributions to Mineralogy and Petrology* **133**, 1–11.
- van Achterbergh, E., Ryan, C., Jackson, S. & Griffin, W. L. (2001). Appendix 3 data reduction software for LA-ICP-MS. In: Sylvester, P. (ed.) *Laser-Ablation-ICPMS in the Earth Sciences*. Québec, Canada: Mineralogical Association of Canada Short Course, pp. 239–243.
- Vielzeuf, D. & Montel, J. M. (1994). Partial melting of metagreywackes. Part I. Fluid-absent experiments and phase relationships. *Contributions to Mineralogy and Petrology* **117**, 375–393.
- Wang, F., Lu, X. X., Lo, C. H., Wu, F. Y., He, H. Y., Yang, L. K. & Zhu, R. X. (2007a). Post-collisional, potassic monzonite–minette complex (Shahewan) in the Qinling Mountains (central China): $^{40}\text{Ar}/^{39}\text{Ar}$ thermochronology, petrogenesis, and implications for the dynamic setting of the Qinling orogen. *Journal of Asian Earth Sciences* **31**, 153–166.
- Wang, F., Zhu, R. X., Hou, Q. L., Zheng, D. W., Yang, L. K., Wu, L., Shi, W. B., Feng, H. L., Sang, H. Q., Zhang, H. Y. & Liu, Q. (2014). $^{40}\text{Ar}/^{39}\text{Ar}$ thermochronology on Central China Orogen: cooling, uplift and implications for orogeny dynamics. *Geological Society, London, Special Publications* **378**, 189–206.
- Wang, L.-J., Griffin, W. L., Yu, J.-H. & O'Reilly, S. Y. (2013). U–Pb and Lu–Hf isotopes in detrital zircon from Neoproterozoic sedimentary rocks in the northern Yangtze Block: implications for Precambrian crustal evolution. *Gondwana Research* **23**, 1261–1272.
- Wang, Q., Chung, S.-L., Li, X.-H., Wyman, D., Li, Z.-X., Sun, W.-D., Qiu, H.-N., Liu, Y.-S. & Zhu, Y.-T. (2012). Crustal melting and flow beneath Northern Tibet: evidence from Mid-Miocene to Quaternary Strongly Peraluminous Rhyolites in the Southern Kunlun Range. *Journal of Petrology* **53**, 2523–2566.
- Wang, Q., Hawkesworth, C. J., Wyman, D., Chung, S.-L., Wu, F.-Y., Li, X.-H., Li, Z.-X., Gou, G.-N., Zhang, X.-Z., Tang, G.-J., Dan, W., Ma, L. & Dong, Y.-H. (2016). Pliocene–Quaternary crustal melting in central and northern Tibet and insights into crustal flow. *Nature Communications* **7**, 11888.
- Wang, X., Wang, T. & Zhang, C. (2015). Granitoid magmatism in the Qinling orogen, central China and its bearing on orogenic evolution. *Science China Earth Sciences* **58**, 1497–1512 (in Chinese with English abstract).
- Wang, X., Wang, T., Castro, A., Pedreira, R., Lu, X. & Xiao, Q. (2011). Triassic granitoids of the Qinling orogen, central China: genetic relationship of enclaves and rapakivi-textured rocks. *Lithos* **126**, 369–387.
- Wang, X., Wang, T. A. O., Jahn, B.-M., Hu, N. & Chen, W. E. N. (2007b). Tectonic significance of Late Triassic post-collisional lamprophyre dykes from the Qinling Mountains (China). *Geological Magazine* **144**, 837–848.
- Watson, E. B. & Harrison, T. M. (1983). Zircon saturation revisited: temperature and composition effects in a variety of crustal magma types. *Earth and Planetary Science Letters* **64**, 295–304.
- Weinberg, R. F. & Hasalová, P. (2015). Water-fluxed melting of the continental crust: a review. *Lithos* **212–215**, 158–188.
- Wiedenbeck, M., AlIÉ, P., Corfu, F., Griffin, W. L., Meier, M., Oberli, F., Quadri, A. V., Roddick, J. C. & Spiegel, W. (1995). Three natural zircon standards for U–Th–Pb, Lu–Hf, trace element and REE analyses. *Geostandards and Geoanalytical Research* **19**, 1–23.
- Woodhead, J. D. & Hergt, J. M. (2005). A preliminary appraisal of seven natural zircon reference materials for in situ Hf isotope determination. *Geostandards and Geoanalytical Research* **29**, 183–195.
- Wu, F. Y., Jahn, B., Wilde, S. A., Lo, C. H., Yui, T. F., Lin, Q., Ge, W. C. & Sun, D. Y. (2003). Highly fractionated I type granite in NE China (I): geochronology and petrogenesis. *Lithos* **66**, 241–273.
- Wu, Y. B. & Zheng, Y. F. (2013). Tectonic evolution of a composite collision orogen: an overview on the Qinling–Tongbai–Hong'an–Dabie–Sulu orogenic belt in central China. *Gondwana Research* **23**, 1402–1428.
- Wu, Y., Zhou, G., Gao, S., Liu, X., Qin, Z., Wang, H., Yang, J. & Yang, S. (2014). Petrogenesis of Neoproterozoic TTG rocks in the Yangtze Craton and its implication for the formation of Archean TTGs. *Precambrian Research* **254**, 73–86.
- Xu, H., Ma, C. & Ye, K. (2007). Early Cretaceous granitoids and their implications for the collapse of the Dabie orogen, eastern China: SHRIMP zircon U–Pb dating and geochemistry. *Chemical Geology* **240**, 238–259.
- Xu, H., Ma, C., Zhang, J. & Ye, K. (2013). Early Cretaceous low-Mg adakitic granites from the Dabie orogen, eastern China: petrogenesis and implications for destruction of the over-thickened lower continental crust. *Gondwana Research* **23**, 190–207.
- Yang, J.-H., Chung, S.-L., Zhai, M.-G. & Zhou, X.-H. (2004). Geochemical and Sr–Nd–Pb isotopic compositions of mafic dikes from the Jiaodong Peninsula, China: evidence for vein-plus-peridotite melting in the lithospheric mantle. *Lithos* **73**, 145–160.
- Yang, P. T., Liu, S. W., Li, Q. G., Wang, Z. Q., Wang, R. T. & Wang, W. (2012). Geochemistry and zircon U–Pb–Hf isotopic systematics of the Ningshan granitoid batholith, middle segment of the south Qinling belt, Central China: constraints on petrogenesis and geodynamic processes. *Journal of Asian Earth Sciences* **61**, 166–186.
- Yang, P. T., Liu, S. W., Li, Q. G., Wang, Z. Q., Zhang, F. & Wang, W. (2014). Chronology and petrogenesis of the Hejiazhuang granitoid pluton and its constraints on the Early Triassic tectonic evolution of the South Qinling Belt. *Science China Earth Sciences* **57**, 232–246.
- Yang, P. T., Liu, S. W., Li, Q. G., Zhang, F., Wang, Z. Q., Wang, D. S., Wang, R. T., Yan, Q. R. & Yan, Z. (2011). Ages of the Laocheng Granitoids and crustal growth in the South Qinling Tectonic Domain, Central China: zircon U–Pb and Lu–Hf isotopic constraints. *Acta Geologica Sinica - English Edition* **85**, 854–869.
- Yan, Z., Wang, Z. Q., Chen, L., Liu, S. W., Ren, T., Xu, X. Y. & Wang, R. T. (2014). Tectono-magmatism and metallogenesis of Shanyang-Zhashui ore concentration area, Qinling Orogen. *Acta Petrologica Sinica* **30**, 401–414. (in Chinese with English abstract).
- Zhang, B. T., Wu, J. Q., Ling, H. F. & Chen, P. R. (2010). Petrological discrimination between primary and secondary muscovites and its geological implications: a case study of Fucheng peraluminous granite pluton in southern Jiangxi. *Acta Petrologica et Mineralogica* **29**, 225–234. (in Chinese with English abstract).
- Zhang, F., Liu, S. W., Chen, X., Li, Q. G., Dai, J. Z., Yang, K., Wu, F. H. & Chen, Y. Z. (2012). Xiba granitic pluton in the Qinling Orogenic Belt, central China: its petrogenesis and tectonic implications. *Acta Geologica Sinica - English Edition* **86**, 1128–1142.
- Zhang, F., Liu, S. W., Li, Q. G., Sun, Y. L., Wang, Z. Q., Yan, Q. R. & Yan, Z. (2011). Re–Os and U–Pb geochronology of the Erlihe Pb–Zn deposit, Qinling orogenic belt, central China, and constraints on its deposit genesis. *Acta Geologica Sinica - English Edition* **85**, 673–682.
- Zhang, G. W., Zhang, B. R., Yuan, X. C. & Chen, J. Y. (2001). *Qinling Orogenic Belt and Continental Dynamics*. Beijing: Science Press.

- Zhang, R. Y., Liou, J. G. & Ernst, W. G. (2009). The Dabie–Sulu continental collision zone: a comprehensive review. *Gondwana Research* **16**, 1–26.
- Zhang, Z. Q., Zhang, G. W., Tang, S. H., Wang, J. H., Xu, J. F. & Yang, Y. C. (2002). Age of Anzishan granulites in the Mianxian–Lueyang suture zone of Qinling orogen: with a discussion of the timing of final assembly of Yangtze and North China Craton blocks. *Chinese Science Bulletin* **47**, 1925–1929.
- Zhao, X. X. & Coe, R. S. (1987). Palaeomagnetic constraints on the collision and rotation of North and South China. *Nature* **327**, 141–144.
- Zheng, Y. (2008). A perspective view on ultrahigh-pressure metamorphism and continental collision in the Dabie-Sulu orogenic belt. *Science Bulletin* **53**, 3081–3104.
- Zheng, Y.-F., Xia, Q.-X., Chen, R.-X. & Gao, X.-Y. (2011). Partial melting, fluid supercriticality and element mobility in ultrahigh-pressure metamorphic rocks during continental collision. *Earth-Science Reviews* **107**, 342–374.
- Zhu, D. C., Wang, Q., Cawood, P. A., Zhao, Z.-D. & Mo, X. X. (2017). Raising the Gangdese Mountains in southern Tibet. *Journal of Geophysical Research: Solid Earth* **122**, 214–223.
- Zhu, D. C., Wang, Q., Zhao, Z. D., Chung, S. L., Cawood, P. A., Niu, Y., Liu, S. A., Wu, F. Y. & Mo, X. X. (2015). Magmatic record of India-Asia collision. *Scientific Reports* **5**, 14289.
- Zhu, R. X., Yang, Z. Y., Wu, H. N., Ma, X. H., Huang, B. C., Meng, Z. F. & Fang, D. J. (1998). Paleomagnetic constraints on the tectonic history of the major blocks of China during the Phanerozoic. *Science in China Series D: Earth Sciences* **41**, 1–19.